

Application of Damage Tolerant Design in Mechanical Engineering

Doctoral Thesis

Miraj Muhammad Jan



University of Leoben, November 2008



Affidavit

I declare in lieu of oath that I wrote this thesis and performed the associated research myself, using only literature cited in this volume.

Leoben, November 2008

Miraj Muhammad Jan
M.Sc. (Engg.), B.Sc. (Engg.)



Dedication

To my hardworking father who put us on the path of education,

To my mother who gave us everything

To my caring and loving wife

And to my lovely children!



Acknowledgements

This thesis has been written at the Chair of Mechanical Engineering of the Montanuniversität Leoben. At the successful moment of presenting my work, I would like to thank all the co-workers of the institute for their wonderful cooperation during my working period at the institute with special words as following:

I would like to express my sincere gratitude to the head of the institute, Univ.-Prof. Dipl.-Ing. Dr.techn. W. Eichlseder, who provided me the opportunity to work under his kind guidance. His good leadership and nice personality provided a friendly environment for working. It is my pleasure to express that I have learnt a lot from his lectures and from his talks at the institute.

My heartfelt thanks go to Dipl.-Ing. Dr. mont. H.-P. Gänser, for supervising me with great care during my whole stay at the institute. Without his kind cooperation and friendly guidance it would have been impossible for me to complete this work. In addition to that I am thankful to him for his care and support in many social matters.

I would like to offer my special thanks to Univ.-Doz. Dipl.-Ing. Dr. techn., H. Pettermann (Vienna University of Technology) for his helpful discussion and opinions. His careful review helped me understanding many things and finalizing the thesis with a fine touch.

Many thanks are due for the careful support and friendly behaviour of Dipl.-Ing. Dr. mont. István Gódor, Dipl.-Ing. Dr. mont. H. Leitner, Dipl.-Ing. Dr. mont. M. Stoschka, Dipl.-Ing. Dr. mont. J. Fröschl, and Dipl.-Ing. Dr. mont. F. Grün. Their fruitful advices and discussions provided a basis for the experimental work and for resolving many related problems.

I want to use this opportunity to say words of thanks to Dipl.-Ing. Dr. mont. M. Riedler, Dipl.-Ing. Dr. mont. A. Javidi, Dipl.-Ing. Dr. mont. A. Lamik, Dipl.-Ing. C. Guster, Dipl.-Ing. H. Köberl, Dipl.-Ing. C. Haberer, Dipl.-Ing. T. Fössl, Dipl.-Ing. W. Tan and Miss M. Höfler for their support and encouragement.

I deeply acknowledge the priceless help and support provided by Dipl.-Ing. G. Winter and Dipl.-Ing. A. Leitgeb for their help and guidance in the lab work as well as at the desk.

Grateful acknowledgements are expressed to the “good souls” of the institute, Mrs. C. Lohner and Mrs. E. Wolfgruber, for their kind help and support.

Moreover, I want to express my gratitude to the workshop team of the institute, Mr. F. Grabner, Mr. M. Bichler and their co-workers, for their support and help with the test specimens.

A lot of thanks are due to the project partner, Dipl.-Ing K. Irnberger (Magna Steyr Weltraumtechnik) for discussions and providing material and literature.

I would like to acknowledge the financial support and administrative work from the Higher Education Commission of Pakistan. Due to their great effort it was possible to join such a wonderful institute and use the latest research facilities. Many thanks are due to the management and colleagues of HMC-3 Pakistan for their encouragement and moral support.

Moreover, I am thankful to the Austrian Exchange Service (ÖAD) with a special word of thanks to Mag. K. Bauman (Vienna), Mrs. D. Holzapfel (Leoben) and Mrs. N. Juritsch (Leoben) for their thorough support and help in solving many social problems.

At the end, I would like to offer special thanks to my parents for their guidance, prayers and well wishes, to my wife *Aisha* for her lovely care, understating and wholehearted support, and to our children *Musa* and *Saliha* for their patience and love.

Miraj Muhammad Jan
Leoben, Nov. 2008



Abstract

The traditional design methodology for dimensioning against cyclic loading is the stress-based approach. In the simplest case, nominal stresses are corrected by stress concentration factors and (semi-)empirical factors accounting for type of loading and operation, size and surface finish effects. The corrected stresses are then compared to admissible values from Smith or Haigh diagrams, or to stress-life (S/N) curves, obtained from specimens of standardized size and surface quality. The advantage of this approach is that it is well established and is practically most widely used by design engineers.

Most engineering components and structures are designed such that the stresses are below the yield point. If, however, an overload occurs, the material response may not be in the elastic range in some regions. This is particularly true for critical locations such as notches. In that case a strain-life approach is used, in which the material behaviour is examined under deformation controlled tests and given in the form of ϵ/N curves.

In practice, the material contains certain natural defects, inclusions or inhomogeneities which originate from the production processes such as casting and welding or from foreign object damage (FOD). The effect of these small flaws is often accounted for, in a purely empirical manner, by S/N curves from damaged components. On the other hand, such flaws yield often the same high stress gradients as cracks, and are therefore sometimes approximated as cracks. The design methodology which takes these into account is the damage tolerant design approach (DTD). In case of cyclic loading, the DTD approach ensures that the inherent cracks will not propagate to failure either within the design life or between inspection periods.

In this thesis, these three primary approaches – stress-life, strain-life, and DTD – are used to analyse fatigue damage with special focus on investigating flaws typically encountered in structural parts. The fatigue limit of undamaged and damaged specimens is assessed experimentally as well as theoretically. An effort is made to combine the existing concepts and to re-interpret the results obtained by the DTD and strain-life approaches in the framework of the conventional stress-life method. For a material containing defects, the idea of net section yielding is exploited to transform the S/N curve of an undamaged material to a damaged one. Finally, a method is proposed for obtaining an estimate of the fatigue lifetime of a component with and without defects using the static tensile properties in combination with the fatigue crack growth properties of the material. A guideline for obtaining a first estimate of fatigue data useful for purposes of preliminary design is developed and verified experimentally for a wrought aluminium alloy typically used for cryogenic applications.

As a practical design application, the fatigue response of thin-walled tubular specimens is considered. A special rig having the capability to test various materials such as aluminium and steel alloys under arbitrary combinations of static and/or periodic internal pressure and axial loading has been designed. First promising results for aluminium tubes under static internal pressure and axial fatigue loading are presented.



Table of Contents

Introduction	1
1. General Background.....	4
1.1. Basic design philosophies	4
1.1.1. Safe-life approach.....	4
1.1.2. Fail-safe approach	4
1.1.3. Damage tolerant design (DTD)	5
1.2. Life prediction models.....	5
1.2.1. Fatigue damage mechanisms – crack nucleation and growth.....	5
1.2.2. Stress-life approach	6
1.2.3. Strain-life approach	8
1.2.4. Stress-strain hysteresis loop – strain energy density approach.....	10
1.2.5. Crack growth lifetime estimation approaches	10
2. Codes and Standards for Damage Tolerant Design.....	16
2.1. General description.....	16
2.1.1. Philosophy of assessment methodologies	17
2.1.2. Flaw selection and re-characterization	17
2.2. Static failure assessment.....	18
2.2.1. Basic methods.....	18
2.2.2. BS 7910.....	19
2.2.3. ASME BPV Section XI.....	20
2.2.4. SINTAP	21
2.2.5. FITNET	21
2.3. Fatigue failure assessment.....	21
2.3.1. BS 7910.....	22
2.3.2. ASME BPV Section XI.....	22
2.3.3. FKM fracture mechanics guideline	23
2.3.4. FITNET	24
2.4. Residual stresses.....	24
3. Development of Consistent Engineering Estimates for DTD in Fatigue	26
3.1. Short and long cracks	26
3.2. Different DTD methodologies for fatigue.....	27
3.3. Fatigue life curve for a material containing defects	31
3.4. Prediction of the HCF and endurance regimes.....	33
3.5. Prediction of the LCF regime	35
4. Experimental Investigation.....	40
4.1. Material	40
4.1.1. Tensile tests	40
4.1.2. Hardness measurements	41
4.2. Fatigue tests (defect free material)	42
4.2.1. HCF tests	42
4.2.2. LCF tests.....	44
4.3. Fatigue tests (with defect)	46
4.3.1. HCF tests	46
4.3.2. LCF tests.....	48
4.4. Standard fatigue crack growth tests.....	49
4.5. Residual stress measurements	53
5. Model Calibration	55
5.1. Material without defects	55
5.1.1. Fatigue crack growth and HCF.....	55
5.1.2. Mean stress effect in the HCF region.....	58
5.1.3. Estimation of the S-N curve in the LCF regime.....	59
5.1.4. Mean stress effects in the LCF region.....	63



5.2.	Material with defects	65
5.2.1.	Estimation of the HCF-endurance regime	65
5.2.2.	Estimation of the LCF regime	67
5.2.3.	Estimation of HCF-LCF based on net section stresses.....	69
5.3.	Residual stress effects	71
6.	Guidelines for Engineering Estimates	74
6.1.	Material without defects.....	74
6.2.	Material with defects	76
7.	Fatigue Testing on Thin Tubes.....	78
7.1.	Introduction	78
7.2.	Background	78
7.3.	Design approximations.....	79
7.4.	Design for cyclic loading	80
7.5.	Experimental details	80
7.5.1.	Design of experimental rig	80
7.5.2.	Material and specimen.....	82
7.5.3.	Fatigue tests	84
7.6.	Results and discussion.....	84
7.6.1.	Application of the DTD engineering estimates to thin tubes	87
8.	Comparison and Validation.....	90
8.1.	Comparison with crack growth data.....	90
8.2.	Comparison with quality S-N curves	91
8.3.	Application to cryogenic conditions.....	92
8.4.	Comparison with FKM Guideline	95
9.	Summary and Conclusion	96
9.1.	Summary	96
9.2.	Conclusion and outlook.....	98
10.	References	99



Introduction

Dimensioning of components against cyclic loading is of major importance in the design of structural components. Fatigue life can be divided into two different phases – crack initiation and crack propagation. The initiation life comprises the development and early growth of a small crack and the propagation life is the part of the total life spent until complete failure of the component. The question which stage should be considered for design purposes depends on various factors.

The traditional approach relies on a stress-based methodology using S-N curves obtained from experiments on specimens of standardized size and surface finish. Despite the fact that the stress-life approach is of a largely empirical nature, it is commonly used by design engineers for fatigue life prediction, especially in the high cycle fatigue region where the material behaviour is predominantly elastic.

For components under high loading, where the material yields, the strain-life methodology considering the cyclic stress-strain behaviour of the material is adopted.

The S-N curve obtained from the stress based approach is helpful in providing a fatigue life prediction in the HCF regime. Similarly, the strain life approach results in ϵ -N curve for the LCF regime. Both life prediction models require detailed experimental investigations. For design engineers accustomed to dimensioning against fatigue loading using the stress-based approach, it might be helpful to interpret strain-life results in the framework of the stress-based concept.

On the other hand, with the introduction of fracture mechanics, the modelling of crack growth has become possible. Paris and co-workers were the first to propose a simple fatigue crack growth law. Within this framework, a fatigue lifetime prediction can be obtained using the crack geometry, material properties and applied loading. However, for an engineering assessment of materials containing multiple defects such as casting, forging or welding flaws – which in the worst case may be regarded as cracks – this method becomes computationally too expensive.

There exist a lot of codes (see e.g., [50][92][94][95]) for the structural integrity of components providing guidelines for the design of components containing flaws. The range of these codes varies from general to specific applications such as nuclear industry. Many of these rules have been developed for a specific manufacturing technology, a single industrial sector or as a national document. Codes¹ such as the British R6 and the GKSS Engineering Treatment Model (ETM) are for general use as well as for power generation applications. The British Standard BS 7910 is primarily focused on the assessment of welded components. On the other hand, the US API 579 and ASME codes provide guidelines for the offshore and pressure vessel industries. Regarding the failure modes, many of these guidelines are also taking into account cyclic loading in addition to static failure.

In the majority of codes, two types of fatigue assessment are provided. For the defect-free case, a conventional stress-based methodology is adopted. In this case the following cases are considered [105]

- S-N curves with a nominal stress criterion
- S-N curves with hot spot stresses
- S-N curves with a local approach

For a material containing defects, a fracture mechanics based methodology is normally provided by all of the aforementioned codes.

Procedures like ETM, R6 and SINTAP (structural integrity assessment procedure) mainly consider static fracture as a failure mode. However, the British R5 – assessment procedure for high-temperature response of structures – considers the initiation of cracks by creep and fatigue damage [97].

In the ASME Boiler and Pressure Vessel (BPV) Code Section VIII, the fatigue design curves are derived from low cycle fatigue tests of smooth specimens, which are then corrected by means of stress

¹ A more detailed description of these codes follows below.



concentration and strength reduction factors. Similarly, ASME BPV Code Section XI provides guidelines for an assessment of fatigue crack growth. However, owing to the specific application of the code, the fatigue design curve and reference fatigue crack growth curves are mostly related to US steel grades [93] [53].

In BS 7910, guidelines for assessing the acceptability of flaws in metallic structures are given. Assessment routes are provided for unwelded as well as for welded parts. For planar flaws, a fracture mechanics procedure is recommended; however, a simplified procedure based on quality S-N curves can also be adopted [50].

The most recent addition to the structural integrity assessment procedures is the FITNET fitness-for-service (FFS) procedure [100]. The method provides guidelines for fracture, fatigue, creep and corrosion damage. The fatigue module of the procedure draws heavily from existing design rules and recommendations (e.g. IIW, Eurocode 3) and flaw assessment procedures (e.g. BS 7910, API 579, R6). The method provides the following five assessment routes for fatigue:

- Nominal stress analysis
- Structural stress or notch stress
- Non-linear local stress-strain analysis
- Fatigue crack growth analysis
- Assessment of non-planar flaws

The first three routes are valid for cases where no flaw is present. In the presence of flaws, the last two steps are followed, which are similar to BS 7910. For a conservative assessment, non-planar flaws are taken as planar; however, another possibility is to treat them according to route 1 (nominal stress analysis) using S-N curves for welded joints, for which cases the equivalent fatigue strength is established; this corresponds to the quality S-N curve approach as provided by BS 7910. For planar, crack-like flaws, a fatigue crack growth analysis has to be carried out. In this case, the assessment is further subdivided into unwelded and welded cases. For the former, the NASGRO crack growth equation is used; for the latter, the Paris crack growth equation is applied.

All of the aforementioned procedures are well established. Nevertheless, the more advanced assessment routes therein are characterized by high demands on experimental and numerical analyses, whereas many of the more basic approaches are based on estimates of doubtful accuracy [56] (see also [111],[112]) and must therefore rely heavily on empirical safety factors.

Therefore, despite the multitude of FFS codes available, a need for a *simple, versatile* and *reliable* criterion for a preliminary design against fatigue still persists in the context of damage tolerant design. The key issues simplicity, versatility and reliability are motivated as follows:

- *Simplicity*: Keeping in view the cost of experimental work needed for obtaining S-N or ϵ -N curves, it is desirable to develop an inexpensive and easy-to-use approximate methodology for obtaining estimates for S-N and ϵ -N curves from a minimum of experimental tests.
- *Versatility*: The method developed should be likewise applicable to the LCF, HCF, and endurance regimes. Also, the treatment of components with and without flaws should follow the same logic, thereby eliminating the complication of having to choose between different assessment routes.
- *Reliability*: It lies in the nature of an approximate approach that it is of moderate accuracy. However, the estimates obtained should lie on the conservative side throughout. Furthermore, ideally a method should be available for estimating the degree of conservatism of the approach chosen, so that the corresponding safety factors – if necessary at all – may be determined accordingly.

The above goals can be met by combining and comparing the various existing fatigue life prediction approaches. More specifically, crack growth models can be adopted for estimating the HCF and endurance regimes of the stress-life curve. This is due to the fact that fatigue failure is a result of various stages:



- Crack initiation phase and short crack propagation phase
- Long crack propagation phase (the region where the Paris law is valid)
- Unstable crack growth (final rupture)

With the exception of crack initiation, fatigue life is therefore related to the different stages of fatigue crack growth. On the other hand, the endurance regime (i.e., infinite fatigue life) corresponds to the threshold for fatigue crack growth; this relation is visualized in the Kitagawa diagram – a bi-logarithmic plot of defect size vs. allowable stress range.

In the LCF regime, the use of linear-elastic fracture mechanics (LEFM) does not provide reliable results because of large-scale plasticity. A possible link between the strain-life and the stress-life curves is provided by the cyclic stress-strain curve. Alternatively, an estimate for the LCF behaviour may be constructed by interpolating between the static and the HCF behaviour.

In the present study, the aforementioned concepts are applied to the characterization of the fatigue behaviour of a thin aluminium sheet. A method is developed for estimating an approximate combined S-N curve valid for the LCF, HCF and endurance regimes. The estimate is based on experimental results from fatigue crack growth and static tensile tests. The HCF part of the stress-life curve is obtained from an integration of fatigue crack growth curves and from the Kitagawa diagram. A simple interpolation between the static behaviour (as assessed by means of tensile tests) and the HCF behaviour is provided for the LCF regime. A net section yielding criterion is used for accounting for the presence of flaws. The estimated stress-life curve is verified by comparison with experimental results from Woehler tests (HCF) and strain-controlled tests (LCF). Finally, the influence of residual stresses for welded sheet (including welding flaws) is also taken into account.



1. General Background

1.1. Basic design philosophies

Engineering components are loaded under different types of loading. These include monotonic, variable amplitude, uni- or multi-axial conditions. Among other factors, the failure of a component is dependent on load, time, material and environment. From a temporal classification of load types, one may distinguish two basic failure modes, i.e., static and fatigue failure.

In the case of static loading, the damage mode is either brittle fracture or ductile tearing. If the loading is cyclic, the failure phenomenon is termed as fatigue. In this case, material degradation may take place well below the yield or ultimate strength. Generally, fatigue failures can be classified

- Based on the failure phenomenon
 - o Fatigue crack nucleation
 - o Fatigue crack propagation
- Based on the type of fatigue loading
 - o Constant or variable amplitude loading
 - o Proportional or multiaxial loading
- Based on the environment
 - o Corrosion fatigue
 - o Fretting fatigue
 - o Creep fatigue

The design of an engineering component may be based on different approaches, depending on the intended application of the component. For example, the component or structure may be safety critical or not. Similarly, there may be certain parts which can be replaced during operation; however, many applications may have a single part which cannot afford in-service substitution. Such considerations lead to different design principles. In the traditional method, strength is the major concern. Modern methods involve additionally the consideration of inherent flaws and mechanical defects. Depending on the required objectives, various approaches are applied for dimensioning. Irrespective of the type of loading, there exist three basic design approaches – safe-life, fail-safe and damage tolerant design.

1.1.1. Safe-life approach

In this case, a component is designed for a particular lifetime. This is one of the simplest design approaches [1], where the structure is assumed to be free of defects. The design of a component is carried out on the strength of the material and is mainly applied to critical components where the maintenance of the part is complex. Design is based on either calculation or some tests and the part is removed from service when its useful life is consumed. Various empirical safety factors are used to obtain a reliable lifetime, and the design life is some fraction of estimated life (typically of the order of one fifth [2]). However, with this type of approach the part may be substantially over-dimensioned.

1.1.2. Fail-safe approach

In this case the system is made redundant such that a multiple load path is provided. A typical example of such an approach is the leak-before-break approach in pressurized vessels where the part is designed such as to leak instead of having a guillotine fracture. The multiple load path philosophy means here that other, less intensely loaded areas of the vessel cross-section take over some load, thereby reducing the load on the leak. This gives the possibility of detecting local damage or partial fracture either by online monitoring or in the course of regular inspections [3].

1.1.3. Damage tolerant design (DTD)

The more recently developed total life – crack initiation and crack propagation – based DTD approach allows the operation of a component even in the presence of a crack. However, crack growth is restricted to be below the critical length during the entire or remaining life of the component, to avoid fracture. The methodology uses fracture mechanics techniques, which take the resistance of the material and the geometry of the crack as well as the applied loading² into consideration. It is widely used in the aerospace, transport, offshore and nuclear industries. If applied in the design stage, an inspectable flaw size based on the non-destructive testing (NDT) resolution is assumed for calculating the lifetime of a component. Similarly, if a crack is found in service, then it is possible – depending on the loading and the crack size – to predict the remaining lifetime until the crack becomes critical, and prescribe either a replacement of the component or shorter inspection intervals.

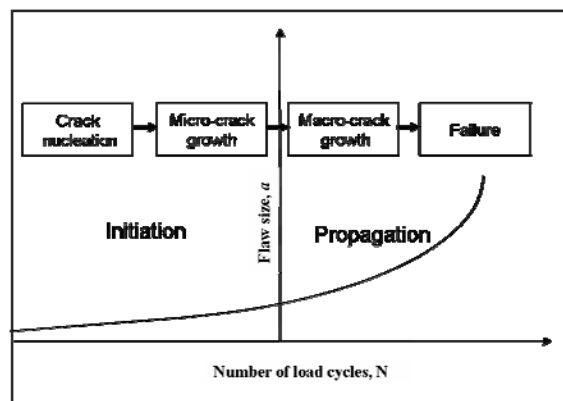


Fig. 1.1: Schematic distinction between fatigue crack initiation and propagation life

1.2. Life prediction models

1.2.1. Fatigue damage mechanisms – crack nucleation and growth

The selection of a design strategy depends on the assumed prospective lifetime. The choice between different design approaches is based on the various stages of the total life. In the case of cyclic loading, total life can be subdivided into several phases such as crack nucleation, microcrack growth, macrocrack growth and failure (unstable crack growth) [5] (see Fig. 1.1). Crack nucleation and growth are due to cyclic slip in slip bands, which occurs due to plastic deformation as a result of moving dislocations [5]. The lower constraints for the plastic deformation at the surface grains will lead to the initiation of a crack at the surface, which then grows into the subsurface grains. Furthermore, defects from manufacturing and maintenance will also promote the initiation stage. Similarly, the presence of voids or inclusions can also lead to the generation of microcracks. Cracks at such a level are termed as *small cracks* or *microstructurally short cracks* (see Chapter 3). In the early stage of propagation, these microcracks are of the order of the material's grain size. According to Schijve [7], for pure metals and commercial alloys, the formation of a small crack of about 100 μm in size can consume 60-80 % of total life [66]. As the cracks grow up to several grains, the microstructural effects vanish and the cracks are termed as *physically short cracks*, which are of the order of 0.1 ... 1 mm. Further crack growth happens in a continuous manner depending on the material resistance – a lack of crack closure plays a significant role for short cracks – until they become macrocracks, or long cracks. Finally, as the crack length reaches the size where the remaining ligament cannot bear the applied loading any further, the final forced rupture of the component takes place.

Depending on the desired lifetime, different fatigue design concepts focus either on the prediction of crack initiation, crack propagation, or crack arrest, with design criteria varying from safe-life to

² In the case of fatigue loading, special care is required when assessing multiaxial and load sequence effects (cf., e.g., [4]).

damage tolerance. For dimensioning against fatigue loading, the following basic life prediction models are in common use

- Stress-life approach
- Strain-life approach
- Strain energy density concept
- Fatigue crack growth concept

1.2.2. Stress-life approach

The basis of the stress-based method is the Woehler curve, also known as the S-N diagram. Fig. 1.2 shows a typical S-N curve. The S-N diagram is a plot of stress amplitude σ_a versus number of cycles to failure, N . There are numerous testing procedures to generate the required data for a proper S-N diagram under constant amplitude loading. The test data are usually displayed on a log-log plot with the actual S-N curve representing the statistical mean of the data from several tests, or the curve for a survival probability of 50%. For a complete assessment including statistical scatter, it proves useful to display also the corresponding lines for 90% and 10% survival probability.

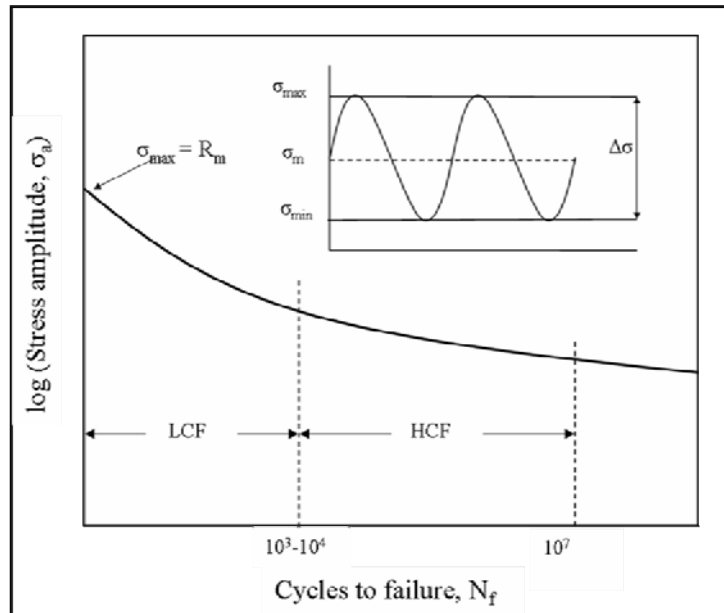


Fig. 1.2: A typical S-N curve describing different regimes (LCF low cycle fatigue, HCF high cycle fatigue) [11]

The cyclic stress amplitude σ_a is defined as one half of the difference between the peak σ_{max} and the trough σ_{min} of the stress cycle and is given by

$$\sigma_a = \frac{\sigma_{max} - \sigma_{min}}{2} \quad \text{Equ. (1.1)}$$

Similarly, the mean stress σ_m and the stress ratio R can be written as:

$$\sigma_m = \frac{\sigma_{max} + \sigma_{min}}{2} \quad \text{Equ. (1.2)}$$

$$\sigma_m = \frac{1 + R}{1 - R} \sigma_a \quad \text{Equ. (1.3)}$$

$$R = \frac{\sigma_{min}}{\sigma_{max}} \quad \text{Equ. (1.4)}$$

The load ratio R – the ratio of minimum to maximum stress – is commonly used as a measure of the mean stress influence. Generally, the S-N diagram is divided into three main areas – the LCF (low cycle fatigue) regime with $N < 10^3 \dots 10^4$, HCF (high cycle fatigue) regime with $10^3 \dots 10^4 < N < 2 \cdot 10^6 \dots 10^7$ and the endurance limit with $N > 10^7$ cycles. The endurance, or fatigue, limit is the stress amplitude at which a smooth, unnotched specimen will not fail for any number of cycles. Certain nonferrous materials and alloys such as aluminium do not have a well-defined endurance limit [8], nevertheless, for many practical purposes 10^7 cycles are taken to be ‘infinite’ life [11]. The S-N curve can be approximated by an empirical relation (Basquin law) [12]:

$$\sigma_a^k N = C \quad \text{Equ. (1.5)}$$

where $-1/k$ corresponds to the slope of the linear portion (log-scale), and k and C are material constants. Generally, a classical S-N curve can be defined using three equations:

$$N_1 \sigma_1^{k_1} = C_1; \quad N_2 \sigma_2^{k_2} = C_2 \quad \text{Equ. (1.6)}$$

$$k_i = - \left(\frac{d(\log \sigma)}{d(\log N)} \right)^{-1}, \text{ where } i = 1, 2 \quad \text{Equ. (1.7)}$$

$$k_2 = p k_1 \quad \text{Equ. (1.8)}$$

where k_1 and k_2 are the slopes in the HCF-LCF and endurance-HCF regimes, respectively. For certain aluminium alloys, $p \approx 5$ may be assumed [13].

The influence of the mean stress on the S-N curve is mostly described by the constant life diagrams, also known as Haigh or Smith diagrams. In the former diagram, the results of fatigue tests at various stress ratios are plotted as alternating stress versus mean stress for a constant life, usually 10^7 or higher (i.e., for the endurance limit). However, in the absence of data at different mean stress values the Haigh diagram may be estimated from an approximate construction using the yield strength, ultimate tensile strength, and fatigue limit at alternating loading ($R = -1$) [6].

In practice, various structures are subjected to variable amplitude loading, which is more complex than the constant amplitude S-N curve. For the simplest case, a linear damage accumulation model after Palmgren-Miner is often hypothesized. According to this the total damage D is estimated by

$$D = \sum \frac{n_i}{N_i} \quad \text{Equ. (1.9)}$$

where n_i is the number of cycles applied at a stress level corresponding to a lifetime of N_i . However, the drawback of this model is that it does not include the influence of the load sequence. A conservative approach could be to follow the same slope k as is in the finite life region (Miner-elementary model), meaning that the Basquin relation, Equ. (1.5), is assumed to be applicable for stress amplitudes below the fatigue limit. Based on the work by Haibach [15], who assumes that cycles with amplitudes above the fatigue limit will reduce the fatigue limit of the undamaged material, a reasonable result can be obtained by taking the slope of the curve to be $2k-1$ in the infinite lifetime region.

There are certain other factors which also influence the fatigue resistance. These influences are taken into account by various empirical reduction factors.

Among others, these include

- Size
- Type of loading
- Surface finish
- Temperature
- Environment

These effects have been quantified using different parameters to get a conservative estimate of the S-N curve, cf. [14].

S-N curves are mostly used in the context of macroscopic linear elastic behaviour. At such loads, the observed lifetimes are relatively long, so that this regime is called *high cycle fatigue (HCF)*.

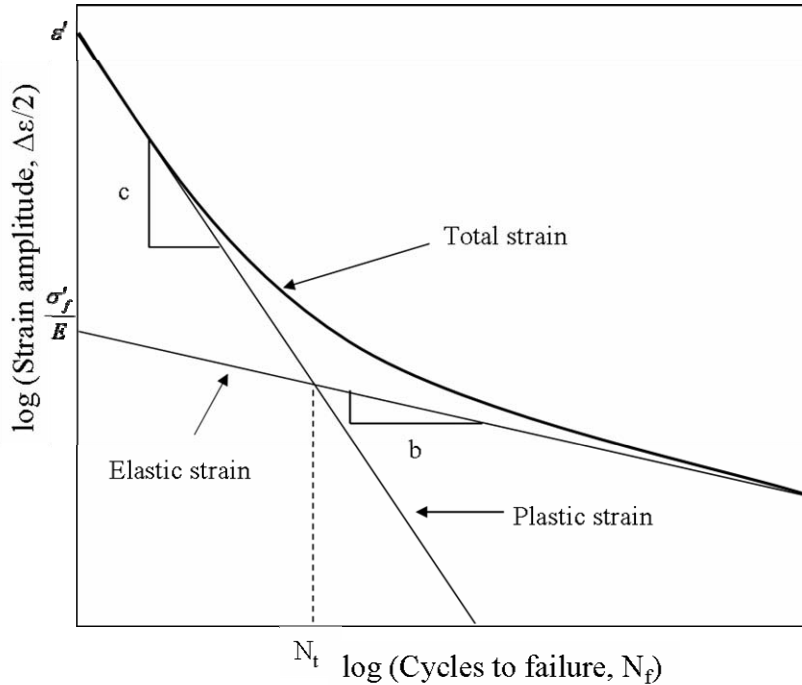


Fig. 1.3: Schematic strain-life curve with elastic-plastic strain decomposition

1.2.3. Strain-life approach

Despite the fact that many engineering components are designed such that the stresses remain within the elastic range, in many components the response of the material in critical sections such as notches is plastic. There, the local strain at the ‘hot spot’ is controlled by the elastic deformation of the surrounding material, which is under lower stress. The strain-life method is based on the assessment of such plastic strains. Fig. 1.3 shows an example of a strain-life curve. As in the stress-life approach, crack growth is not considered explicitly, and therefore this method is often considered to give an estimate of crack initiation lifetime (or, at least, an estimate of the time taken for a crack to grow from an undetectable size to a size which can be easily identified by non-destructive inspection techniques).

The total strain is obtained by the algebraic sum of the elastic and plastic strains. Thus a stress-strain curve can be modelled as

$$\varepsilon_t = \varepsilon_e + \varepsilon_p = \frac{\sigma}{E} + \left(\frac{\sigma}{K'} \right)^{\frac{1}{n'}}, \quad \text{Equ. (1.10)}$$

where K' is the strength coefficient and n' is the hardening exponent. The plastic strain relation is assumed to follow the power law

$$\sigma = K'(\varepsilon_p)^{n'}, \quad \text{Equ. (1.11)}$$

the elastic stress-strain relation follows Hooke’s law

$$\sigma = E\varepsilon. \quad \text{Equ. (1.12)}$$

The approximation for strain life is normally obtained using the Manson-Coffin [16] [17] and Basquin [12] relations. The total strain amplitude is the sum of elastic and plastic part which gives:

$$\varepsilon_{a,t} = \varepsilon_{a,e} + \varepsilon_{a,p} = \frac{\sigma_f'}{E} (2N_f)^b + \varepsilon_f' (2N_f)^c, \quad \text{Equ. (1.13)}$$

where $\varepsilon_{a,e}$, $\varepsilon_{a,p}$ and $\varepsilon_{a,t}$ are the elastic, plastic and total strain amplitudes, and b , c are the slopes of the elastic and plastic portions of the curve, respectively (b has a value near 0.1 for most materials and c varies between 0.5 and 0.7 [11],[14]). The parameters σ_f' is the fatigue strength coefficient (roughly equal to fracture strength in tension [11]) and ε_f' is the fatigue ductility coefficient (approximately equal to the fracture ductility [14]) and $2N_f$ is number of cycles to failure ($2N_f$ reversal = N_f cycle).

1.2.3.1. Influence of mean stress

The effect of mean stress on low cycle fatigue can also be obtained by different models. In most cases the Manson-Coffin-Basquin relation, Equ. (1.13), is modified. Morrow's equation [20] modifies only the elastic term and is given by

$$\varepsilon_{a,t} = \frac{\sigma_f' - \sigma_m}{E} (2N_f)^b + \varepsilon_f' (2N_f)^c. \quad \text{Equ. (1.14)}$$

Another modification of the strain-life equation accounting for the mean stress influence, including both the elastic and plastic terms, is given by Manson and Halford [23]:

$$\frac{\Delta\varepsilon}{2} = \frac{\sigma_f' - \sigma_m}{E} (2N_f)^b + \varepsilon_f' \left(\frac{\sigma_f' - \sigma_m}{\sigma_f'} \right)^{c/b} (2N_f)^c \quad \text{Equ. (1.15)}$$

Smith, Watson and Topper [21] use a different approach. It is based on the assumption that $\sigma_a \Delta\varepsilon_t/2$ for a fully reversed test ($R = -1$) is equal to $\sigma_a^{\max} \Delta\varepsilon_t/2$ for a test with a mean stress, where $\sigma_a^{\max} = \sigma_a + \sigma_m$. The SWT equation modifies both the elastic and plastic parts of the total strain as follows:

$$\sigma_{\max} \varepsilon_{a,t} = \frac{(\sigma_f')^2}{E} (2N_f)^{2b} + \sigma_f' \varepsilon_f' (2N_f)^{b+c} \quad \text{Equ. (1.16)}$$

The correlation fits reasonably well for $R = -1$ and $R = 0$ [22]; however, it becomes undefined if σ_{\max} is negative, which can be physically interpreted that no damage occurs for $\sigma_{\max} < 0$.

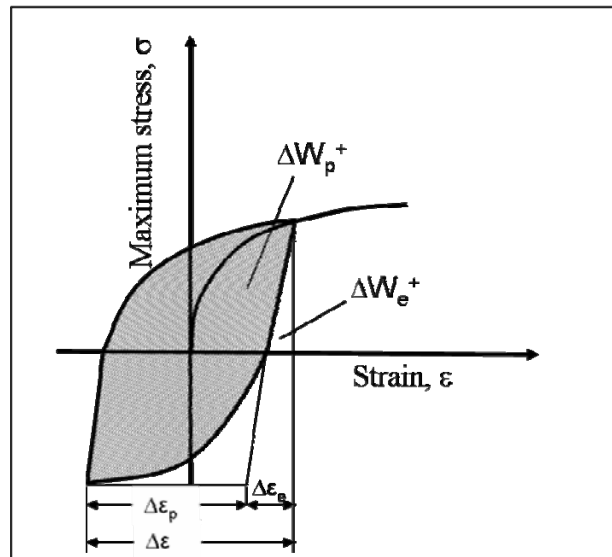


Fig. 1.4: Schematic representation of total strain energy density consisting of plastic strain energy density and tensile elastic strain energy density [19]

1.2.4. Stress-strain hysteresis loop – strain energy density approach

The response of the material under cyclic plastic loading is observed to be in the form of a hysteresis loop. The low cycle fatigue life can be modelled using the energy-based model after Morrow [18]. Here, the inelastic strain energy density is determined from the area within the stabilized cyclic stress-strain hysteresis loop. Accordingly,

$$N_f^n W_p = A. \quad \text{Equ. (1.17)}$$

A total strain energy model [19] assumes that the damage due to cyclic loading is a function of the absorbed plastic strain energy density ΔW_p and that part of the elastic strain energy which facilitates the crack growth ΔW_e^+ . In this case, ΔW_p is equivalent to the area of the hysteresis loop for a single stabilized cycle, and ΔW_e^+ is the area under the positive unloading part of the loop (Fig. 1.4). Accordingly, for fully reversed loading, the following relation was proposed

$$\Delta W_t = \Delta W_p + \Delta W_e^+. \quad \text{Equ. (1.18)}$$

Thus, the fatigue limit is postulated to be a function of the energy input. In particular, a power law relationship of the following form was suggested [19]:

$$\Delta W_t = \kappa N_f^\alpha + C, \quad \text{Equ. (1.19)}$$

where the constant C is the elastic energy input which causes no perceivable damage, its value being equivalent to the strain energy density at the material fatigue limit and N_f is number of cycles to failure. The values of k and α can be determined from the log-log plot of W_t versus N_f (Fig. 1.5).

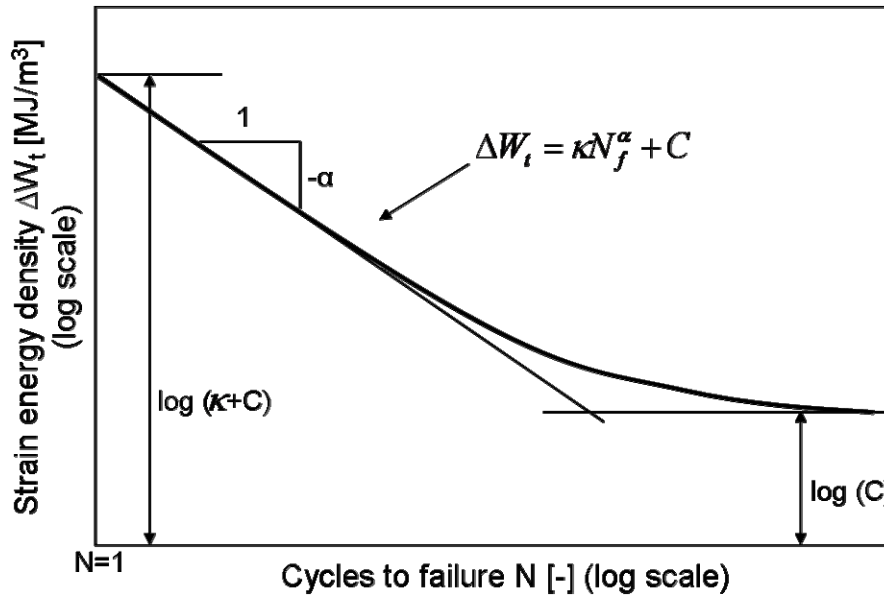


Fig. 1.5: A typical plot of total strain energy density per cycle versus number of cycles to failure; for ASTM A 516 GR 70, $\kappa = 880 \text{ MJ/m}^3$, $\alpha = -0.67$, $C = 0.1 \text{ MJ/m}^3$ [71]

1.2.5. Crack growth lifetime estimation approaches

Crack growth life prediction models mainly consider the growth of particular, well-defined cracks and estimate the allowable crack length for safe operation. Usually, linear elastic fracture mechanics (LEFM) is used to obtain the strength of a component in the presence of cracks. Griffith [24] was among the first to give the idea for brittle materials that a crack in a component will propagate if the total energy of the system is decreased with the propagation of crack. Thus, if U is the total energy of a cracked body with crack length a , the instability criterion reads [9]

$$\frac{dU}{da} \leq 0. \quad \text{Equ. (1.20)}$$

This relation was modified by Irwin for ductile materials. Later on, it was shown that the local stresses near the crack tip are of the general form [25] [26][14]

$$\sigma_{ij} = \frac{K}{\sqrt{2\pi r}} f_{ij}(\theta) + \text{Higher Order Terms}, \quad \text{Equ. (1.21)}$$

where r and θ are the cylindrical coordinates of a point with respect to the crack tip and K is the stress intensity factor (SIF) and $f_{ij}(\theta)$ is the generalised term for the geometry. Thus, crack propagation will occur if the crack driving force exceeds the critical SIF of the material. Generally, there are three different modes of loading corresponding to different crack surface displacements. These are: mode-I, opening or tensile mode; mode-II, sliding or in-plane shear; and mode-III, tearing or out-of-plane shear. For many engineering applications, mode-I is dominant. From Equ. (1.21), it can be seen that a singularity exist as $r \rightarrow 0$ for each value of θ i.e., the stresses go to infinity. However as the material yields, a plastic zone will form near the crack tip – the so called small scale yielding and the LEFM is assumed to be valid as long as this zone is smaller compare to the overall dimension of the crack and cracked body [14]. The magnitude of the local stress around the crack tip is defined by the stress intensity factor K , and it depends on loading, crack size and shape [14]. In general form it can be written as

$$K = Y\sigma\sqrt{\pi a}, \quad \text{Equ. (1.22)}$$

where σ is the remotely applied stress, a is the crack length and Y is a correction factor that depends on the specimen and crack geometry. For a wide variety of cases, different stress intensity factor solutions can be found in the literature and handbooks, e.g. [27].

One of the assumptions of LEFM is that material conditions are predominantly elastic. For fracture mechanics, the crack tip conditions are of primary relevance. According to Paris [108], the state of the crack tip zone may be classified as follows (Fig. 1.6):

- *Elastic (small scale yielding)*: In this case, the size of the plastic zone is at least an order of magnitude smaller than the smallest geometric dimension of the specimen or component
- *Elastic-plastic*: This refers to a significant plastic zone at the crack tip and may be described as intermediate scale of plastic yielding
- *Fully plastic*: In this case, the region ahead of the crack tip is fully plastified; this is referred to as large scale yielding.

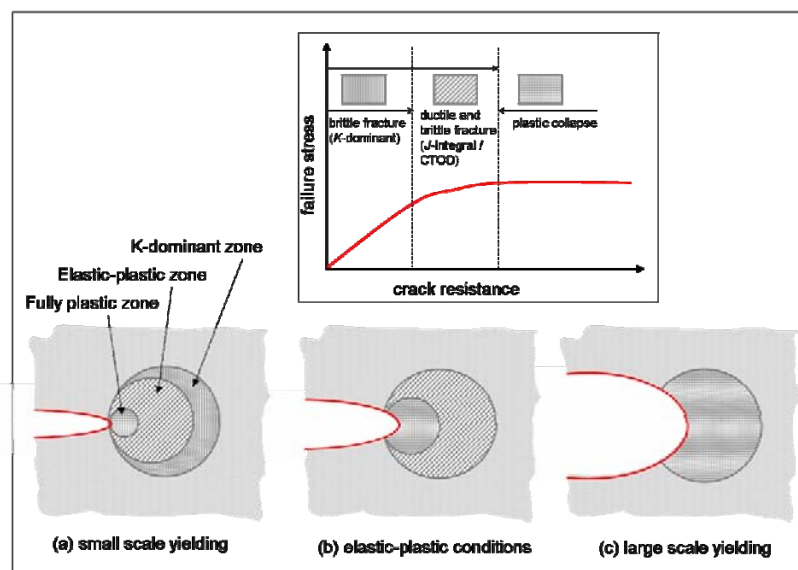


Fig. 1.6: Crack tip condition [10]

From Equ. (1.21), it is observed that the singularity, as $r \rightarrow 0$, can be interpreted by the formation of small scale yielding at the crack tip. Using the stress field equations and a yield criterion, the size of

the plastic zone can be obtained in terms of yield strength and stress intensity factor. According to Irwin [26], for Mode-I crack it is given by for plane stress and plane strain states, respectively, as

$$\omega = \frac{K^2}{\pi\sigma_y^2} \quad \text{Equ. (1.23)}$$

$$\omega = \frac{K^2}{\pi\sigma_y^2}(1-2\nu)^2 \quad \text{Equ. (1.24)}$$

Another widely used model has been given by Dugdale [28] for plane stress conditions. According to Dugdale's analysis, the size of the plastic zone is

$$R \cong \frac{\pi}{8} \left(\frac{K}{\sigma_y} \right)^2 \quad \text{Equ. (1.25)}$$

Comparing Equ. (1.23) and Equ. (1.25) , it can be seen that $R \approx 1.23 \omega$, which means that both models give reasonably close estimates.

Two other fracture mechanics parameters are the crack tip opening displacement CTOD and the J -integral. The former was proposed by Wells [29], stating that the fracture behaviour in the vicinity of a sharp crack could be characterized by the crack tip opening displacement. As the CTOD measurement can be made even when there is considerable plastic flow ahead of the crack tip, this can be used to establish critical design stresses or critical crack sizes similar to that of LEFM also for large scale yielding.

For a centre crack in a wide plate, the mode-I CTOD δ is related to K via

$$\delta = \frac{K^2}{E\sigma_y} \quad \text{Equ. (1.26)}$$

The J -integral proposed first by Rice [30] characterizes the stress-strain field at the crack tip by an integral path that is sufficiently far from the crack tip for being amenable to a purely elastic analysis. Thus, similarly to the CTOD, the J -integral can also be used for describing the fracture characteristics of materials exhibiting elastic-plastic behaviour. For the linear-elastic (Mode I loading) case, the J -integral is identical to the energy release rate per unit crack extension and follows from K and the elastic parameters E , ν as [10]

$$J = \frac{(1-\nu^2)K^2}{E} \quad \text{(Plane strain)} \quad \text{Equ. (1.27)}$$

$$J = \frac{K^2}{E} \quad \text{(Plane stress)} \quad \text{Equ. (1.28)}$$

For the design of engineering components containing cracks it is important to obtain the critical values at failure in the form of K_c (fracture toughness), critical CTOD δ_c , or critical value of the J -integral J_c . Many testing standards such as ASTM provide guidelines for obtaining these parameters.

For the design of components containing defects or cracks, the criterion is to keep either the applied stress level σ or the crack size a as low as to ensure that $K = Y\sigma\sqrt{\pi a} < K_{Ic}$.

The LEFM method based on SIF values K can also be adapted for fatigue loading. In this case, the static fracture criterion corresponds to the onset of catastrophic failure; i.e., final rupture occurs if the maximum SIF in one cycle K_{max} approaches the fracture toughness K_{Ic} , $K_{max} = K_{Ic}$. Prior to final rupture, however, there is a long phase of cyclic stable crack growth. Thus, the fatigue crack growth behaviour can be divided into three regions, cf. Fig. 1.7: region I corresponds to the fatigue crack growth threshold ΔK_{th} , below which cracks do not propagate under cyclic loading [32].

Microstructure, mean stress, frequency and environment mainly control region I. Region II represents stable fatigue crack growth. For this regime, the crack growth behaviour may be approximated by a linear relationship in the $\log(da/dN)$ versus $\log(\Delta K)$ plot as given by the Paris relation [34]

$$\frac{da}{dN} = C(\Delta K)^m, \quad \text{Equ. (1.29)}$$

where m is the slope of the fatigue crack growth (FCG) line and C is a coefficient of proportionality. Both m and C depend on the material. ΔK is the stress intensity factor range given by

$$\Delta K = Y\Delta\sigma\sqrt{\pi a}. \quad \text{Equ. (1.30)}$$

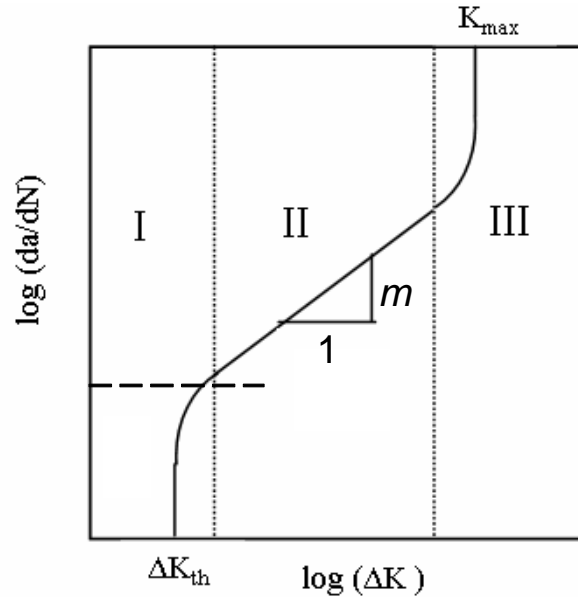


Fig. 1.7: A typical fatigue crack growth curve

In region II, stable macroscopic crack propagation takes place, and the crack growth is generally dependent on the environment. Microstructure and mean stress³ have less influence on the fatigue crack growth behaviour in region II compared to region I [1].

In region III, as mentioned before, the fatigue crack growth rates are very high. This region is delimited by the fracture toughness K_{Ic} , as the growth rate approaches infinity at final rupture.

For the characterization of the fatigue crack growth behaviour, a number of relationships have been developed over the years. The simplest relation is due to Paris, Equ. (1.29). Nevertheless, this equation does not consider the influence of the mean stress on crack growth. Likewise, the asymptotic behaviour in regions I and III is also missing. Various proposals for accounting for such effects can be found in the literature; in what follows the most common ones are described briefly.

The effect of mean stress on the fatigue crack growth rate is introduced by considering the stress ratio R . A schematic general representation of such effects is shown in Fig. 1.9 [35]. One of the concepts used for explaining the effect of stress ratio on the fatigue crack growth is that of *crack closure*. In Fig. 1.8, this has been shown with respect to the threshold regime. The lack of crack closure effects at higher stress ratios R results in lower threshold values ΔK_{th} , Fig. 1.9b.

³ Mainly for the tensile part of the cycle

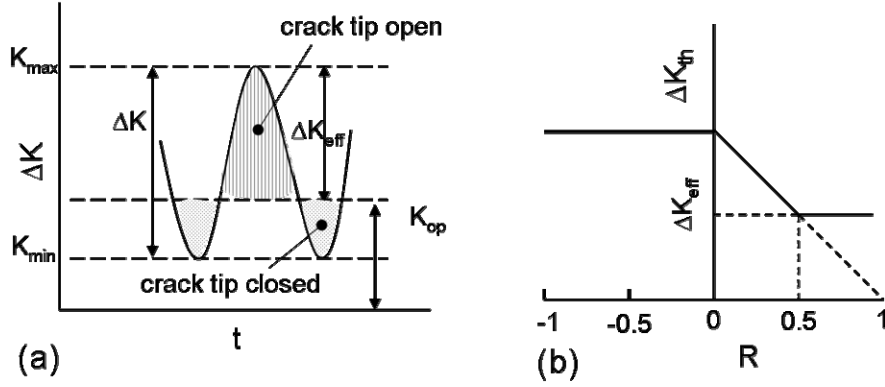


Fig. 1.8: (a) Crack closure effect [5], (b) effect of R ratio on threshold SIF [31]

For the mean stress effect in regions II and III, Forman [39] proposed a function which is now commonly used,

$$\frac{da}{dN} = \frac{C(\Delta K)^m}{(1-R)K_c - \Delta K} = \frac{C(\Delta K)^m}{(1-R)(K_c - K_{\max})}. \quad \text{Equ. (1.31)}$$

As K_{\max} tends to approach the fracture toughness value K_{Ic} , the growth rate goes to infinity, meaning that the upper vertical asymptote in the crack growth behaviour is also incorporated in this equation in addition to the load ratio effect.

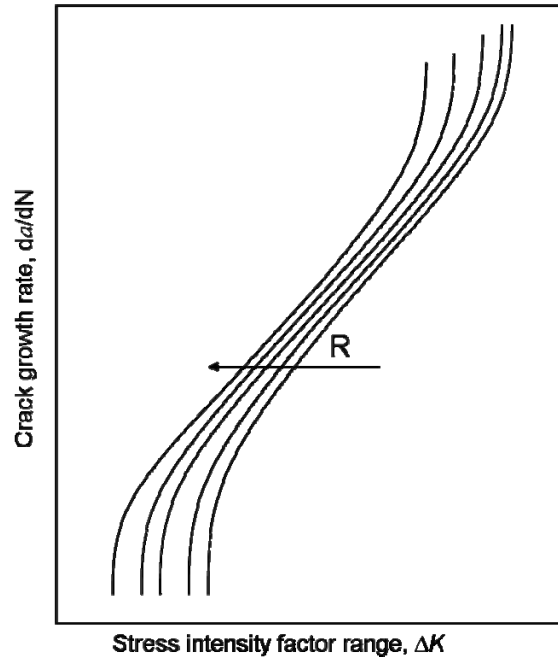


Fig. 1.9: Schematic mean stress effect on fatigue crack growth rates

Furthermore, the lower vertical asymptote can be included by introducing the threshold stress intensity factor range ΔK_{th} into Equ. (1.31) as given by [40]

$$\frac{da}{dN} = C \left[\frac{\Delta K - \Delta K_{th}}{\Delta K_c - K_{\max}} \right]^m, \quad \text{Equ. (1.32)}$$

where ΔK_{th} is a function of stress ratio and can be obtained by [41]

$$\Delta K_{th,R} = \Delta K_{th0}(1-R)^\gamma. \quad \text{Equ. (1.33)}$$



Similar functions for the crack growth behaviour have been proposed by Elber, Walker, Kujawski and many others, [42]-[46]. A more recent equation for the complete description of fatigue crack growth has been given by Kohout [46],

$$\frac{da}{dN} = CK_c^n \left(\frac{\Delta K}{(1-R)^\gamma} \right)^{m-p} \left[\frac{\{(\Delta K(1-R)^{-\gamma})^p\} - \Delta K_{th0}}{\{K_c^n - (\Delta K(1-R)^{-1})^n\}} \right], \quad \text{Equ. (1.34)}$$

where p , n and γ are fitting parameters. The parameter p defines the curvature of the crack growth path between regions I and II, and parameter n defines the curvature between regions II and III. The exponent γ defines the influence of the R ratio on the threshold SIF range and is an empirical constant fitted to test data for non-zero positive R values; its effect is similar to that of the exponent γ in Equ. (1.33).

2. Codes and Standards for Damage Tolerant Design

2.1. General description

The conventional design against fatigue is based on the assumption that the material is an ideally homogeneous, continuous, isotropic continuum free from defects and flaws. On the other hand, many engineering structures contain crack-like defects or imperfections which can arise during manufacturing, operation or maintenance. As discussed previously, the former postulate leads to the use of safe-life approaches, either for finite life (LCF/HCF) or for infinite life (dimensioning against the endurance limit). However, in the presence of flaws, the design should rather be based on the damage tolerant design (DTD) method, which ensures that that the inherent defects may not grow up to the point of failure, either during the entire design life or during inspection periods. Fig. 2.1 shows a classification which includes both conventional and damage tolerant design approaches, providing a common systematics for all of the basic methods outlined in the previous chapter.

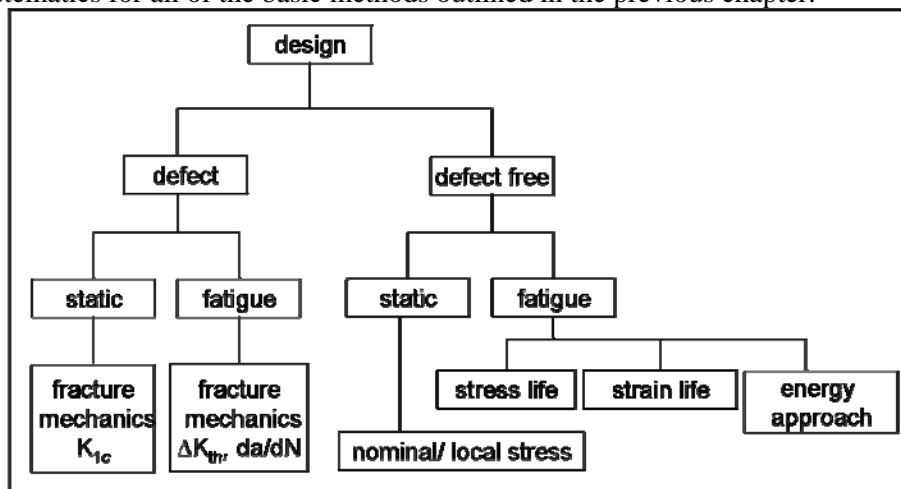


Fig. 2.1: Classification of design approaches

Depending on the application, component type and loading conditions, there may be different failure mechanisms such as static, fatigue, creep, corrosion, buckling etc. responsible for damage. Over the years, a number of methodologies and design guidelines have been developed to cover these damage modes. For the safe-life design approach such guidelines are provided in codes like BS 7608, ASME Boiler and Pressure Vessel (BPV) Code Sections III and VIII, the FKM Guideline for Analytical Strength Assessment etc. For a defect-free material under static loading these guidelines follow the yield criterion corrected by adjustment factors; for fatigue loading, the fatigue strength of smooth, polished specimens of standard diameter serves as a basis, corrected by different reduction factors such as size, surface finish, stress concentration, type of loading etc. The maximum allowable values calculated thereby must exceed the applied stresses for a component to be safe.

If, on the other hand, a flaw is found in a structure during inspection, crack growth – i.e., damage tolerance – considerations must be applied. In general, a damage tolerance evaluation conforming to the particular design code is required to decide about the further use or removal of the specific part or structure. Such procedures are termed fitness-for-service (FFS) or damage tolerant design (DTD) procedures. A variety of such codes exists for the structural integrity assessment of components containing crack-like flaws. Among others, these include R6, BS 7910, API 579, GE-EPRI, SINTAP, FITNET, the FKM Fracture Mechanics Assessment Guideline, and the ASME BPV Code Section XI. Some of these codes are purely for static loading (e.g., SINTAP). Others provide also guidelines for fatigue loading (e.g., BS 7910 and ASME BPV). A general comparison of the most commonly used procedures for static and fatigue assessment may be found in Tab. 2.1.

Design code	Failure mode		Remarks
	Fracture	Fatigue	
R6, R5 [95] [96]	✓	✓	British power generation industry
SINTAP [94]	✓	-	General European procedure
FITNET [99]	✓	✓	General European procedure, follow-up to SINTAP
GE-EPRI [110]	✓	-	General working methodology [109]
API 579 [98]	✓	✓	Pressure vessels, piping, tanks
ETM [103]	✓	-	General
ASME XI [53]	✓	✓	Nuclear power plants
BS 7910 [50]	✓	✓	Offshore, pressure vessels, pipelines
FKM [104]	✓	✓	General industry, compilation of BS 7910 and SINTAP

Tab. 2.1: Comparison of DTD procedures

2.1.1. Philosophy of assessment methodologies

DTD/FFS methods compare the applied and material side based on the crack tip parameters such as the linear-elastic stress intensity factor K , the crack tip opening displacement CTOD or the J -integral. Thus, the fracture behaviour of a component is estimated in terms of the critical crack dimension or the critical applied loading. If the deformation behaviour of the structure is linear-elastic, then the crack driving force parameter is K . For a number of crack and component geometries, K solutions can be obtained from the respective codes or from stress intensity compendia (e.g., [27]). However, if a structural component is under such loading so that the response is elastic-plastic, a J -integral or CTOD approach must be applied. Again, for many cases closed form solutions are available in handbooks like [27] or [48]. Additional finite element analyses may be needed for complex geometries.

2.1.2. Flaw selection and re-characterization

The underlying principle of all DTD/FFS assessment codes is the presence (or assumption) of an initial flaw. The procedures are centred on evaluating the acceptance of such flaws either found during inspection or assumed as worst-case flaws (e.g., corresponding to the NDT detection limit) in the design phase of a component. One of the major steps in such an assessment is the classification of the flaw type. A real flaw may be of complex shape; however, there exist certain guidelines in different codes due to which a conservative shape can be easily selected. The flaws are characterized as

- Non-planar flaws: cavities, solid inclusions, local thinning
- Planar flaws: cracks, lack of fusion or penetration, undercut

Fig. 2.2 depicts exemplarily a complex flaw which may be separately characterized by the superposition of an extended, part-through flaw and a semi-elliptical flaw in a section of reduced thickness [50].

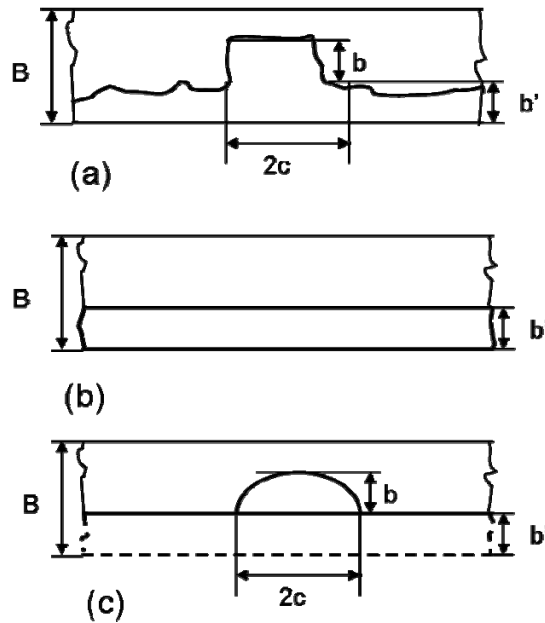


Fig. 2.2: Flaw re-characterization: a complex flaw (a) is separately assessed as two simple flaws (b) and (c) [50].

2.2. Static failure assessment

For static failure, the structural integrity codes are based on the following two principal methods of analysis [47]:

- Failure assessment diagram (FAD)
- Crack driving force (CDF)

Both concepts are analogous, stemming from a combination of a fracture mechanics assessment based on the stress intensity factor, and a plastic limit load analysis.

2.2.1. Basic methods

2.2.1.1. Failure assessment diagram (FAD)

Codes like R6, BS 7910, API 579 and SINTAP use the FAD method [49]. In its simplest form, a geometry-independent failure line is given by normalizing the crack tip loading to the fracture toughness of the material. For a safety assessment, the geometry and load dependent assessment (design) point is compared to this failure line [47]. A component is said to be safe if the assessment point lies within the area below the failure line. A position of the design point above the failure line is said to be critical, and the component is potentially unsafe in this case. The elastic parameter is accounted for by using the fracture ratio

$$K_r = \frac{K_I}{K_{Ic}} \quad \text{Equ. (2.1)}$$

Similarly, the plastic parameter is obtained from the ratio of applied to the plastic limit load,

$$S_r = \frac{F}{F_L} \quad \text{Equ. (2.2)}$$

2.2.1.2. Crack driving force (CDF)

Certain standards such as GE-EPRI, ETM and SINTAP use the CDF methodology [49]. In contrast to the FAD, this method considers the J -integral or CTOD as single applied load parameter, which is then compared to the material resistance. ETM, e.g., gives formulas for contained yielding ($\sigma \leq \sigma_y$) and for the fully plastic case ($\sigma \geq \sigma_y$). In contained yielding, usually a linear-elastic analysis is performed. For the fully plastic regime, the material stress-strain behaviour is obtained by the power law for $\sigma \geq \sigma_y$,

$$\frac{\sigma}{\sigma_y} = \left(\frac{\varepsilon}{\Delta\varepsilon} \right)^n, \quad \text{Equ. (2.3)}$$

with the help of which a relation between the applied load δ (or J) and the material resistance δ_{mat} or J_{mat} is established,

$$\frac{\delta}{\delta_y} = \left(\frac{F}{F_y} \right)^{1/n} = \left(\frac{J}{J_y} \right)^{1/(1+n)}. \quad \text{Equ. (2.4)}$$

An outline and comparison of some of the most widely used codes is presented in what follows.

2.2.2. BS 7910

The British Standards code BS 7910 provides a guideline for determining the acceptability of flaws in metallic structures. The fracture assessment consists of three levels, depending on the available information and depth of analysis:

- *Level 1:* only limited material information is available
- *Level 2:* general assessment rule in which the assessment line is obtained from the true stress-strain behaviour of the material
- *Level 3:* for ductile materials enabling tearing resistance analysis. In this case, the fracture toughness is needed in the form of δ or J vs. crack extension curves (the so-called resistance curves, or R-curves).

The assessment follows the FAD concepts, where the ratio of applied load vs. fracture load is plotted against applied load vs. plastic collapse load.

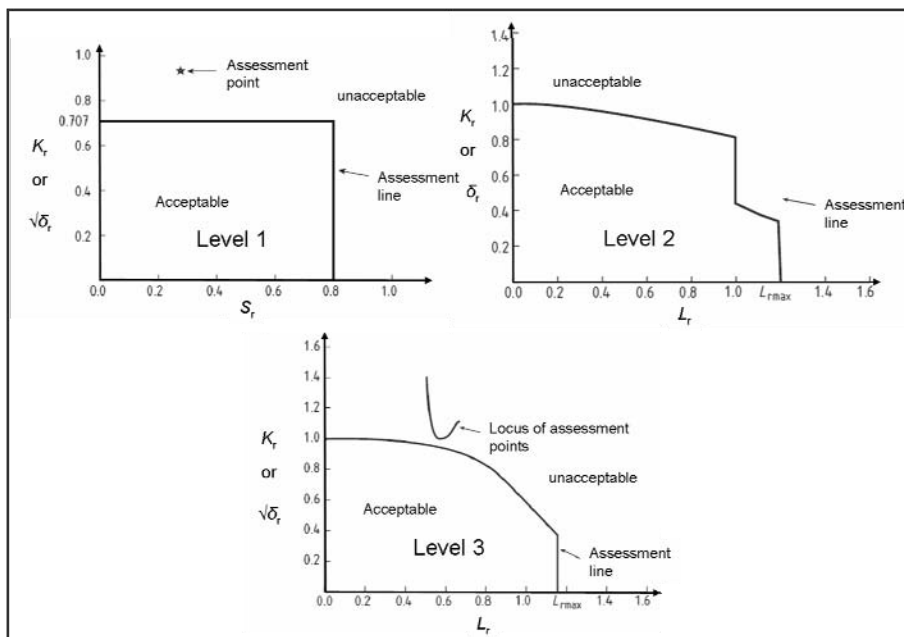


Fig. 2.3: Different assessment levels according to BS7910 [50]

2.2.3. ASME BPV Section XI

ASME BPV Section XI Appendix A [53] provides procedures for assessing the acceptability of flaws that have been detected during in-service inspection and which exceed a specified allowable value. The method is based on linear-elastic fracture mechanics and mainly applies to ferritic materials of a thickness of 4 inch (≈ 100 mm) or more, with a minimum yield strength of 50 ksi (≈ 345 MPa).⁴ A brief summary of the procedure is as follows:

- Obtain the actual flaw configuration and characterize it into simple shapes representative of the actual severity of the actual defect using flaw re-characterization techniques given in the code.
- Determine the stresses and stress intensity factors for the observed flaw for different conditions such as normal, emergency or faulted. Equations for surface or subsurface flaws are provided, incorporating primary as well as secondary (residual) stresses.
- Determine the necessary material properties such as K_{Ic} (fracture toughness) and K_{Ia} ⁵ – value of stress intensity shortly after crack arrest followed by dynamic or impact loading⁶. The code provides the lower bound curves of these properties as a function of temperature for different grades of steel. The approximations to these curves are

$$K_{Ic} = 33.2 + 20.734 \exp[0.02(T - RT_{NDT})] \quad \text{Equ. (2.5)}$$

and

$$K_{Ia} = 26.8 + 12.445 \exp[0.0145(T - RT_{NDT})] \quad \text{Equ. (2.6)}$$

where RT_{NDT} is the nil ductility temperature in $^{\circ}F$ and K_{Ic} and K_{Ia} are in $\text{ksi}\sqrt{\text{in}}$. However, it is to be noted that these curves will give conservative values; it is recommended to extract these values from tests on specimens of the actual material.

- The final step is to compare the K_I values computed for different loading conditions prescribed in the code to K_{Ic} or K_{Ia} . The minimum critical flaw size a_i for different operational conditions is obtained using K_{Ic} data for fracture initiation considerations and K_{Ia} data for flaw arrest considerations.

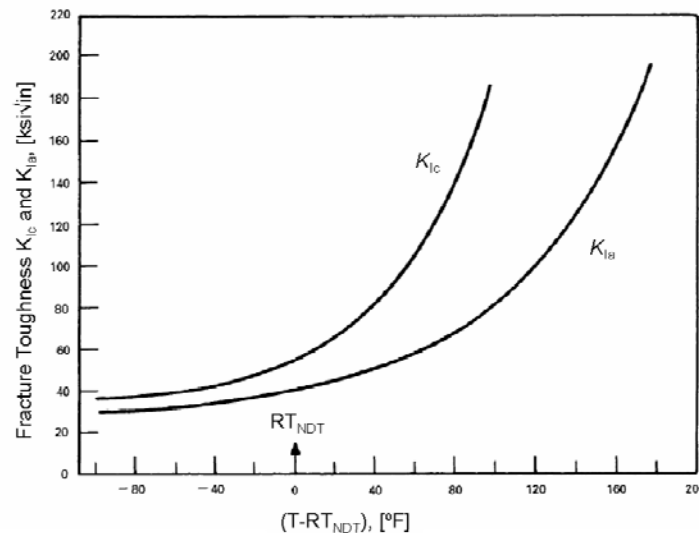


Fig. 2.4: ASME lower bound K_{Ia} and K_{Ic} test data for various grades of steel [54]

⁴ Clearly, this standard is custom-tailored to serve the U.S. power generation and piping industrial environment.

⁵ Linear-elastic behaviour during dynamic or impact loading results in rapid unstable brittle fracture. K_{Ia} can be obtained using ASTM E-1221 [32]

⁶ K_{Ia} and K_{Ic} represent the critical values of SIF K_I . K_{Ia} is based on the lower bound of crack arrest, whereas K_{Ic} is based on the lower bound of static fracture. The critical K_I values are temperature dependent in order to account for the ductile-brittle transition observed in ferritic steels.

2.2.4. SINTAP

SINTAP is the procedure for the assessment of flaws that mainly considers brittle fracture and ductile tearing failure modes. The procedure has been obtained by using the experiences of R6, BS 7910 and the ETM model [94]. Both FAD and CDF routes are incorporated, and calibrated such as to give identical results.

A range of assessment options is provided within the code, depending on data availability and analysis requirements. The different options are summarized as follows:

Default level (Level 0): the simplest case, which is used when only the yield strength is available.

Standard levels:

Level 1: uses the yield and tensile strength of the material without any weld effects

Level 2: additional assessment of weld mismatch effects

Level 3: considers the full stress-strain curve of the material

Advanced levels:

Level 4: allows for the loss of constraint in thin sections or predominantly tensile loading

Level 5: *J*-integral analysis requiring numerical cracked body analysis

Level 6: special case of leak-before-break for piping and pressure vessel applications

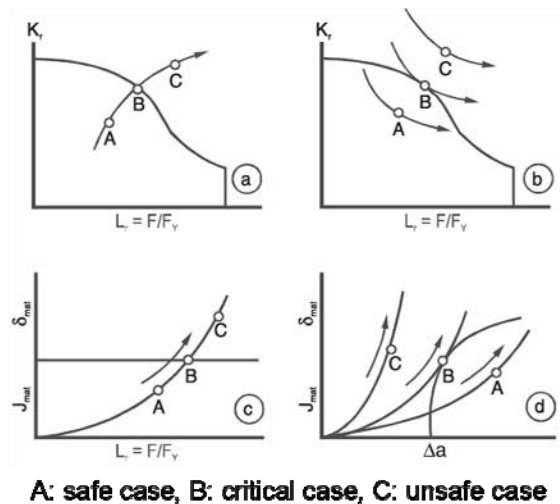


Fig. 2.5: SINTAP FAD and CDF approaches for crack initiation and ductile tearing analysis. (a), (c): FAD and CDF with fracture initiation, (b), (d): FAD and CDF with ductile tearing [94]

2.2.5. FITNET

The FITNET fracture module is a follow-up to the SINTAP European project incorporating recent developments in R6 and BS 7910 [51]. The methodology is based on the CDF and FAD concepts. Similar to SINTAP, the key aspect of the procedure is that a range of assessment routes can be followed reflecting the quality of available input data.

2.3. Fatigue failure assessment

As for static loading, one of the major steps in a fatigue assessment is the characterization of a present or presumed flaw.

For planar flaws, fracture mechanics principles are used. Fatigue crack growth analysis is performed for such defects, i.e., the fatigue life is estimated by integrating the crack growth laws.

For the case of non-planar flaws or if the defect is of volumetric type (e.g., local thinning or bad weld quality), the situation is dealt with based on modified S-N curves [50]. Thus a nominal stress approach is applied using a set of S-N curves classified according to different levels of fatigue resistance corresponding to different local geometry, weld condition, or microstructure; these so-called quality S-N curves are obtained from statistical analysis of tests performed on standard weld details [52]. – Alternatively, for a still more conservative analysis, non-planar flaws can also be taken as planar flaws.

2.3.1. BS 7910

In the British Standards code, the flaw classification is based on non-planar and planar as described above. Two methods are incorporated for an assessment of planar flaws – (i) a general procedure which allows the use of accurate expressions for the cyclic stress intensity factor and specific fatigue crack growth data, (ii) a simplified procedure in which the flaws are assessed on the basis of quality S-N curves).

It is recommended to determine the crack growth law experimentally. The crack growth may be approximated by a single slope m or two slopes m_1 and m_2 in the central portion of a sigmoid-shaped curve. For most cases, a Paris law Equ. (1.29) is applied. For $\Delta K < \Delta K_{th}$, the crack growth rate da/dN is zero. The applied stress intensity factor range ΔK , Equ. (1.30) is substituted into Equ. (1.29) to get the total life after (numerical) integration.

For situations where the crack growth near the threshold is significant, a less conservative form of Equ. (1.29) based on the effective value of ΔK , ΔK_{eff} , is suggested. Thus, the relevant equation become

$$\frac{da}{dN} = C(\Delta K_{eff})^m, \quad \text{Equ. (2.7)}$$

where at temperatures up to 100 °C, the proximity of threshold, ΔK_{th} , is used such that for $\Delta K < \Delta K_{th}/R$

$$\Delta K_{eff} = \frac{(\Delta K - \Delta K_{th})}{(1 - R)} \quad \text{Equ. (2.8)}$$

The major steps for the assessment of planar flaws in BS 7910 are briefly summarized as follows:

- Obtain the da/dN vs ΔK relation and the relevant value of ΔK_{th} . For elliptical flaws, the same relationship is assumed to be applicable in both depth b and width c directions.
- Determine the relevant stress range including stress concentrations due to gross discontinuities (the stress concentration due to local discontinuities is taken as part of the stress intensity factor). The stresses are further identified as primary stress P or secondary stress Q depending on the conditions.
- Obtain the stress intensity factor range corresponding to the applied stress range for the given or assumed flaw dimension and position.
- Estimate the growth of the crack (Δa and Δc) for one cycle from the value of ΔK .
- Using the peak value of the tensile stress in the cycle, obtain the stress intensity factor corresponding to the new size of the crack.
- Compare the increment in crack length or stress intensity factor to the limiting values.

2.3.2. ASME BPV Section XI

Similar to the static fracture case, the ASME BPV Section XI [53] also provides a guideline for a fatigue crack growth assessment. In Appendix A (article A-4300), a set of reference fatigue crack growth curves is given for carbon and low ferritic steels in air and wet environment. The crack growth

rate is characterized in terms of the applied stress intensity range ΔK_I and is given as in Equ. (1.29). It is suggested to obtain the real data from specimens corresponding to the actual material and product form, considering various variables such as environment, frequency and material variability. For carbon and low ferritic steels, the reference fatigue crack growth curve is provided as follows:

For a dry (air) environment (or subsurface flaws), the crack growth rate is given according to Equ. (1.29) with $m = 3.07$ and

$$C = 1.99 \times 10^{-10} S, \quad \text{Equ. (2.9)}$$

where S is a scaling parameter to account for the mean stress effect such that for $0 \leq R \leq 1$,

$$S = 25.72(2.88 - R)^{-3.07}. \quad \text{Equ. (2.10)}$$

Similarly for $R < 0$, value of scaling parameter has been given as $S = 1$. Reference fatigue crack growth curves for dry environment, given by Equ. (1.29) and Equ. (2.9) are shown in Fig. 2.6.

A similar procedure is also provided for obtaining the crack growth behaviour in water environment. However, the use of these reference fatigue curves is only recommended in cases where the actual material data is not available.

The degree of conservatism of these reference curves has been discussed by many researchers [55] [56]. In case of air environment, the reference crack growth is mostly (!) on the safe side. However, in [56] it is reported that in certain wet conditions such as HWC⁷ (Hydrogen water chemistry), the ASME reference crack growth curves are clearly non-conservative.

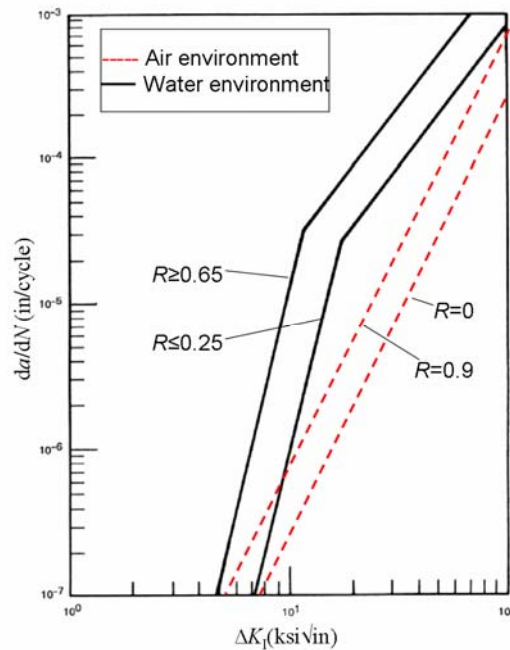


Fig. 2.6: ASME reference fatigue crack growth curves for carbon and low ferritic steels in air and water environments [54]

2.3.3. FKM fracture mechanics guideline

The FKM fracture mechanics guideline provides guidance for defect assessment under static as well as fatigue loading. It follows the formulations based on SINTAP and BS7910. Under static loading, the guideline uses the FAD and CDF approaches. For fatigue crack growth, the Paris equation is followed.

⁷ Hydrogen is added to feed-water in boiling water reactors (BWR) to reduce stress corrosion cracking, which changes the chemistry from normal water (NWC) to hydrogen water chemistry (HWC).

2.3.4. FITNET

The FITNET fatigue module [52] again offers different assessment routes for the aforementioned non-planar and planar flaw conditions.

In the case of non-planar flaws, a nominal stress approach is applied using S-N curves for welded joints. For variable load spectra, the linear damage accumulation law Equ. (1.9) is used. Alternatively, for conservative results, the flaw can be taken as planar and assessed as described below.

For planar flaws, recommendations are provided for two cases – un-welded and welded.

For the non-welded case, the NASGRO fatigue crack growth equation (Forman and Mettu) is used:

$$\frac{da}{dN} = C \left[\left(\frac{1-f}{1-R} \right) \Delta K \right]^m \frac{\left(1 - \frac{\Delta K_{th}}{\Delta K} \right)^p}{\left(1 - \frac{K_{max}}{K_c} \right)^q}, \quad \text{Equ. (2.11)}$$

where f is the ratio of opening vs. maximum stress intensity range.

For the assessment of flaws in welded structures, or for unwelded cases where the parameters for an application of Equ. (2.11) are not available, Equ. (2.11) is reduced to the standards Paris law, Equ. (1.29) .

The major consideration for the flaws is that they are treated as long cracks. Thus, if ΔK is below a certain determined value, the crack growth rate is expected to be negligible. In order to provide estimates of crack growth over a particular number of cycles or to estimate the number of cycles required to reach a critical crack size, the crack growth equations Equ. (2.11) and Equ. (1.29) are integrated numerically.

2.4. Residual stresses

One of the most important factors in the structural assessment of welded components is the consideration of residual stresses. Due to the fact that they can lead, in combination with the applied stresses, to accelerated fatigue crack growth, they are of major importance. There exist certain methods for residual stress relief, such as shot peening or post-weld heat treatment (PWHT); nevertheless, the FFS/DTD codes provide guidelines for a conservative assessment of such residual stresses [83].

In many codes residual stresses are regarded as secondary stresses. The R6 and BS7910 codes classify residual stress distributions into two types

1. *As-weld conditions*: For a wide variety of plates and joint configurations, residual distributions are given in Annex Q of BS 7910). For cases where no distribution is available, it is assumed to be uniform and is taken to be the lesser of

$$\sigma_{res} = \sigma'_y \quad \text{Equ. (2.12)}$$

and

$$\sigma_{res} = \left(1.4 - \frac{\sigma_{ref}}{\sigma_f} \right) \sigma'_y, \quad \text{Equ. (2.13)}$$

where σ_{res} is the residual stress and σ'_y the yield strength of the material in which the flaw lies for a flaw lying in a plane transverse to the welding direction (i.e., the stresses to be considered are parallel to the weld), and σ_{ref} is the reference stress used for plastic collapse case, and σ_f is the flow stress (the arithmetic average of yield stress and ultimate tensile strength).



2. *Post-weld heat treatment (PWHT) conditions:* In a structure subjected to PWHT, the residual stresses will not be reduced to zero completely. In the absence of measured data, the residual stresses are assumed to be

- 30% of the yield strength of the material in which the defect is located for stresses parallel to the weld and
- 20% of the lower of yield strengths of the weld and base material for stresses transverse to the weld.
- In case of uncontrolled heat treatment, as-weld values are to be taken.

These conditions are applied in different ways in various levels of assessment:

- *Level 1:* As-weld condition is applied for the residual stress distribution.
- *Level 2:* For obtaining the K_r (Equ. (2.1)) for the FAD, the residual stress intensity factor is added to the applied stress intensity factor.
- *Level 3:* For this case, the residual stress distribution is obtained from numerical simulations.

3. Development of Consistent Engineering Estimates for DTD in Fatigue

3.1. Short and long cracks

The classical approaches for dimensioning against fatigue assume components to be free of defects. However, the fact that many engineering components contain flaws, e.g., in the form of inclusions, porosity or manufacturing imperfections, has led to the development of the damage tolerant design approach. In the case of fatigue loading, the aim of this design method is to guarantee that pre-existing cracks will not propagate to failure. The early work of Paris [34] has led to the utilization of the stress intensity factor range ΔK_I for the assessment of fatigue crack propagation by means of the crack growth law Equ. (1.29). Since then, many more equations for describing the fatigue crack growth rate above the threshold have been formulated (cf. Chapter 1).

All these relations are valid for cracks exceeding a certain minimum length – so-called *long cracks*. Thus the lower asymptote (Fig. 1.7) corresponds to the *long crack threshold* ΔK_{th} . However, for certain short cracks this framework breaks down due to microstructure, plasticity and crack closure effects, resulting in a growth rate that is significantly higher than for long cracks. Pearson [63] and Kitagawa [64] were among the first to show that small cracks (less than 0.5 mm in metals) grow faster than long cracks if correlated against the stress intensity factor range [66].

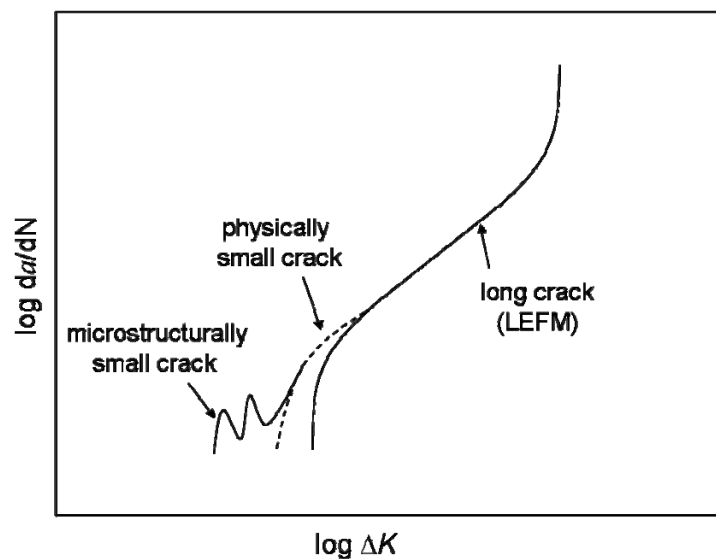


Fig. 3.1: Schematic of typical crack growth rate behaviour of small and long cracks [1]

The different mechanisms influencing the crack growth threshold may of an intrinsic as well as of an extrinsic nature. The former corresponds to the inherent resistance of the material against fatigue crack growth propagation at a certain crack driving force. The latter mechanism is due to shielding of the crack tip as a result of crack-related (as opposed to material-related) mechanisms, such as crack closure, crack branching and crack bridging [57]. Following this categorization, small cracks are categorized as follows [1] [57] [58] (see also Fig. 3.1):

Microstructurally small cracks: In this case, the length of the crack is comparable to the microstructural dimensions such as grain size. Crack growth occurs along the weakest paths, and local retardation or arrest can occur at microstructural barriers such as grain boundaries.

Mechanically small cracks: For such cracks, the length is small compared to the scale of local plasticity, i.e., the plastic zone ahead of the crack tip exceeds the K -dominated field. Thus the framework of linear-elastic fracture mechanics (small scale yielding) breaks down.

Physically small cracks: Cracks smaller than a multiple of grain diameters are called *physically small*. As the cracks grow through several grains, the microstructural influences die out, leading to a more homogeneous crack growth behaviour.

3.2. Different DTD methodologies for fatigue

Various models have been proposed for predicting the fatigue strength of materials containing defects. A detailed outline of these models is described in [62], which classifies them into three different groups:

- Models based on empirical results
- Models based on fatigue notch factors
- Models based on fracture mechanics

The Frost model is one of the examples of the empirical methods. According to Frost [62], the fatigue limit σ_f is obtained from

$$\sigma_f^3 l = C, \quad \text{Equ. (3.1)}$$

where l is the depth of the crack. Similarly, other models (like Mitchell's or Nordberg's [62]) use Peterson's empirical equation [62] for small cracks (although Peterson's equation was originally proposed for large notches!)

$$\sigma_f = \frac{\sigma_0}{[1 + (K_t - 1)/(1 + C'/\rho)]}, \quad \text{Equ. (3.2)}$$

where C' is a material constant depending on the ultimate strength, ρ is the tip radius of a geometric discontinuity, and K_t is the stress concentration factor.

However, the most used methods for predicting the life of flawed components are those from fracture mechanics, where it is assumed that defects or flaws can be characterized as cracks. The crack tip parameter K_I and the threshold for fatigue crack growth ΔK_{th} are used to obtain an estimate of the fatigue strength for materials containing defects. Kitagawa and Takahashi presented the stress versus crack length diagram to characterize quantitatively the fatigue threshold behaviour of small cracks, i.e., the breakdown of the LEFM-based threshold condition for short cracks. According to them, there exists a transition crack length, below which ΔK_{th} is smaller than that for long cracks. This length parameter is dependent on the material microstructure. Thus, the overall dependence of the threshold stress intensity range on the crack length is characterized by a ΔK_{th} versus crack length a plot. Alternatively, the same behaviour may be described by a threshold stress range $\Delta\sigma_{th}$ against crack length a plot – commonly known as Kitagawa diagram. Fig. 3.2 shows schematically two K-T diagrams where both the threshold stress intensity range ΔK_{th} against the crack length a and the stress range at the threshold of the crack growth range $\Delta\sigma_{th}$ against the crack length a are described.

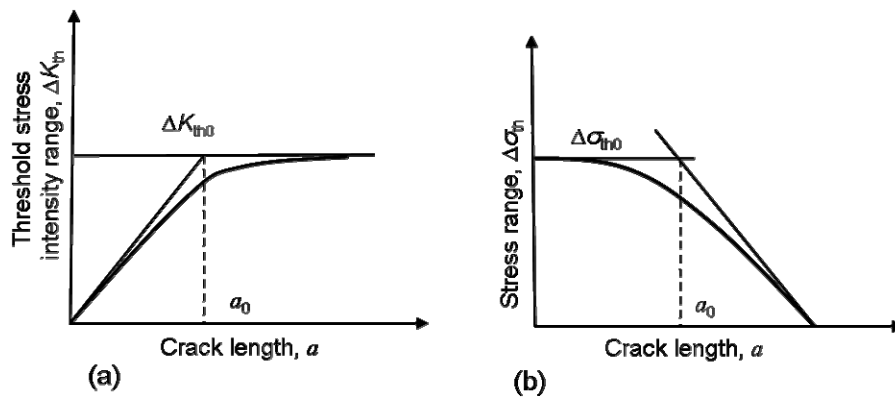


Fig. 3.2: K-T diagram: (a) threshold stress intensity range as a function of crack length; (b) stress range at the threshold of crack growth as function of crack length (schematic) [67]

Various examples of the Kitagawa-Takahashi (K-T) diagram can be found discussing weld metals, foreign object damage and fretting fatigue (e.g., [59]). Similarly, many modifications of the K-T model have followed their study. “[60],[61]” shows a typical K-T diagram showing the threshold between propagating and non propagating cracks. Here the effect of short cracks is shown with reference to the microstructural size. Even if the applied stress is smaller than the smooth specimen fatigue limit, cracks of the order of the microstructural length scale will start growing and will be arrested.

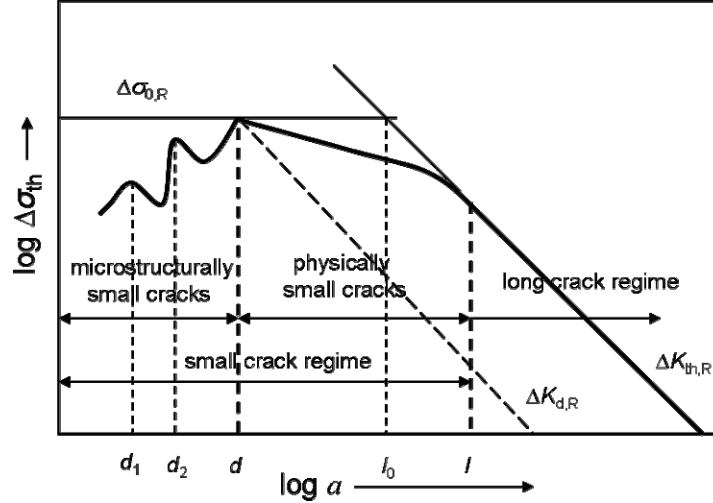


Fig. 3.3: K-T diagram showing threshold between propagating and non-propagating cracks [60]

The transition length has been approximated by El Haddad *et al.*[65] defining l_0 as an *intrinsic crack size*. As a first order approximation, cracks smaller than this length are assumed to be non-propagating. The intrinsic crack size is used for modifying the conventional LEFM equation as follows:

$$\Delta K_{th,lc} = \Delta \sigma_{lim} Y \sqrt{\pi(a+l_0)}, \quad \text{Equ. (3.3)}$$

where $\Delta K_{th,lc}$ stands for the fatigue crack growth threshold SIF range obtained for long cracks, the $\Delta \sigma_{lim}$ denotes the fatigue limit in the presence of a crack of length a , and Y is some geometry factor. This is called the concept of the effective crack length, which is the sum of the real crack length a and the intrinsic crack size l_0 .

On the other hand, the original LEFM equation must be used in conjunction with a crack length dependent threshold value ΔK_{th} if it is to be used with short cracks:

$$\Delta K_{th} = \Delta \sigma_{lim} Y \sqrt{\pi a} \quad \text{Equ. (3.4)}$$

or

$$\Delta \sigma_{lim} = \frac{\Delta K_{th}}{Y \sqrt{\pi a}} \quad \text{Equ. (3.5)}$$

Combining Equ. (3.3) and Equ. (3.4) we get

$$\Delta K_{th} = \frac{\Delta K_{th,lc}}{\sqrt{1 + \frac{l_0}{a}}} \quad \text{Equ. (3.6)}$$

where $\Delta K_{th,lc}$ is the stress intensity threshold for the propagation limit of long cracks and a is the crack length. The intrinsic crack size l_0 may be conveniently estimated from $\Delta K_{th,lc}$ and the fatigue limit stress of the unflawed specimen $\Delta \sigma_{lim,0}$ by setting $a = 0$, giving

$$l_0 = \frac{1}{\pi} \left(\frac{\Delta K_{th,lc}}{Y \Delta \sigma_{lim,0}} \right)^2 \quad \text{Equ. (3.7)}$$

Similarly,

$$\Delta \sigma_{th} = \frac{\Delta K_{th}}{Y \sqrt{\pi(a + l_0)}}. \quad \text{Equ. (3.8)}$$

Thus it can be seen that Equ. (3.6) represents Fig. 3.2(a) and Equ. (3.5) represents Fig. 3.2(b).

Another way of obtaining an approximation to the K-T diagram could be the use of the *R*-curve. It has been shown, e.g., in [85] that the threshold stress intensity factor range ΔK_{th} increases with increasing crack extension Δa until it reaches the constant value for long cracks. The reasons for such behaviour are various extrinsic mechanisms which occur at the wake of the crack tip and which are mainly responsible for the crack tip shielding [57]. This leads to the concept of the effective threshold stress intensity range, $\Delta K_{th,eff}$, which is corrected for crack closure or shielding effects, and therefore valid for short cracks also. Recalling Fig. 1.8 a, short crack behaviour is without shielding, which corresponds to $\Delta K_{th,eff}$, and long crack behaviour is affected by shielding, which corresponds to ΔK_{th} (where $\Delta K_{th} > \Delta K_{th,eff}$). Similar to the static case, where the resistance curve is defined as the plot of critical energy release rate (or fracture toughness or CTOD) against the crack extension, for fatigue loading the plot of threshold stress intensity factor range ΔK_{th} against the crack extension Δa is also called a resistance curve or *R*-curve, Fig. 3.4.

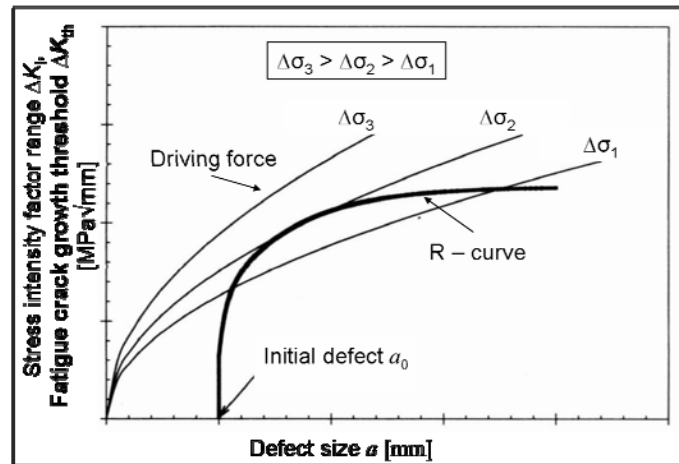


Fig. 3.4: Schematic of CDF depicting the driving force and the R-curve [85]

For a material with a certain initial defect, the *R*-curve can be used for purposes of DTD. Using the crack driving force (applied stress intensity factor range) and the resistance curve a Kitagawa diagram can be obtained.

According to [85], if it is assumed that the *R*-curve is independent of the initial crack length, the fatigue limit of small cracks can be obtained by shifting the *R*-curve in the CDF diagram to different crack sizes for obtaining the influence of the defect size on the fatigue limit. Fig. 3.4 describes schematically the fatigue resistance curve in the crack driving force diagram. It can be seen that for a particular initial defect size a_0 the threshold stress intensity factor increases with crack length. Thus the intersection of the driving force and resistance curves will lead to the critical stress range for that particular defect size. By applying this method to different initial crack sizes, a fatigue limit stress versus crack length diagram can be constructed.

It is to be noted that the *R*-curve is strongly influenced by the load ratio [85]. So, the threshold SIF range from the *R*-curve depends on the long crack threshold, the stress ratio, and the crack tip displacement,

$$\Delta K_{th,R} = f(\Delta K_{th,lc}, R, \Delta a), \quad \text{Equ. (3.9)}$$

where $\Delta a = a - a_0$. For a surface crack the driving force curve can be taken using Equ. (1.30). Thus using Equ. (3.9) and Equ. (1.30) and solving for $\Delta\sigma$, a K-T diagram is obtained.

Fig. 3.5 shows such an example, in which the K-T diagram has been obtained using the aforementioned method from an experimentally determined R-curve as published in [85]. It can be seen that El Haddad's equation approximates the behaviour quite well.

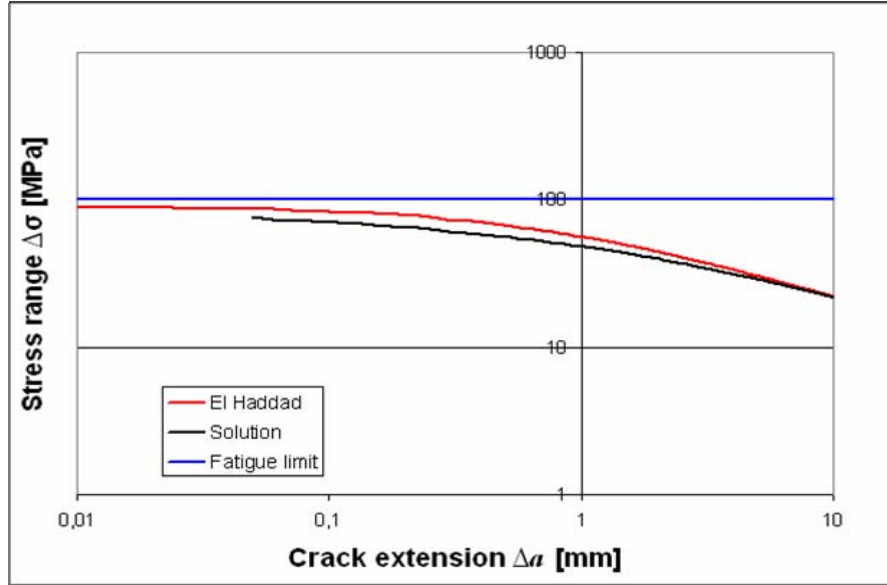


Fig. 3.5: Kitagawa diagram obtained from the R-curve (data from [85] at $R=0.1$)

A closed form solution for such a methodology has been proposed by Chapetti [86]. The fatigue limit stress is for $a \geq d$

$$\Delta\sigma_{th} = \frac{\Delta K_{dR} + (\Delta K_{th,lc} - \Delta K_{dR}) [1 - e^{-k(a-d)}]}{Y\sqrt{\pi a}} \quad \text{Equ. (3.10)}$$

and for $a < d$

$$\Delta\sigma_{th} = \Delta\sigma_0, \quad \text{Equ. (3.11)}$$

where d is the distance of the strongest microstructural barrier from the surface, K_{dR} is the microstructural threshold, a is the crack length and k is a material constant accounting for the development of the extrinsic component of ΔK_{th} .

Extending the work of Kitagawa/Takahashi and El Haddad, the stress versus crack length diagram may be used as a tool for damage tolerant design of engineering components. More recently, Gaenser et al. [68] presented the stress ratio R dependent K-T diagram using the dependence of threshold stress intensity range ΔK_{th} and the fatigue limit stress amplitude of the unflawed material σ_{a0} on the stress ratio.

Thus for a stress amplitude $\sigma_{a0} = \Delta\sigma_0/2$, and putting Equ. (3.7) into Equ. (3.3), the admissible stress amplitude for a component containing a flaw of size a is obtained as

$$\sigma_a = \frac{1}{\sqrt{\left(\frac{4\pi a}{\Delta K_{th,lc}^2}\right) + \left(\frac{1}{\sigma_{a0}^2}\right)}}. \quad \text{Equ. (3.12)}$$

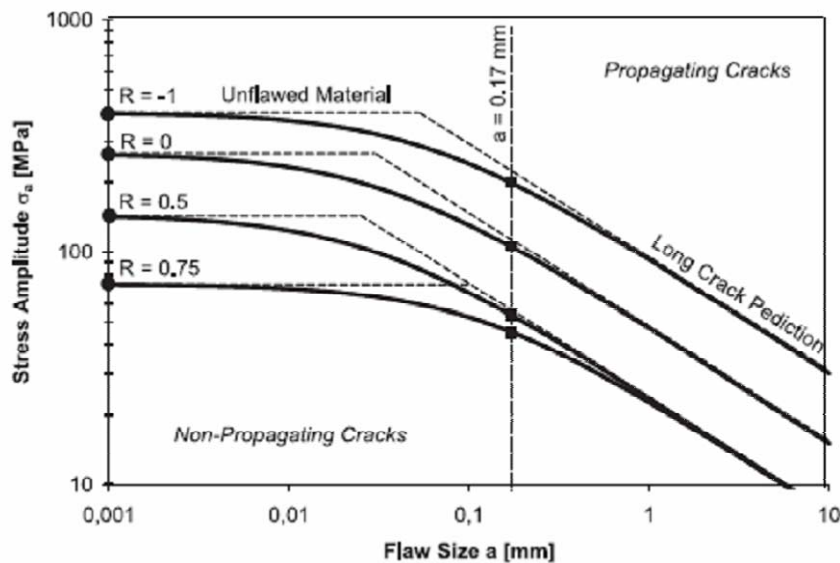


Fig. 3.6: Kitagawa diagram for S45 - dependence on R ratio [68]

Fig. 3.6 represents the K-T diagram obtained from Equ. (3.12) for a QT steel S45. Evidently, the stress ratio dependence of $\Delta K_{th,R}$ and the stress ratio dependent $\sigma_{a,R}$, are used to construct a stress ratio dependent K-T diagram.

3.3. Fatigue life curve for a material containing defects

One of the major requirements of modern engineering design is to assess the operational safety of components in the presence of flaws. Conventional design methods assuming a defect-free material are still the most widely used practical tools in industry. On the other hand, a wide variety of methods from fracture mechanics exists for the assessment of flawed components. With the introduction of the intrinsic crack length – i.e., the length parameter l_0 in El Haddad's approximation to the K-T diagram –, it has become possible to merge the two approaches. It will be demonstrated subsequently that crack growth results can be utilized to obtain S/N curves by integrating the crack growth law with respect to initial and final allowable crack size. In the case of a cracked component, the observed crack length acts as initial crack size; in the case of an unflawed material, the intrinsic crack length l_0 from El Haddad's model serves the same purpose. In other words, the K-T diagram ensures a unified treatment of defect-free and flawed components.

Furthermore, broadly speaking, the first two branches of the FCG curve (threshold and lower proportional part) correspond roughly to the biggest proportions of lifetime spent in the endurance and HCF regions of the S/N curve.

The situation is somewhat different for the region III of the FCG curve, which corresponds to incipient instability. As the LFM approach is not valid for large scale yielding, it is advisable to use the integration of the crack growth law for LCF, where plasticity plays the dominant role. Instead, the cyclic stress-strain curve may serve as a tool for connecting the e-N curve to the conventional S-N curve.

Fig. 3.7 summarizes these links between the various fatigue life prediction methodologies. The conventional S/N curve occupies the centre of the figure as the most widely used design tool in practice. The cyclic stress-strain curve forms the link to the e/N curve, whereas the Kitagawa diagram (and its possible generalization to finite lifetime as proposed by Ciavarella and Monno [70]) helps to introduce the notion of a (possibly intrinsic) crack length, providing the basis for applying the fatigue crack growth curve to lifetime estimation.

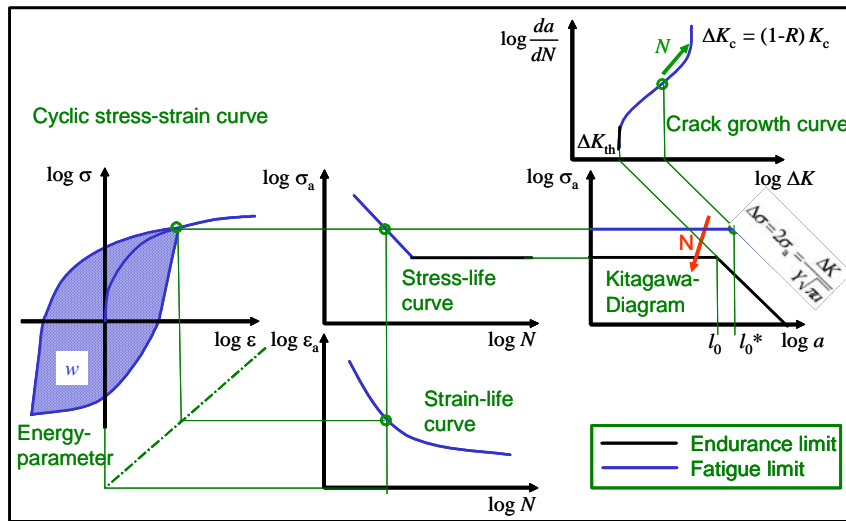


Fig. 3.7: Comparison of methodologies for defect free material

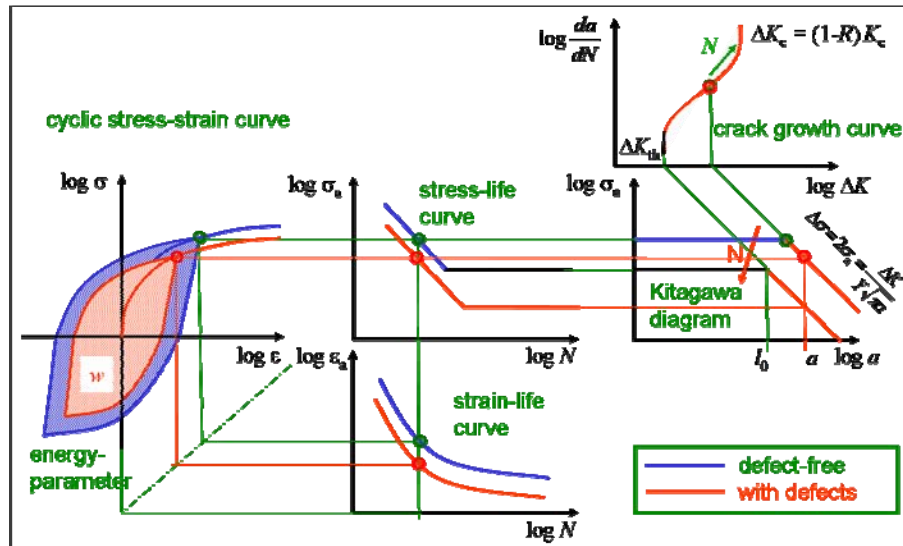


Fig. 3.8: Comparison of methodologies for material with defects

With reference to the figure above, it can be seen that the two asymptotes in the K-T diagram – represent the fatigue crack growth threshold ΔK_{th} for a damaged material and the endurance limit for a defect-free material, respectively. Also in this sense, El Haddad’s intrinsic crack length l_0 described in Equ. (3.7) marks the transition between the un-cracked and cracked material states. The K-T diagram is normally drawn for the endurance limit, i.e., for infinite lifetime, which corresponds to the crack growth threshold SIF range in the FCG curve. Similarly for the finite life the intrinsic crack size l_0^* will be greater than the infinite life intrinsic crack size l_0 (cf. Fig. 3.7). If the loading exceeds the crack growth threshold, a crack starts growing until it reaches instability, corresponding to region III in the FCG curve or, at the point of final rupture, corresponding to the static fracture toughness K_{Ic} of the material. The equivalent length at final fracture can thus be computed from

$$a_f = \frac{1}{\pi} \left(\frac{K_{Ic}}{\sigma_{max}} \right)^2 \quad \text{Equ. (3.13)}$$

where σ_{max} is the maximum stress at final rupture.

As far as LCF is concerned, the link between the strain-life and stress-life curves can be visualized through the cyclic stress-strain curve.

This will in turn provide a closer approximation of the upper part of the stress-life curve owing to the fact that the strain-life curve is recorded in conditions when the loadings are mostly inelastic. Using this and based on the fact that the yield strength of a material is the parameter which separates the elastic and plastic portions, one can give an estimate for the low cycle fatigue regime of the stress-life curve. – Finally, if the material behaviour is known in such detail that the hysteresis loops may be evaluated, then also an energy approach based on the total strain energy density (see Section 1.1) is well suited for obtaining the fatigue damage per cycle [71].

Coming to the question for obtaining the fatigue life time of a material containing a particular defect, Fig. 3.8 outlines the procedure analogously to the unflawed case in Fig. 3.7. For a certain crack size a greater than the length parameter l_0 as defined in Equ. (3.7), the endurance limit will be decreased, thereby shifting the stress-life curve downwards. Alternatively, for the same loading, the presence of a crack size larger than l_0 will result in a lower number of cycles, shifting the stress-life curve to the left.

3.4. Prediction of the HCF and endurance regimes

For obtaining the fatigue life of a cracked specimen, the easiest way is to integrate the simplest form of FCG law, i.e., the Paris equation Equ. (1.29). For initial and final crack sizes a_i and a_f this becomes

$$N = \int_{a_i}^{a_f} \frac{1}{C(\Delta K)^m} da. \quad \text{Equ. (3.14)}$$

Consequently, substituting the value of ΔK (such as from Equ. (1.30)), and assuming no geometrical influences, $Y = 1$, the above equation gives

$$a_i^{2-(m/2)} - a_f^{2-(m/2)} = \left(\frac{m-2}{2} \right) C \pi^{m/2} \Delta \sigma^m N. \quad \text{Equ. (3.15)}$$

Obviously, the resulting equation is a sort of stress-life curve. However, owing to the fact that Paris equation characterizes the crack growth curve in the regime II only, possible deviations in the crack threshold regime I and the rupture regime III will result in a stress-life curve that is mainly valid in the high cycle fatigue regime (cf. Fig. 1.7 and Fig. 1.2). The slope of such a stress-life curve can be obtained using

$$\frac{d(\log \sigma)}{d(\log N)} = -\frac{1}{2m\sigma} \frac{2 \left(a_i^{1-\frac{m}{2}} - a_f^{1-\frac{m}{2}} \right)}{\pi^{\frac{m}{2}} N(m-2)C}. \quad \text{Equ. (3.16)}$$

Another possibility to obtain the crack growth description for the threshold and Paris regime is to use Donahue's function [72]. Accordingly,

$$\frac{da}{dN} = C \left[\Delta \sigma \sqrt{\pi a} - \Delta K_{th} \right]^m. \quad \text{Equ. (3.17)}$$

The closed form solution can be obtained by integrating the above equation,

$$N = \frac{2}{C\pi\Delta\sigma^2} \left[\frac{(\Delta K - \Delta K_{th})^{2-m}}{2-m} + \frac{\Delta K_{th}(\Delta K - \Delta K_{th})^{1-m}}{1-m} \right]_{a_i}^{a_f}. \quad \text{Equ. (3.18)}$$

In the literature there are a lot of equations for describing the fatigue crack growth behaviour (cf., e.g., [5] [46]). In fact, none of these formulas has a physical background; instead, they are based on trends observed from experimental investigations. One model for a fit of the complete fatigue crack growth behaviour is Kohout's Equ. (1.34) (Section 1.2).

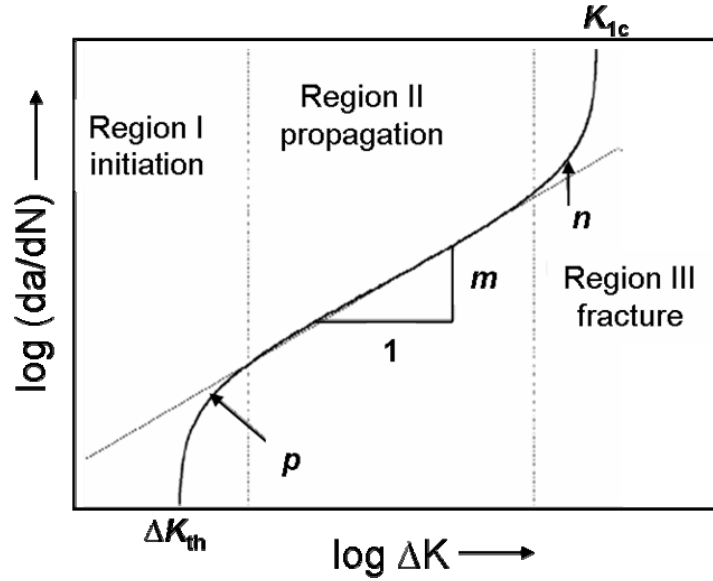


Fig. 3.9: Schematically drawn fatigue crack growth curve with associated regression parameters for **Equ. (1.34)**

In this function, the parameter p defines the curvature between regions I and II, and n defines the curvature between regions II and III (cf. Fig. 3.9). The function is easily adaptable to crack initiation and growth or to crack growth and final fracture, thereby providing a versatile fit to experimental data.

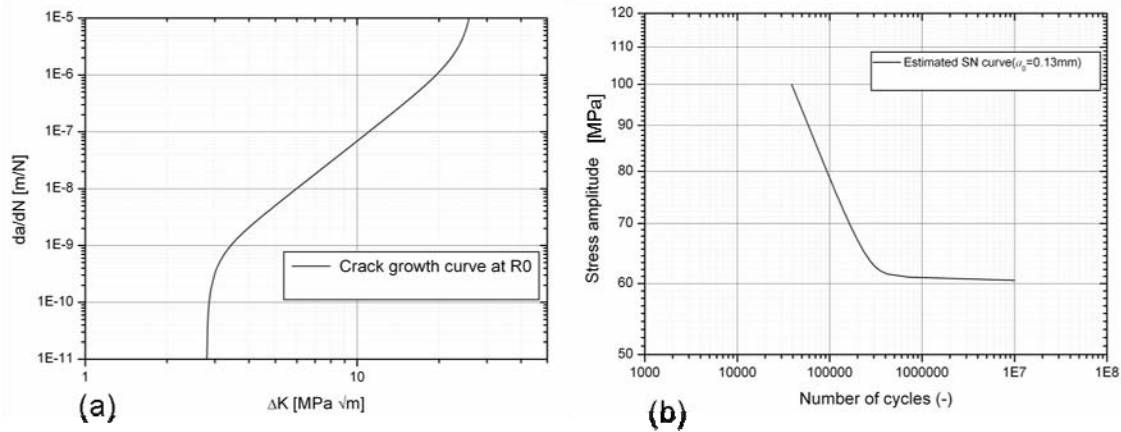


Fig. 3.10: (a) Fatigue crack growth curve (b) Corresponding S-N curve at a stress ratio $R = 0$

Another advantage of using this equation is that, apart from characterizing different stages of the crack growth behaviour, it also incorporates the influence of the stress ratio within the same function. Similar to the previously described method for Paris equation, it also needs to be integrated to obtain a stress based fatigue life curve,

$$N = \int_{a_i}^{a_f} \frac{1}{CK_c^n \left(\frac{\Delta K}{(1-R)^\gamma} \right)^{m-p} \left[\frac{\{(\Delta K(1-R)^{-\gamma})^p\} - \Delta K_{th0}}{\{K_c^n - (\Delta K(1-R)^{-1})^n\}} \right]} da, \quad \text{Equ. (3.19)}$$

where ΔK is obtained from Equ. (1.30). However, Equ. (3.19) is too complex for a closed form solution. In [73], a method has been proposed for integrating Equ. (3.19) numerically. Assuming no crack growth occurs below the threshold ΔK_{th} , the fatigue endurance limit for an un-cracked specimen can be obtained using the intrinsic length l_0 from El Haddad's Equ. (3.7). Alternatively, different initial crack sizes can be used to obtain the fatigue life time within the context of damage tolerant design. For each load level the lifetime is calculated using the applied stress intensity factor for a particular initial defect size by integrating up to the final crack size obtained from the fracture

toughness K_{Ic} using Equ. (3.13). If the fracture toughness is not available, it is approximated from the fit to fatigue crack growth data (K_c in Equ. (3.19)). In Fig. 3.10, an S-N curve obtained by this method is shown.

3.5. Prediction of the LCF regime

When a structure is subjected to heavy cyclic loadings, with stresses lying above the yield stress in many cases, thereby inducing irreversible strains on a larger scale, low cycle fatigue occurs. In this case the number of cycles to failure is relatively small, depending on the type of application [74]:

- 10 – 100 for aerospace applications
- 100 – 1000 for nuclear or thermal power plants (power-up/shutdown cycles)
- 1000 – 10000 for aircraft (passenger cell pressurization cycles, etc.)
- $10^4 < N < 10^5$ assessment by LCF or HCF methods possible, depending upon the case and the degree of accuracy needed

The boundary between the low cycle and high cycle fatigue regions cannot be exactly defined by a specific number of cycles. However, the more relevant difference between the two conditions is that the low cycle fatigue is associated with macroscopic plastic deformations in each cycle. Conversely, high cycle fatigue is more related to elastic behaviour on a macroscale [5].

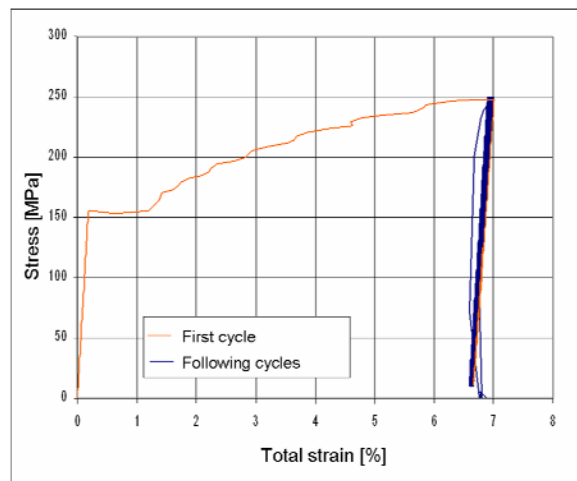


Fig. 3.11: Stress controlled LCF test for aluminium alloy 5083 H111 at a stress ratio $R = 0.04$

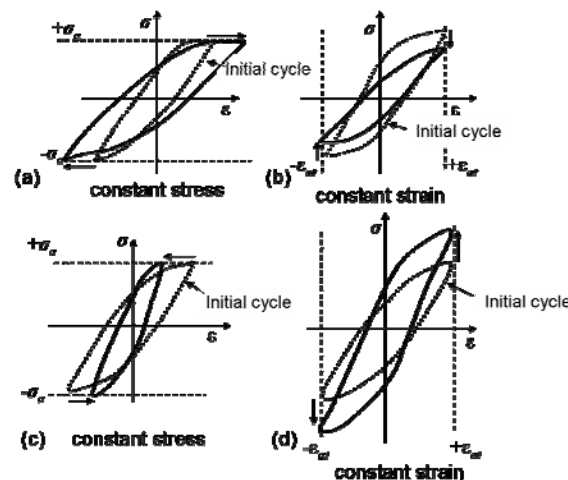


Fig. 3.12: Schematic cyclic response of materials (a),(b) cyclic strain softening and (c),(d) cyclic strain hardening [75]

So, generally, a strain-life approach is used for obtaining the fatigue life of a material under high plastic loadings. It must be noted that, in principle, also for the strain-life approach both stress-controlled and strain-controlled testing methods can be applied. However, as a stress-controlled (constant load amplitude) testing will lead to marked plastic deformations in the first cycles followed by much smaller strain amplitudes in subsequent cycles [5] (see also Fig. 3.11), mostly constant strain amplitude testing is applied in practice. The question under which circumstances strain-controlled test data may be displayed in the context of a constant-stress diagram such as the S/N curve, is closely related to the cyclic hardening behaviour of the material and will be discussed in more detail below.

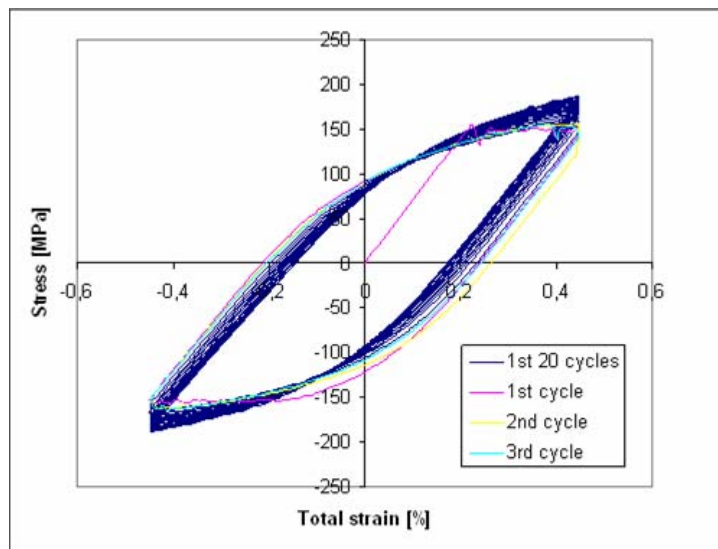


Fig. 3.13: Stress-strain loops during constant- ϵ_a cycles of low cycle fatigue showing cyclic strain hardening of material (aluminium 5083 H111; $\epsilon_a = 0,45$; $R = -1$)

In Fig. 3.12, the cyclic response has been depicted schematically under constant stress and constant strain amplitude, respectively. After the initial cycle, the stress amplitude under strain controlled fatigue testing can vary in the following cycles. For cyclic strain hardening, constant strain cycles lead to increasing stress amplitudes. Conversely, decreasing stress amplitudes are obtained in the case of cyclic strain softening. The stress-strain loops for the aluminium alloy under consideration in the present study, aluminium 5083 H111, are shown in Fig. 3.13; the peak stresses in each cycle are depicted in Fig. 3.14 for a constant strain amplitude of 0.35%. From the figures it becomes clear that this material experiences cyclic strain hardening.

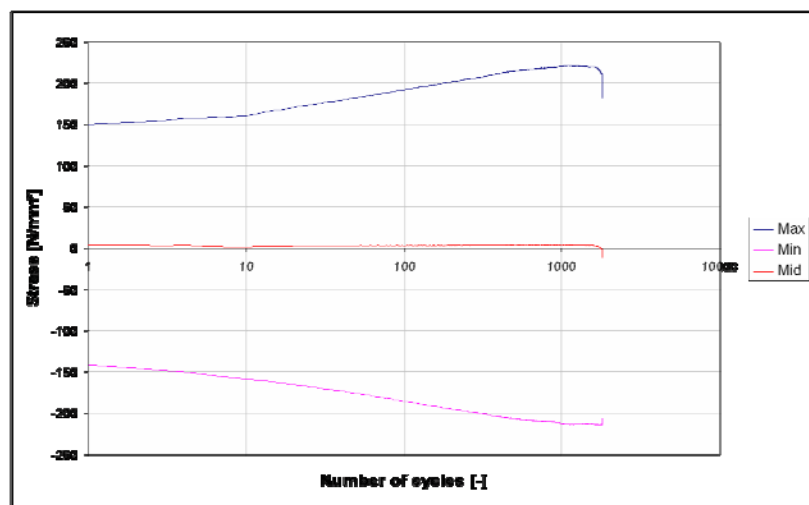


Fig. 3.14: Strain controlled LCF test: Maximum and minimum stress values plotted against the number of cycles. (aluminium 5083 H111)

Generally, both cyclic strain hardening and cyclic strain softening stabilize to a constant level after a number of cycles, cf. Fig. 3.15 a. The number of cycles after which the cyclic loop become stabilize depends upon the material, its manufacturing process and heat treatment [5].

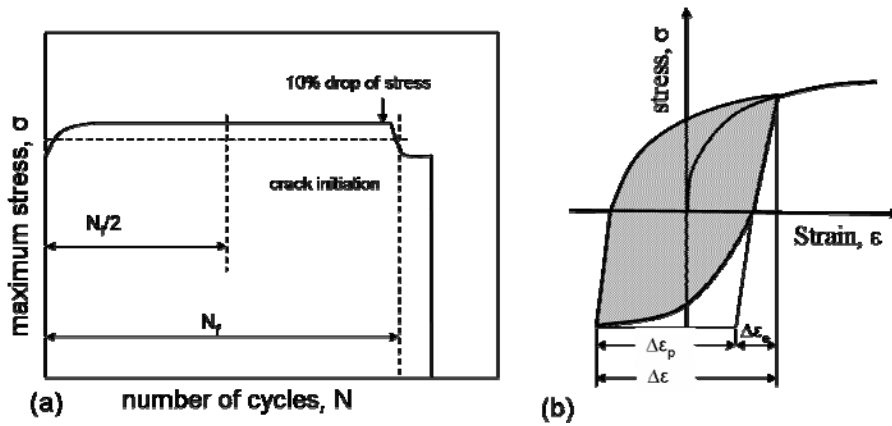


Fig. 3.15: Definition of maximum stress at half number of cycles, (cf. [78]) (b) stabilized hysteresis loop at $N_f/2$

With reference to the schematic representation in Fig. 3.8, it can be seen that the possibility of obtaining results of the strain life approach can be attained using the cyclic stress strain curve. As briefly described earlier (see also [77]), the approach is to follow the failure or maximum stress of the hysteresis loop at different strain amplitudes.

Fig. 3.16 describes schematically the method. The failure stress or maximum stress according to the criterion of the Standard [101] is observed for stabilized hysteresis loops at half life for different strain amplitudes. The corresponding maximum stress values are then incorporated within the stress based fatigue life curve, giving a representation for the low cycle fatigue regime. Such a cyclic stress strain curve can be approximated using a power law fit such as the Ramberg-Osgood relation

$$\frac{\Delta\epsilon}{2} = \frac{\Delta\sigma}{2E} + \left(\frac{\Delta\sigma}{2K'}\right)^{1/n'} \quad \text{Equ. (3.20)}$$

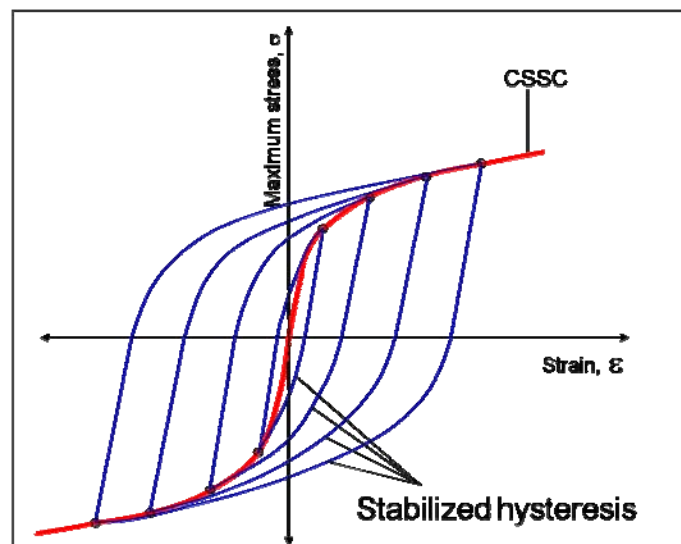


Fig. 3.16: Schematic representation of stable hysteresis loops at half-life for different strain amplitudes

As mentioned above, it may be questioned whether such maximum stress values may be incorporated in a (constant-) stress-life curve. The fact that in case of cyclic hardening or softening the stress values may increase or decrease should not induce a major error because the maximum stress value taken at half number of cycles will represent the stabilized regime covering the major part of the test.

Following Fig. 3.17, where the hardening response for two different strain amplitudes has been shown, it can be seen that the total life for a particular strain amplitudes can be split into three regimes:

- Initial shakedown regime, N_a
- Stabilized regime, N_b
- Final damage regime, N_c

Thus the error associated with using only the stabilized values can be

$$e_N = \frac{N_{total} - N_b}{N_{total}} \quad \text{Equ. (3.21)}$$

where N_b is the life of stabilized regime over which the stress value remains nearly constant, and $N_{total} = N_a + N_b + N_c$. Taking these considerations into account, a possible error based on the generally observed minimum and maximum number of cycles for these regimes (see Fig. 3.17), could be between 2-10%, with the error becoming lower for decreasing strains and increasing number of cycles (i.e., as the HCF regime is approached).

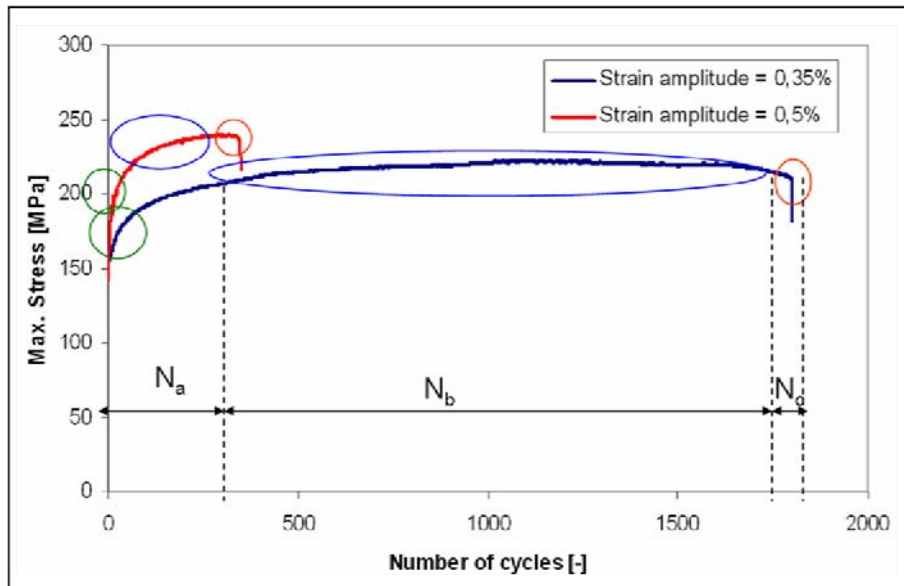


Fig. 3.17: Hardening curves for aluminium 5083 H111 at two different strain amplitudes

Using the above knowledge and based on the experimental results (see Chapter 4 and Section 5.1.3), a method will be proposed now for estimating the low cycle fatigue lifetime within the stress-based diagram. In what follows, the tensile properties of the material will be utilized to obtain such a first prediction.

Commonly, the flow stress – i.e., the average value of yield and ultimate tensile stresses – is used to obtain a collapse load [47].

$$\sigma_f = \frac{\sigma_y + \sigma_u}{2} \quad \text{Equ. (3.22)}$$

The same is used in the present study for the LCF estimate of an undamaged material, Fig. 3.18. The flow stress corresponds to a fatigue life of one cycle. Similarly, the yield strength corresponds to the limit of validity of the HCF curve (which results in 2×10^4 cycles in this case). The task remains how to approximate the material behaviour between these limits of the LCF regime.

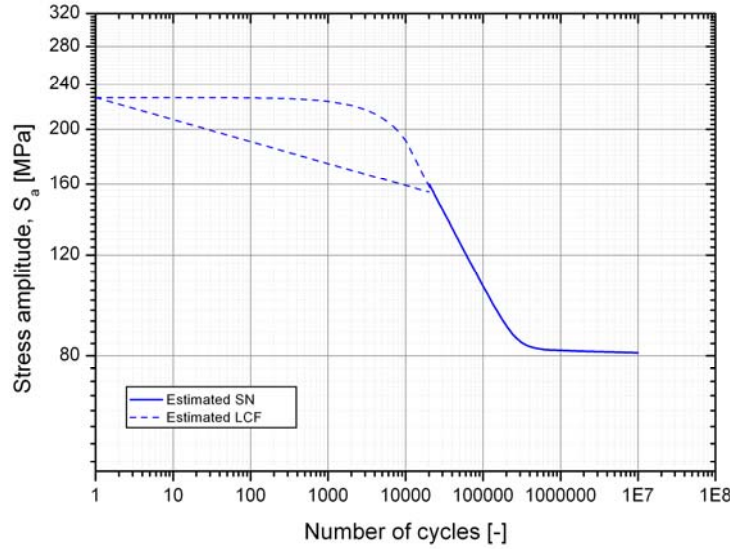


Fig. 3.18: LCF estimation procedure from static properties and S-N curve from crack growth properties.

One way is to use a linear interpolation between the flow stress (static) and yield strength (HCF limit) of the material, and between one load cycle (static) and the number of cycles at the LCF-HCF boundary. This leads to the following equation:

$$\sigma_a = \sigma_{a1} + \left[\frac{(N - N_1)(\sigma_{a2} - \sigma_{a1})}{(N_2 - N_1)} \right]^\alpha, \quad \text{Equ. (3.23)}$$

where σ_{a1} and σ_{a2} are the stress amplitudes at N_1 and N_2 number of cycles respectively corresponding to flow stress and yield stress, and $\alpha = 1$ for linear interpolation.

On the other hand, a straight line connecting these two points, i.e., the flow stress and yield stress, in the log-log S-N diagram gives another approximation for the LCF regime. In Fig. 3.18, both approximations have been presented. The experimental validation (see Chapter 5) will show that for the current material the latter estimate is a lower bound to the experimental data. A conservative analytical approximation for the LCF regime of the S-N curve is therefore

$$\sigma_a = \sigma_f (N)^{m'}, \quad \text{Equ. (3.24)}$$

where σ_f is the flow stress and m' is given by

$$m' = -\frac{\log(q)}{\log(1/c)}. \quad \text{Equ. (3.25)}$$

In Equ. (3.25), q is the ratio of yield strength to flow stress (σ_y/σ_f) and c is the lifetime of the LCF regime, which can be taken as $10^3 - 10^4$ cycles for a stress ratio $R = -1$.

4. Experimental Investigation

4.1. Material

Aluminium 5083 H111⁸ alloy has been used for the current study. Tab. 4.1 shows the chemical composition of the alloy [76]. 5083 is a non heat treatable alloy which is resistant to corrosion and can be welded. Material was supplied in a thin sheet form of 1 mm thickness. The specimens for all of the tests were obtained by high pressure water-jet cutting. Later on the surfaces and edges were polished manually to remove any defects from the testing areas.

Si	Fe	Cu	Mn	Mg	Traces	Al
0.152	0.329	0.034	0.6	4.2	0.1	balance

Tab. 4.1: Chemical composition of 5083 H111

4.1.1. Tensile tests

Tensile tests were performed on a 10 kN hydro-pulsating test rig Fig. 4.1. The specimens were sized according to ASTM E8-03 testing standards and tests were performed at a test rate of 0.005 mm/sec. All the tests were displacement controlled and the applied load were controlled by the load cells, whereas the corresponding strains were measured by an extensometer.

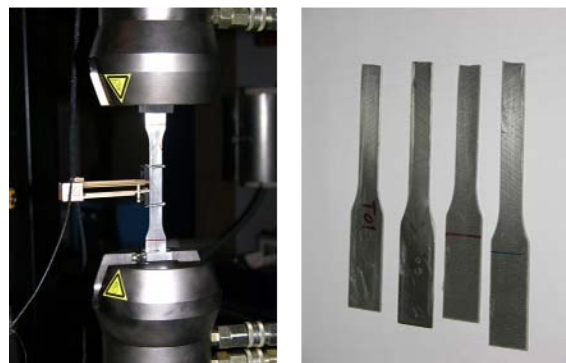


Fig. 4.1: Tensile tests

The tensile tests show a pronounced yield point elongation behaviour. One can see the Lüders bands even with a naked eye which are distributed along the length of the specimen at an angle of approximately 50° to the loading axis (Fig. 4.2).



Fig. 4.2: Lüders bands

Fig. 4.3 shows the monotonic stress-strain data of the alloy. The yield strength and ultimate tensile strength of the material are 155 MPa and 290 MPa, respectively. The hardness of the material is approximately 75 (HV) (see section 4.1.2) [80]. Other tensile data are given in Tab. 4.2.

⁸ H111 applies to alloys which are strain-hardened less than the amount required for a controlled H11 temper, whereas H11 designates half of one quarter hardened [79].

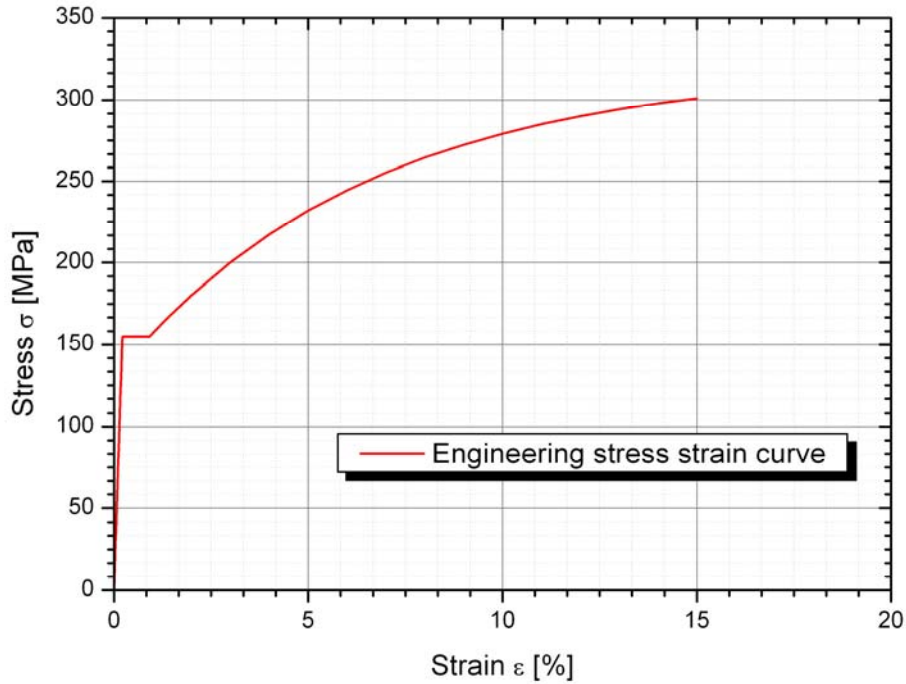


Fig. 4.3: Monotonic stress-strain data

Yield stress, R_e (MPa)	Ultimate tensile stress, R_m (MPa)	Young's modulus, E (MPa)	Area reduction (%)	Elongation at fracture (%)	Yield point elongation (%)
155	300	71000	8.85	15	1.1

Tab. 4.2: Tensile data obtained from tests

4.1.2. Hardness measurements

As a qualitative assessment of the resistance of the material against plastic deformation, generally the hardness of the material is measured. Further, for defect tolerance consideration of welded structures it is important to see the effect of hardness values in different welding zones. This can be achieved using different measurement scales. For the current case Vickers hardness test, has been used.

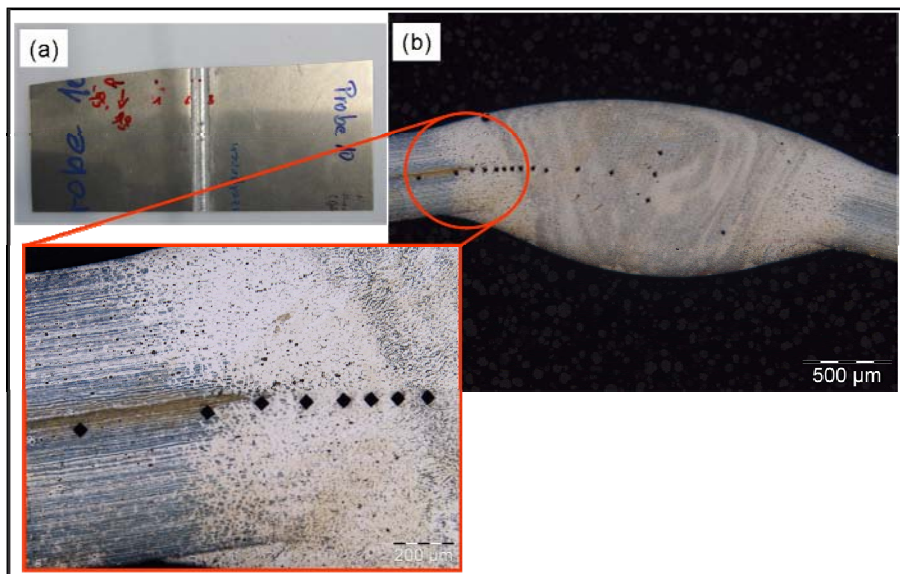


Fig. 4.4: Hardness measurement: (a) Welded plate (b) Indentation in the weld and heat affected zones

The surface was subjected to a standard force for a particular length of time by means of a square-based pyramid shaped diamond. Fig. 4.4 describes the measured surface at different zones. The specimens were welded using a TIG process with filler material (Fig. 4.4 a). Such a method has the advantage of obtaining a superior quality weld with precise control of welding variables. The hardness indentations can be seen in the weld and the heat affected zones (Fig. 4.4 b).

The following values have been obtained for the different zones:

- Weld seam and plate: ~ 75 HV (0.1 kp)
- Heat affected zone: ~76-85 HV (0.1 kp)

4.2. Fatigue tests (defect free material)

4.2.1. HCF tests

In order to assess the response of the material under cyclic loading, fatigue tests were performed. A flat specimen of thickness 1 mm was used. Fig. 4.5 shows the geometry of the test specimen. The geometrical dimensions of the specimen give a notch factor $K_t = 1.04$, i.e., a virtually un-notched specimen with negligible stress concentration and stress gradient.

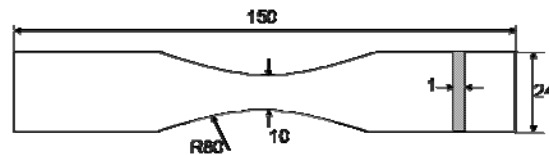


Fig. 4.5: HCF testing specimen

Fatigue tests were done at the following load ratios

- at a pulsating amplitude loading $R = 0$
- at a tension-tension loading with $R = 0.2$.
- at $R = 0.5$ (a few data points were obtained to further validate the influence of the mean stress effect)

All the tests were performed at room temperature and at a frequency of 70 Hz in an electro-magnetic resonance rig. Due to smaller thickness and higher test frequency, HCF fatigue tests were not possible at $R = -1$.

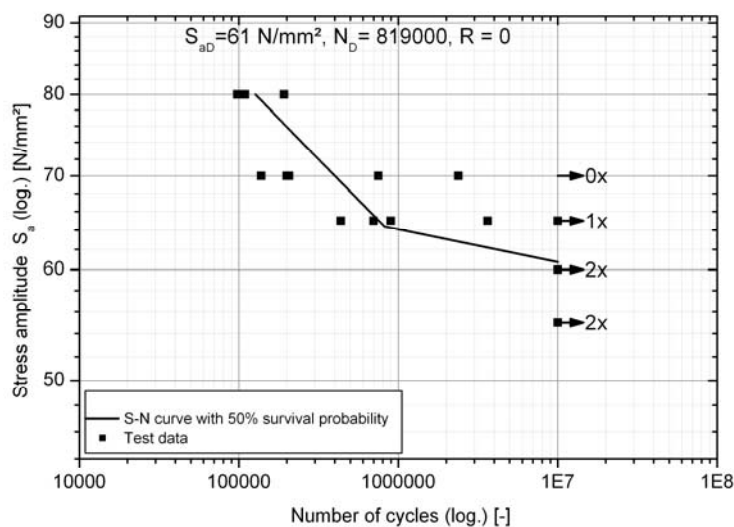


Fig. 4.6: S-N tests at a stress ratio $R = 0$

The test data are shown in Fig. 4.6 and Fig. 4.7 in terms of stress amplitude σ_a against the number of cycles to failure N . Due to the reason that many aluminium alloys do not show a well defined endurance limit, the test were continued until 10^7 number of cycles. This was also supported by the test results for the current case. The S-N with 50% survival probability was obtained using an $\arcsin\sqrt{P}$ transformation method. It can be seen that the alloy is giving a two-slope behaviour and thus the S-N curve can be approximated such that at the intersection point of the two lines Equ. (1.6) holds.

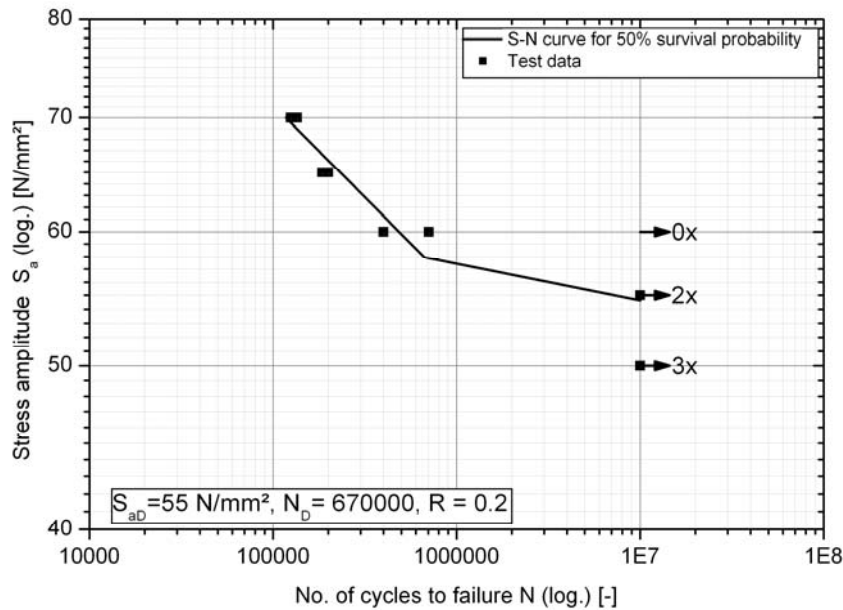


Fig. 4.7: S-N tests at a stress ratio $R = 0.2$

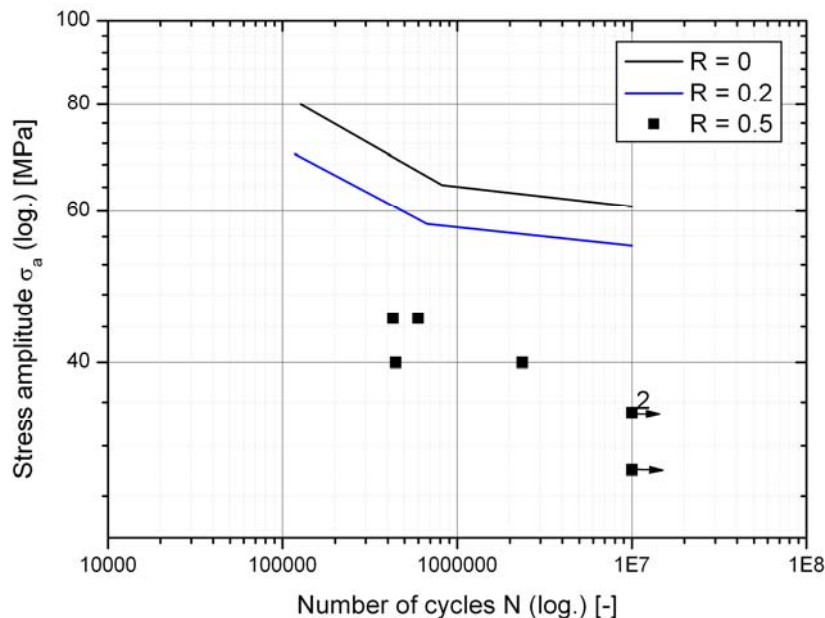


Fig. 4.8: S-N curves and data ($R = 0$, $R = 0.2$ and $R = 0.5$)

Fig. 4.8 and Tab. 4.3 combines all the test data obtained from testing at stress ratios of 0, 0.2 and 0.5. Thus a fatigue limit of 61 MPa (at 10^7 cycles) for pulsating loading ($R = 0$) has been obtained. The mean stress has a greater influence on the material and both the slope and the fatigue limit decrease with increasing stress ratio. On the other hand the trend for the slopes in LCF-HCF and HCF-endurance regimes seems to be similar for all loading ratios.

Stress ratio R	Fatigue limit σ_{aD} [MPa]	$k1$	$k2$	N_D
0	61	8.6	42.9	819000
0.2	55	9.2	46	670000
0.5	35	-	-	-

Tab. 4.3: Fatigue data for 5083 aluminium-magnesium alloy

4.2.2. LCF tests

For obtaining the behaviour of the material under high cyclic forces, where macroscopic plastic deformation occurs in each cycle, LCF data is necessary. LCF tests can be done stress or strain controlled. However, since constant stress amplitude loading will lead to a higher plastic deformation during the first cycle followed by much smaller strain amplitudes in subsequent cycles (e.g. see Fig. 3.11), tests were performed strain controlled. Furthermore, for a basic understanding of the material's cyclic behaviour, tests were carried out at a strain ratio $R = -1$.



Fig. 4.9: Testing setup for strain controlled LCF experiments

LCF experiments were carried out on a hydro-pulsating test rig at room temperature. As the material was in a thin sheet form, special anti-buckling measures were taken. This was achieved by placing support plates around the test specimens. The specimens were manufactured according to the AECMA Standard [101]. The strains were measured using a commercial extensometer (Fig. 4.9).

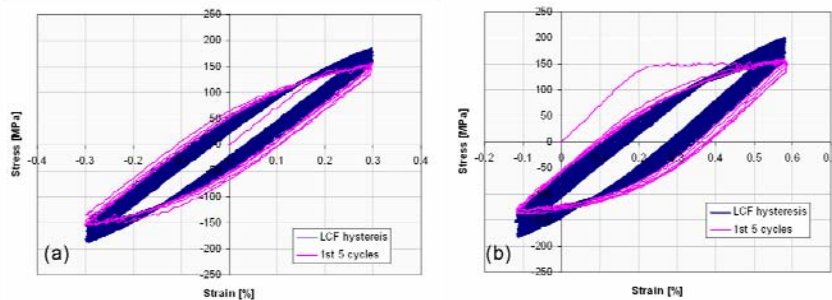


Fig. 4.10: LCF hysteresis loops for (a) $R = -1$ and $\epsilon_{t,a} = 0.30\%$ and (b) $R = -0.2$ and $\epsilon_{t,a} = 0.35\%$

The hysteresis loops for fully and partially reversed strain amplitude loading $R = -1$, $R = -0.2$ are shown in Fig. 4.10. It can be seen that with increasing number of cycles, the stress amplitude increases i.e., cyclic strain hardening behaviour is observed.

The low cycle fatigue data for $R = -1$ are shown in Fig. 4.11 in terms of total strain amplitude $\epsilon_{a,t}$ against number of cycles to failure. The tests were conducted over different constant (total) strain amplitudes ranging from 0.22% to 0.65%. The tests were continued until the development of a crack

or until a decrease of 10% in the stress value in the maximum stress versus number of cycles curve. The total strains, split into elastic ε_{el} and plastic ε_{pl} components, are also plotted. The curves for the elastic and plastic strains are approximated using the power law equations by Basquin and Coffin-Manson, respectively.

$$\varepsilon_{a,e} = \frac{\sigma'_f}{E} (2N_f)^b \quad \text{Equ. (4.1)}$$

$$\varepsilon_{a,p} = \varepsilon'_f (2N_f)^c \quad \text{Equ. (4.2)}$$

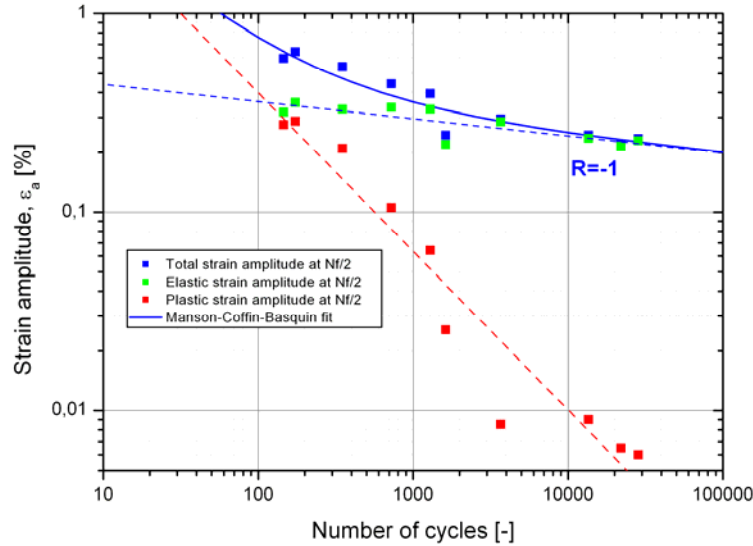


Fig. 4.11: Strain controlled LCF tests ($R = -1$)

Here, b and c denote the slopes of the elastic and plastic portions, respectively, and the parameters σ'_f and ε'_f are called the fatigue strength and ductility coefficients. It can be seen from Fig. 4.11 that the strain life of the material for a total strain amplitude of 0.22% can last up to 10^4 cycles.

The coefficients and exponents in the Coffin-Manson-Basquin relation depends on the material and temperature. There exist many approximations for obtaining parameters (σ'_f , ε'_f , b , c) of strain life curve (see e.g., [81]). For comparison purpose one of the approximations is used here. In [82] a generalized form of the above relation has been given in the following form called 'universal slopes' [1]:

$$\frac{\Delta\varepsilon}{2} = 0.623 \left(\frac{S_u}{E} \right)^{0.832} (2N_f)^{-0.09} + 0.0196 (\varepsilon_f)^{0.155} \left(\frac{S_u}{E} \right)^{-0.53} (2N_f)^{-0.56} \quad \text{Equ. (4.3)}$$

where S_u is the ultimate static fracture stress, E the Young's modulus, ε_f is the fracture strain are obtained from monotonic tension test and $2N_f$ is the number of cycles to failure. Here it is assumed that the values of exponents remain same for all metals and S_u , E and ε_f control the fatigue behaviour. Values of the parameters obtained from experimental data are compared with values from Equ. (4.3) in Tab. 4.4. It can be seen from Fig. 4.12 that the method over estimates the life compared to the Coffin-Manson-Basquin relation with parameters obtained form experimental data (cf. Equ. (4.3))

Coefficients	From experimental data ($R = -1$)	From Equ. (4.3)
σ'_f [MPa]	365	468
b [-]	-0.086	-0.09
ε'_f [%]	15.8	26.5
c [-]	-0.79	-0.56

Tab. 4.4: Comparison of Coffin-Manson-Basquin coefficients with 'universal slopes' (Equ. (4.3))

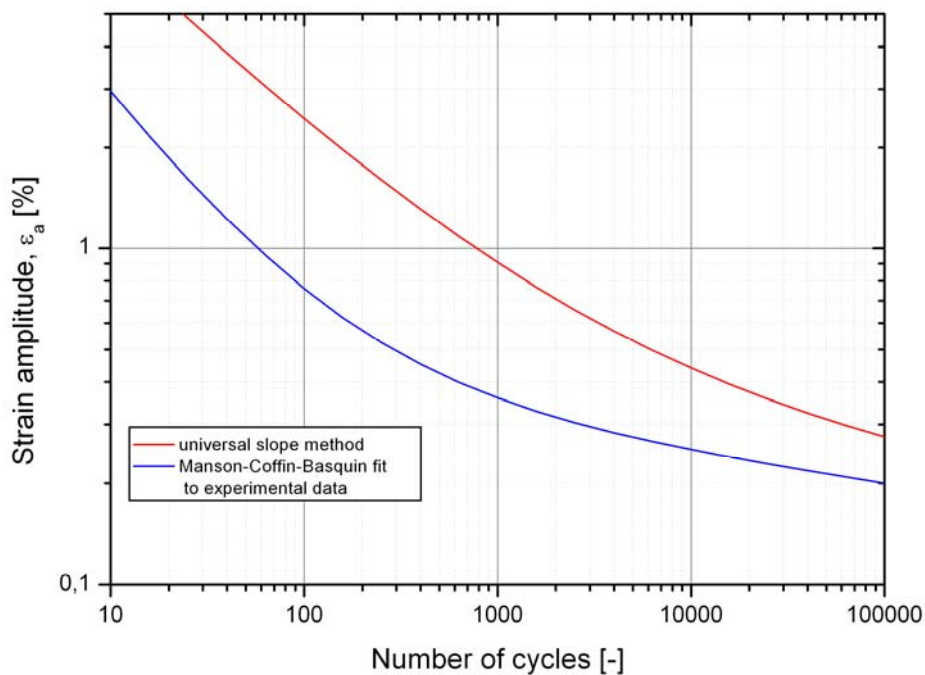


Fig. 4.12: Comparison of Coffin-Manson-Basquin coefficients with 'universal slopes' (Equ. (4.3))

4.3. Fatigue tests (with defect)

4.3.1. HCF tests

Various techniques can be used to obtain an artificial crack. However, an important factor is the sharpness of the resulting crack. In the present study, a crack, approximately equal to 0.14 mm was obtained by means of a sharp knife⁹. The initial depth of the crack was verified *a posteriori* by examining the fracture surface of the specimen under the light microscope. Experimental results were included only from those specimens whose crack depth was within the required range. Fig. 4.13 shows, a pre crack produced by this method.



Fig. 4.13: Artificial crack generation

Two types of crack geometries have been considered – type1: a surface crack of ~3 mm length and type2: a full length surface crack. The depth of the pre crack was around 0.12~0.16 mm in both cases. Similar to fatigue tests of specimens without defect, tests of specimens containing defects were also carried out in an electro-magnetic resonance machine. HCF experiments were conducted under

⁹ It is to be pointed out that similar to fatigue crack growth tests as described in section 4.4, the pre-crack may be allowed to grow cyclically (preferably in compression) before it is loaded for the desired purpose in order to obtain a sharp fatigue crack, however; this was not possible in this case due to smaller thickness of the specimen.

constant amplitude pulsating loading ($R = 0$). The tests were done at room temperature under load control at a frequency of 70 Hz.

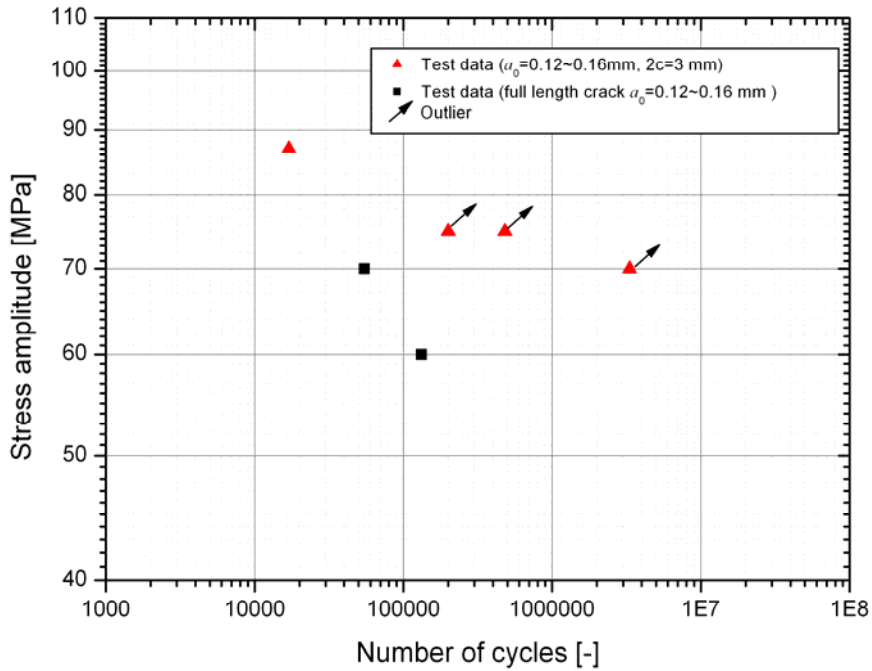


Fig. 4.14: Stress life data for specimen with defect at load ratio, $R = 0$

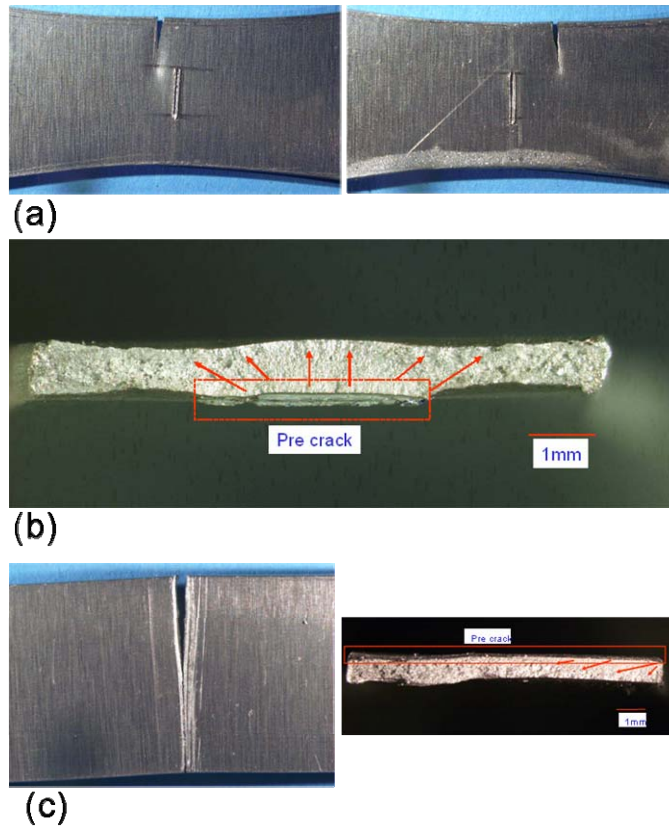


Fig. 4.15: Fatigue tests for specimens with pre defect: (a) crack type 1 (b) fractured surface of crack type1 tested under high loadings (c) fractured surface of crack type 2

The fatigue test results for specimens with both types of defects are shown in Fig. 4.14. For a defect of length $2c = 3$ mm, mostly the crack did not initiate from the defect (Fig. 4.15 a). However, the numbers of cycles to failure in these cases were within the scatter band of the defect-free specimens. This indicates that that this type of defect does not affect the life time of the specimens.

On the other hand when a specimen was tested at a higher load level, failure initiated at the initial defect (pre-crack) with a lower number of cycles to failure. In Fig. 4.15 b, the broken surface of such a specimen is shown. The specimen was tested at stress amplitude of 86.5 MPa. It is to be noted that for a stress ratio $R = 0$, this level is already in the plastic region of the material (material's yield strength $\sigma_y = 155$ MPa).

The HCF tests were also performed on specimens with a pre-crack of initial depth and length $2c$ as width of the specimen. In this case the crack started to grow from the initial defect, giving a lower number of cycles to failure

4.3.2. LCF tests

The low cycle fatigue tests for a material containing a pre crack were performed at different constant strain amplitudes. The test results were obtained on specimens containing a surface crack of length $2c = 3$ mm and depth $a_0 \approx 0.14$ mm. The material showed a similar hardening behaviour as was in case of a defect free material. However the specimens failed at a relatively lower number of cycles.

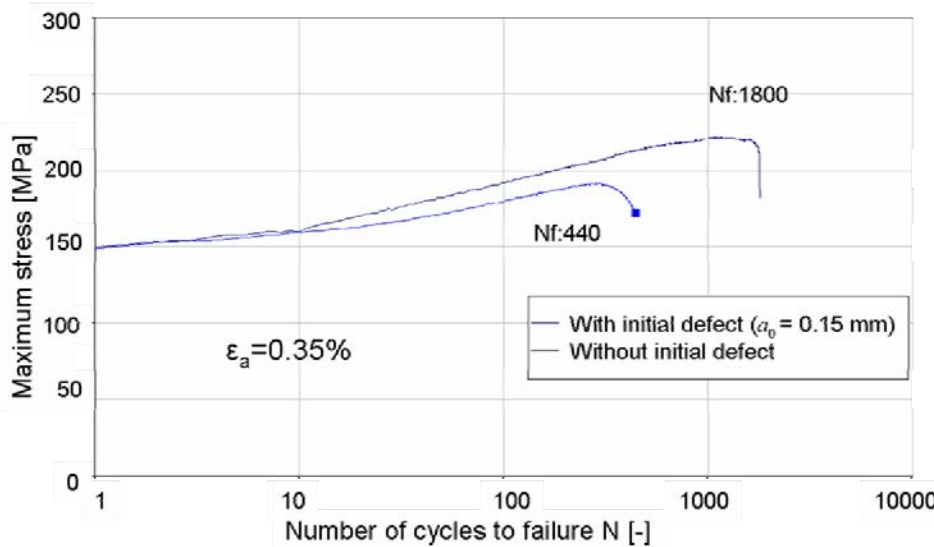


Fig. 4.16: LCF: Failure stress for specimen with and without initial defect for $\epsilon_a = 0.35\%$

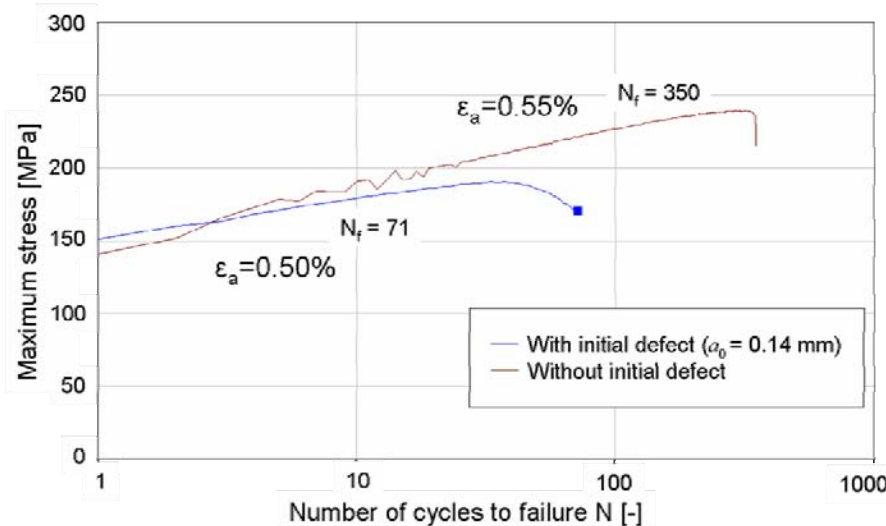


Fig. 4.17: LCF: Failure stress for specimen with and without initial defect for $\epsilon_a = 0.50\%$ and $\epsilon_a = 0.55\%$

In Fig. 4.16 and Fig. 4.17, the results of specimen with and without pre crack are shown. It can be seen that most of the tests exhibit an initial strain hardening behaviour followed by a long period of saturation stress until failure occurs. However, some specimens also show a small increase of apparent hardening before failure (see Fig. 5.8). But this characteristic is due to the failure of a specimen at the extensometer edge or it may be attributed to buckling just before failure.

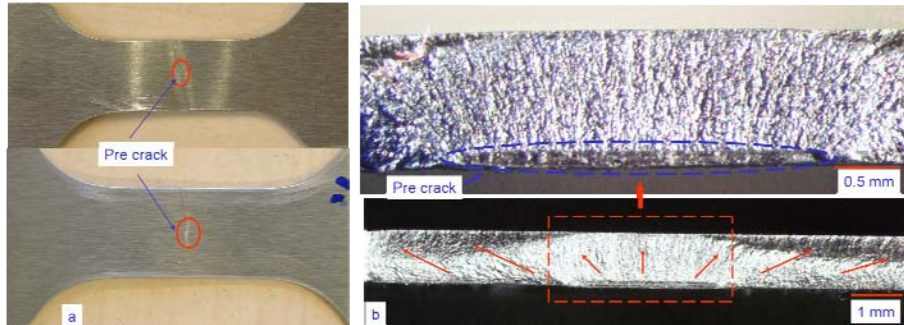


Fig. 4.18: LCF test : a) Pre crack and crack growth, b) Fractured surface

In Fig. 4.18 (a) the pre-crack for two specimens are shown. These were tested at two different strain amplitude values. It can be seen that the crack growth in both cases occurs from the pre-crack. In Fig. 4.18 (b), the fractured surface of one of the specimens is shown. Initially crack growth occurs towards the thickness direction at a slower rate followed by growth towards the width direction until rupture.

In order to obtain the strain life curve, the Manson-Coffin-Basquin relation is used. The data is plotted in Fig. 4.19 and the curves are approximated using Equ. (4.1) and Equ. (4.2).

The results show that the pre crack has a large effect on the strain life curve. In the plastic region the effect is more dominant compared to the near-elastic region. The life is reduced by a factor of more than two for a defect size of 0.14 mm in the LCF regime.

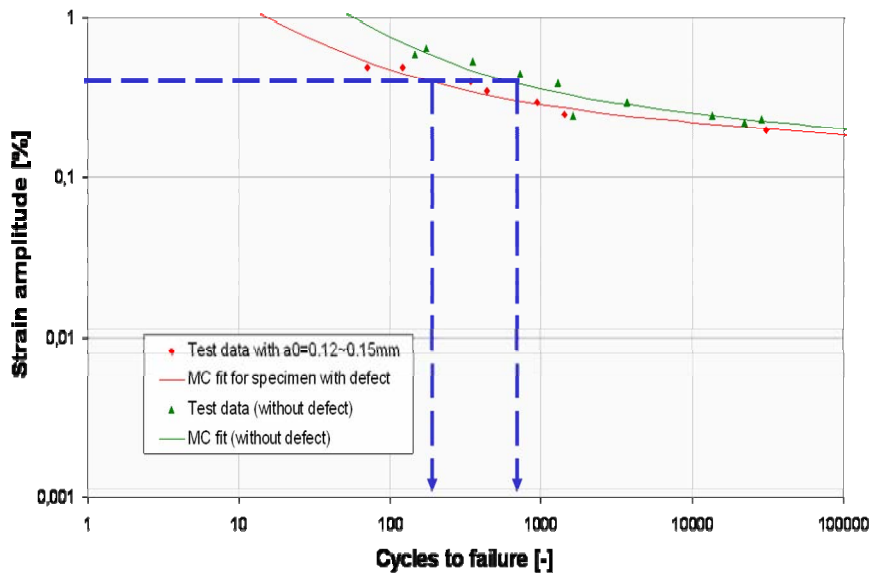


Fig. 4.19: Strain life curves for specimens with and without defect ($R = -1$)

4.4. Standard fatigue crack growth tests

For applying damage tolerant design (DTD) concepts, it is necessary to obtain the fatigue crack growth (FCG) rate. For this purpose compact tension (CT) specimens were used. Due to the smaller thickness of the sheet, a special testing set-up was conceived. Fig. 4.20 (a,b) shows the geometry of the specimen and the testing setup. The loading clevis and pins were designed in a way to avoid any possibility of fatigue modes other than mode I. The ASTM Standard E647 guidelines [33] were mostly

followed for specimen sizing, clevis and pin design and for crack growth measurement. To facilitate fatigue pre-cracking, a notch was produced by water jet cutting followed by manual polishing using super-fine grade sand paper (P1200) and filing. At the end a razor blade was used to further sharpen the notch.

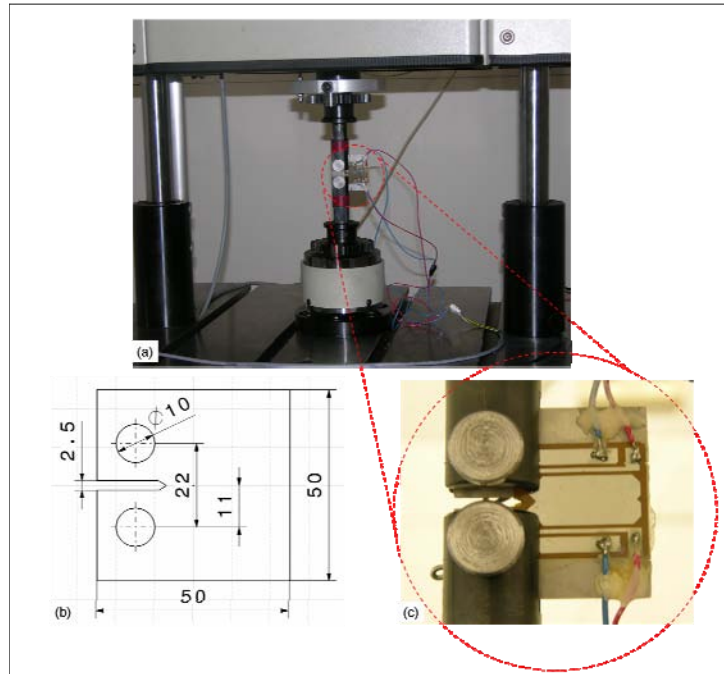


Fig. 4.20: (a) testing setup, (b) CT specimen, (c) crack gauge

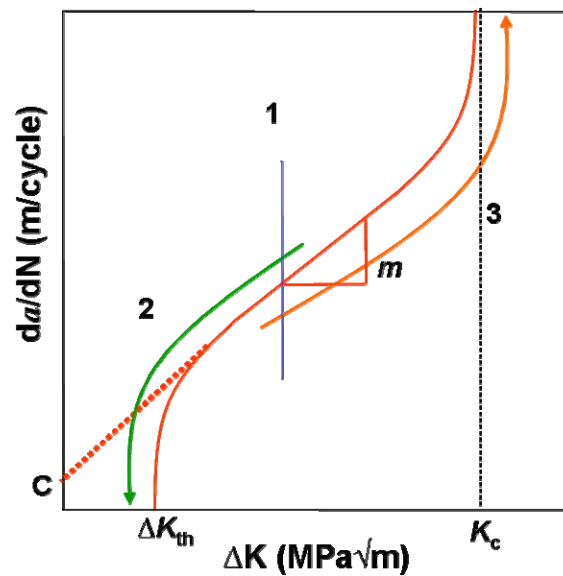


Fig. 4.21: Schematic of fatigue crack growth measurement. (1) Pre-cracking, (2) K-decreasing test, (3) Constant-force-amplitude test

The FCG tests were also carried out on an electro-magnetic resonance test rig. The crack growth was measured by a DC potential drop technique using crack gauges (Fig. 4.20 c). The tests were performed at room temperature with stress ratios R of 0, 0.2, and 0.4. The crack growth rates were obtained in three steps. Fig. 4.21 shows a schematic representation of the procedure.

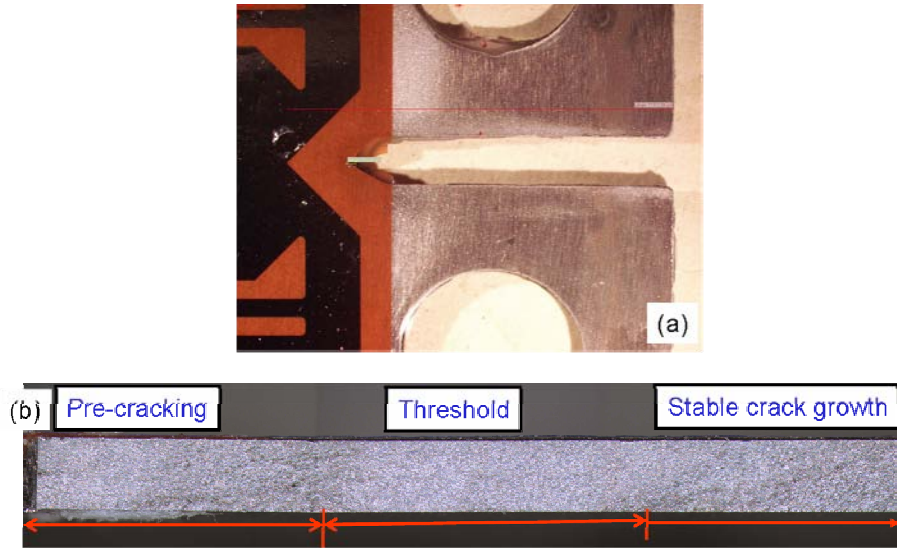


Fig. 4.22: Fatigue crack growth tests : (a) Notch with pre-crack (b) Fractured surface showing different regions

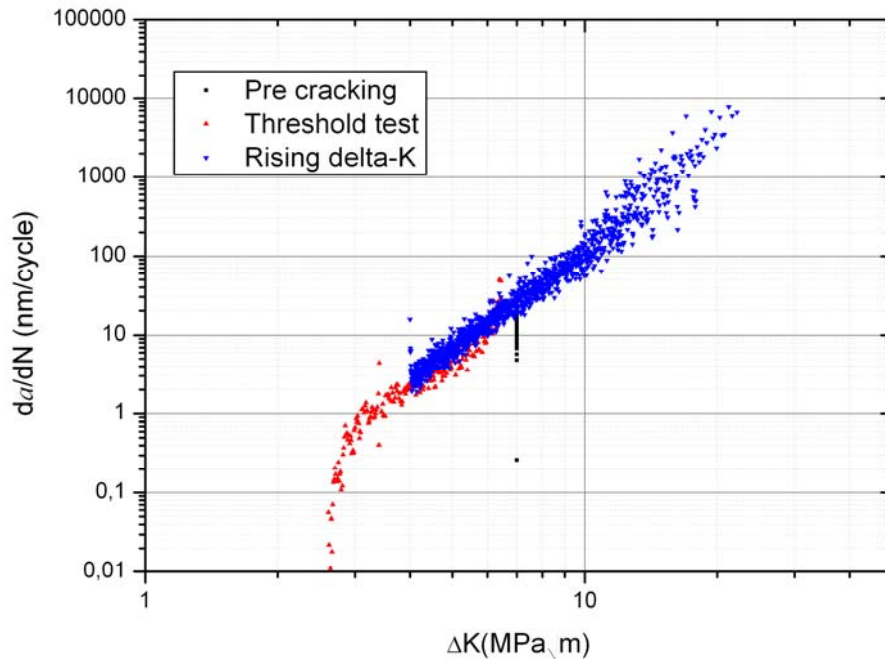


Fig. 4.23: Fatigue crack growth test at stress ratio $R = 0.2$

The methodology used is as follows:

- In order to get a sharp fatigue crack, pre-cracking is done using constant ΔK loading. For this purpose the load range is kept at about one-third of the maximum range of the FCG curve. Since it is important to keep the final K_{max} during pre-cracking not higher than the initial K_{max} for which the test has to be performed, the load ratio for pre-cracking is chosen smaller than for FCG testing.
- The next step is to obtain the FCG rate, da/dN . For this purpose a K -decreasing procedure is used. The test is started by cycling at a ΔK level equal or at about 10 percent higher than the pre-cracking values. Subsequently, the load is decreased (shed) as the crack grows and test data are recorded until the crack growth is almost zero. The criterion for the crack arrest is set

as given in [33] to da/dN values less than 10^{-10} m/cycle. Fig. 4.23 shows the result of such a test for a stress ratio $R = 0.2$.

- The final step is to obtain the crack growth rates at higher values of stress intensity range ΔK . Testing is done at constant-force-amplitude. The test is continued until the measuring limit of the crack gauge is reached.

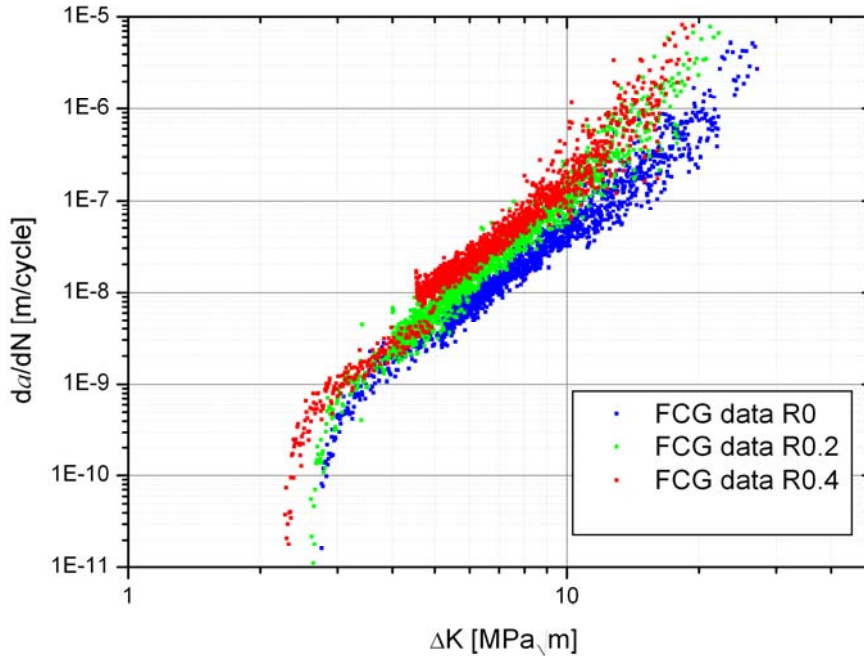


Fig. 4.24: Fatigue crack growth results for stress ratios $R = 0, 0.2, 0.4$

In Fig. 4.24, the fatigue crack growth test results for different values of R are presented. The threshold stress intensity range ΔK_{th} at a stress ratio $R = 0$ can be taken as $2.8 \text{ MPa}\sqrt{\text{m}}$. It can be seen that the threshold stress intensity range decreases with increasing R ratio. The higher value of ΔK_{th} at $R = 0$ is obviously due to crack closure effects. As the cyclic loading becomes more and more tensile, the threshold value decreases. The R -dependent threshold values can be approximated using Equ. (1.33), where ΔK_{th0} is the threshold stress intensity range at $R = 0$ and γ is constant exponent ranging from 0 to 1. In Fig. 4.25, the threshold values obtained from test results are compared with Equ. (1.33). The test data show a good agreement with the prediction by Equ. (1.33) for $\gamma = 0.5$.

On the other hand, the maximum stress intensity value, at which stable crack growth will occur, can also be approximated. This is the point where the crack growth rate is of the order of 0.01 mm/cycle . It can be seen from Fig. 4.24 that this value can be taken as $27 \text{ MPa}\sqrt{\text{m}}$ for $R = 0$. Using this value the mode I fracture toughness K_{Ic} , can also be estimated from

$$\Delta K_c = K_{Ic} (1 - R) \quad \text{Equ. (4.4)}$$

where $\Delta K_c = K_{max} - K_{min}$, giving $K_{Ic} \approx 27 \text{ MPa}\sqrt{\text{m}}$ (see Tab. 4.5)

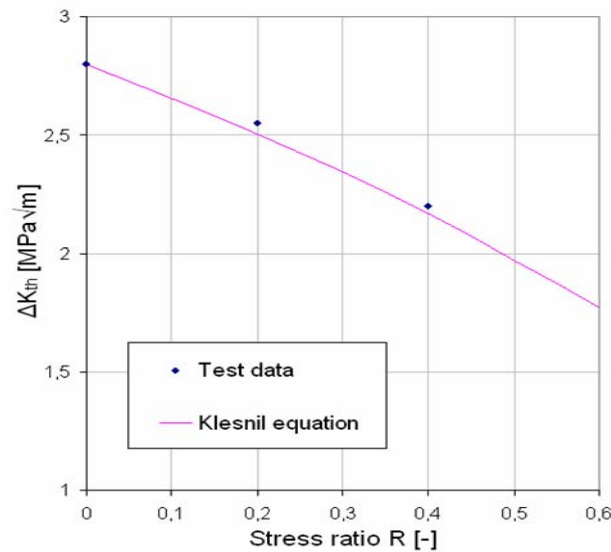


Fig. 4.25: Variation of threshold stress intensity range ΔK_{th} with stress ratio R

Stress ratio R	ΔK_{th} [MPa√m]	C	m	ΔK_c [MPa√m]	K_{Ic} [MPa√m] Equ. (4.4)
0	2.8	1.21E-11	3.754	27	27
0.2	2.6	1.8E-11	3.754	21	26.25
0.4	2.2	2.6E-11	3.754	15.5	25.8

Tab. 4.5: Fatigue crack growth data for 5083 aluminium-magnesium alloy

4.5. Residual stress measurements

The role of residual stresses is important for practical fatigue design. Welding is one of the sources by which residual stresses are induced in the material. For a material with a certain pre-existing stress, the total stress can be expressed as

$$\sigma_t = \sigma_{app} + \sigma_{res}, \quad \text{Equ. (4.5)}$$

where σ_{app} is the applied and σ_{res} is the residual stress. Under cyclic loading the applied loading is the combination of the stress amplitude σ_a and mean stress σ_m . Since the residual stress is permanently present, it will not affect the amplitude stress but will shift the mean stress. For incorporating the weld residual effect into stress-life or strain-life approaches, the applied and residual stresses are simply superposed. For assessing fatigue crack growth, separate stress intensity factors are defined such that

$$K_t = K_{app} + K_{res}, \quad \text{Equ. (4.6)}$$

where K_{res} is the residual stress intensity factor, which can be obtained directly, e.g., by means of the cut compliance method [87]

In the current case the residual stresses were measured using X-ray diffraction.

Fig. 4.26 shows one of the specimens over which the residual stresses were measured. The specimen was welded using the *tungsten inert gas* (TIG) method with the help of filler material. CrK α radiation was used to irradiate the sample with a spot diameter of 0.8 mm. The sample was exposed to radiation for about 100 seconds.

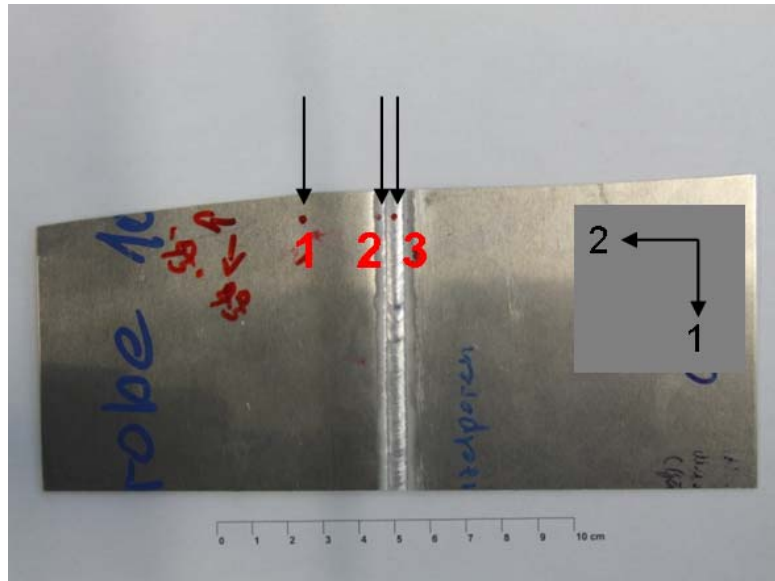


Fig. 4.26: Positions of residual stress measurement on welded specimen

The values of residual stresses were measured at different points both along the weld and perpendicular to the weld on aluminium sheet. This gives a measure of tensile and compressive stresses. The stresses were measured at three different locations¹⁰.

1. Outside the weld and HAZ (i.e., in the base material) (Point 1)
2. Near the HAZ (Point 2)
3. In the weld root (Point 3)

In case of point 3, it was not possible to take measurements directly on the surface due to the irregular shape of the weld surface. For this case material was removed by electrolysis up to a electrolytic polishing depth of 50 microns.

Measurement point	longitudinal residual stress		transverse residual stress	
	σ_1 [MPa]		σ_2 [MPa]	
1	3.3	± 8.5	-3.7	± 15.4
2	22.8	± 5.7	-18.4	± 3.9
3	46.6	± 16.3	-51.2	± 14.3

Tab. 4.6: Measured residual stresses (measurement points and directions cf. Fig. 4.26)

The results are shown in Tab. 4.6. It can be seen that the residual stresses are compressive in the transverse direction to the weld and tensile along the weld. The tensile and compressive residual stresses have maximum values within the weld and HAZ. In the weld zone the tensile and compressive residual stresses are of approximately the same value. On the other hand the stresses reach their minimum values within the base material and near the HAZ; however, a big scatter was observed at point 1 (base material).

¹⁰ Measured at Materials Centre Leoben (MCL)

5. Model Calibration

One of the major objectives of the current study is to establish a relation between the different design approaches in order to get an easy-to-use method for estimating the life of a component containing defects. As described in chapter 3, a relationship between the stress-based and DTD concepts can be obtained. The DTD concept, which is mainly based on FCG curves, can be utilised to obtain the high cycle fatigue (HCF) part of the stress-life curve.

On the other hand, an easy estimate for the behaviour at a very small number of load cycles is given by the static tensile properties of the material. The gap between the static properties and the HCF behaviour is closed by interpolation, giving thus an empirical assessment of the low cycle fatigue (LCF) behaviour.

This approach is validated by the results from strain-controlled tests in the LCF regime and from stress-controlled tests in the HCF regime as described in chapter 4.

5.1. Material without defects

5.1.1. Fatigue crack growth and HCF

The first step in obtaining the stress life curve from the crack growth results is to obtain the crack growth parameters. From literature, various functions approximating the fatigue crack growth rates are available.

These functions are integrated using different crack size limits. The simplest method for obtaining the stress based S-N curve is to use the fatigue crack growth parameters from the Paris law – $da/dN = C(\Delta K)^m$ –, where the integration is performed from an initial crack length a_i up to the final critical crack size a_f . In this case it is assumed that there are no short crack effects, the Paris law being valid only in the context of long cracks.

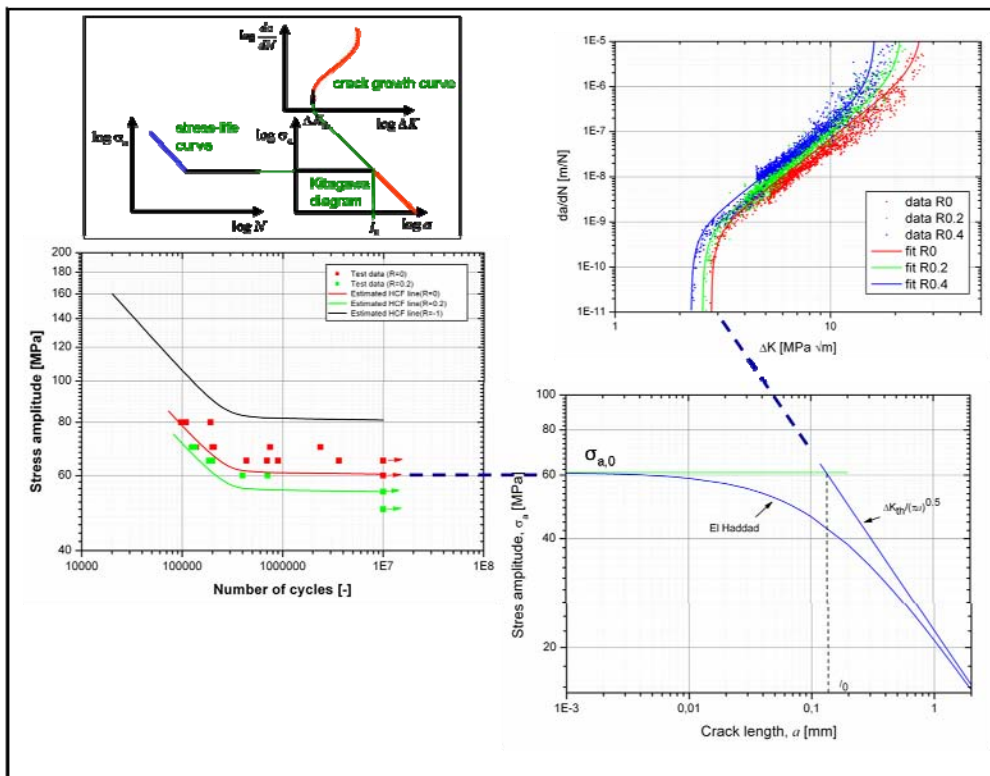


Fig. 5.1: Estimation of HCF stress life curve from fatigue crack growth curve and Kitagawa diagram

The remaining life of a cracked material is not significantly influenced by the critical crack size [5]; however, the initial crack length has a major influence on the crack growth life. For the case of a

defect-free material, the initial crack length a_i is taken equal to the material length parameter l_0 , which can be estimated from the crack growth threshold stress intensity range ΔK_{th} and the stress range at the endurance limit $\Delta\sigma_0$ by using El Haddad's equation. The schematic representation of this method, comparing prediction and experiment, is shown in Fig. 5.1.

The coefficient and exponent of the Paris equation Equ. (1.29) describing stage II of the FCG curve do not depend only on the properties of the material (age, temperature or environment) but also on load influences like the R -ratio. The limits of validity of this equation are the near-threshold regime of the stress intensity factor ΔK_{th} (region I), where crack arrest occurs, and the region of instable crack growth (region III) near $\Delta K_c = K_{Ic} / (1 - R)$.

A complete description of the crack growth for different R ratios, including the threshold, linear, and fracture stages, can be obtained by a recent model proposed by Kohout [46]. According to this model, the crack growth rate is given by Equ. (1.34). Tab. 5.1 shows the values of the parameters selected for fitting this function to the fatigue crack growth data obtained on the CT specimens as described in chapter 4.

C	1,2100E-11
K_{c0}	27
m	3,754
p	8
γ	0,42
ΔK_{th0}	2,794
n	5,813

Tab. 5.1: Values of FCG parameters used for estimating the HCF part of the S-N curve

Fig. 5.2 shows the approximation of the fatigue crack growth data using this equation. Here it is to be noted that a single set of parameters has been used for all stress ratios, allowing a simple analytical description of the fatigue crack curve for any stress ratio R .

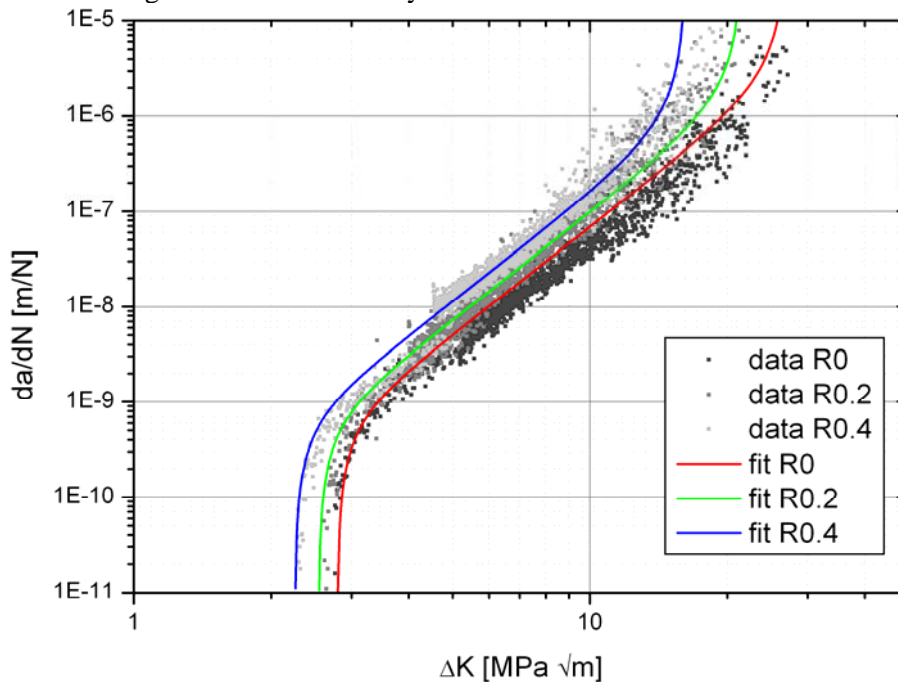


Fig. 5.2: Fatigue crack growth rate approximation using Equ. (1.34)

As described previously, for the lifetime predictions, these curves have to be integrated to obtain the number of load cycles until final fracture. As Equ. (1.34) is too complex for an analytical solution, the fatigue life is obtained by numerical integration:

$$N = \int_{a_i}^{a_f} f(C, K_{c0}, \Delta K_{th0}, R, p, m, n, \gamma) da \quad \text{Equ. (5.1)}$$

Using the method described in [73], the equation above is solved numerically to calculate the points of the S-N curve. El Haddad's equation, Equ. (3.7), can be used to obtain an intrinsic crack size for the unflawed material. With this intrinsic crack size, the stress intensity factor range for the endurance limit stress corresponds to the fatigue crack growth threshold. As the applied stress increases beyond the endurance limit stress, the stress intensity factor range exceeds the fatigue crack growth threshold, thereby leading to crack growth and failure within a number of cycles depending on the applied stress according to Equ. (5.1).

The final crack size, Equ. (3.13), is obtained using the fracture toughness and the ultimate tensile stress of the material. For the purpose of calculating the S-N curve pointwise by numerical integration of Equ. (5.1), the fracture toughness has been estimated from the critical stress intensity range ΔK_c , Equ. (4.4).

The estimated S-N curve is compared with the experimental S-N curve obtained from fatigue tests on smooth specimens (cf. chapter 4) in Fig. 5.3 for a load ratio of $R = 0$. Clearly, the parameters of the Kohout function Equ. (1.34) have an influence on the estimated S-N curve.

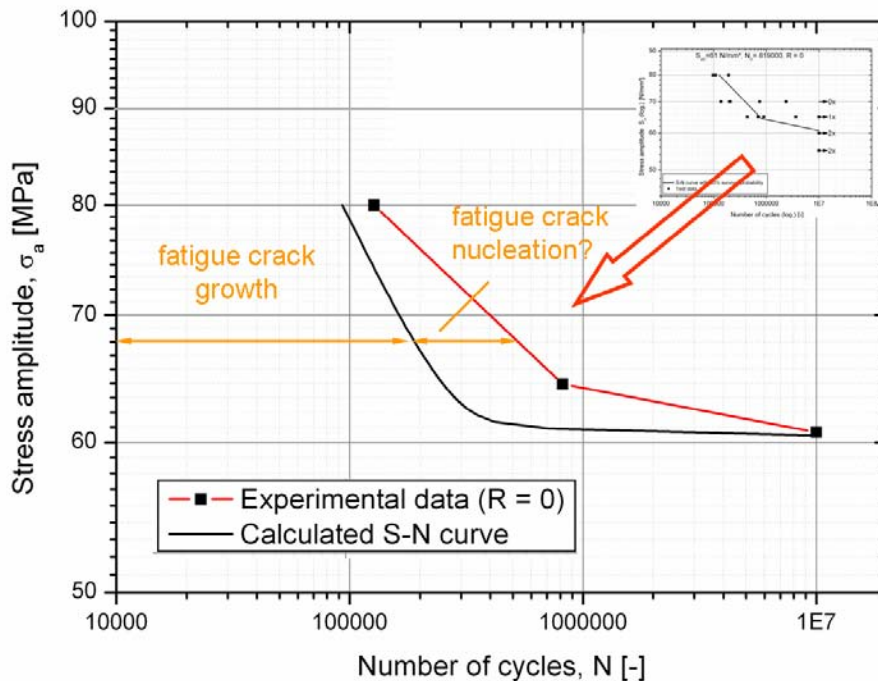


Fig. 5.3: Comparison of the estimated S-N curve with experimental results

Using the fatigue limit for an intrinsic crack length of $l_0 = 0.13$ mm obtained from Equ. (3.7), the calculated curves show a matching with experimental data at an endurance limit of 10^7 cycles. This exact coincidence is due to fixing the intrinsic crack length by means of El Haddad's Equ. (3.7). However, the results are conservative in the HCF regime. The over-conservatism in this regime of the S-N curve can be due to the fact that the estimated S-N curve has been obtained from the fatigue crack growth curve, which obviously neglects the fatigue crack initiation life time. In addition, the value of the parameter n of Equ. (1.34) has a dominant influence on the fit of the crack growth curves between

regions I (threshold) and II, and therefore on the transition between the endurance limit and the HCF regime in the S-N curve.

On the other hand, the estimated S-N curve tends towards overestimating the fatigue life in the HCF-LCF regime of the S-N curve. This is because the S-N curve estimation has been obtained on the basis of linear elastic fracture mechanics (LEFM), which loses its validity in the LCF regime where high loadings cause plastic deformation.

The slope of the S-N curve can be approximated from the slope of the of the FCG curve using Equ. (3.16). However, it is to be noted that this equation is based on the Paris equation and gives a slight difference compared to the slope of the S-N curve based on Kohout's equation. For $R = 0$ with $m = 3.75$, the slope of S-N curve obtained by Equ. (3.16) gives a value of 3.4 compared to a value of 4.3 obtained for the S-N curve from Equ. (3.19).

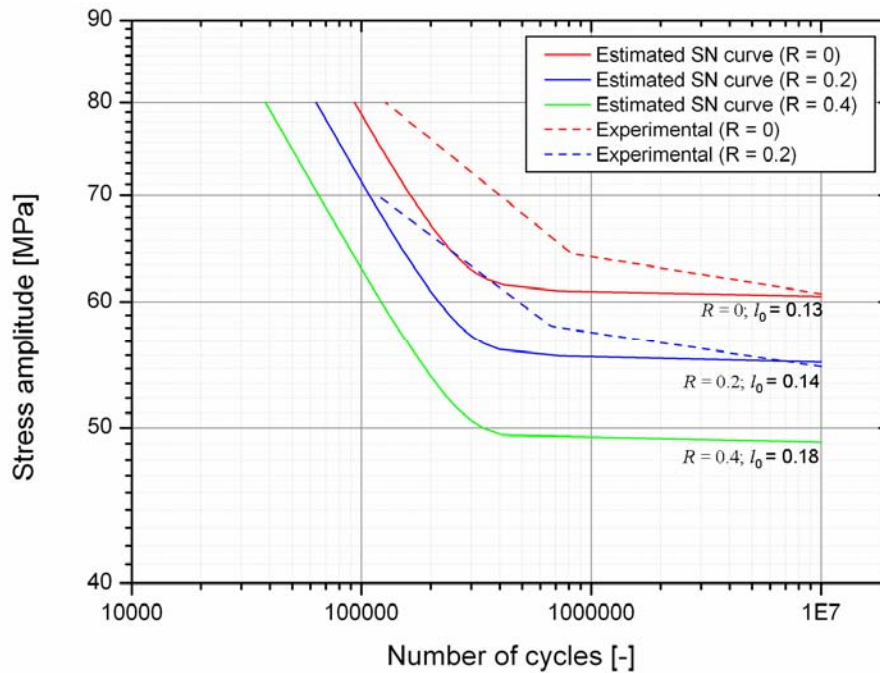


Fig. 5.4: Comparison of experimental and estimated S-N curves for different load ratios R

5.1.2. Mean stress effect in the HCF region

With the method described above it is possible to vary different parameters in Equ. (3.19). For the lifetime consideration of a particular component, not only the stress amplitude is important, but also the mean stress under which the amplitude is applied, characterized by the stress ratio R . Fig. 5.4 compares various S-N curves obtained for different stress ratios. It can be seen that the intrinsic crack size l_0 also depends on the stress ratio R as follows:

$$l_0(R) = \frac{1}{\pi} \left(\frac{\Delta K_{th}(R)}{2Y\sigma_a(R)} \right)^2 \quad \text{Equ. (5.2)}$$

Tab. 5.2 shows the values of l_0 obtained for different values of R using the above equation. In this way, it is possible to see the effect of the mean stress on the fatigue limit. Thus, a Haigh diagram can easily be constructed to study the effect of the R -ratio on the fatigue limit.

With reference to Fig. 5.4, it can be seen that the fatigue crack growth results can be utilized to obtain the stress based fatigue life curves for different stress ratios. However, the resulting S-N curves are mainly valid for the high cycle fatigue regime of the S-N curve. For high loading amplitudes above the yield strength of the material, the method becomes non-conservative.

Load ratio R [-]	Intrinsic crack length l_0 [mm]
0	0.13
0,2	0.14
0,4 ¹¹	0.18

Tab. 5.2: Values of l_0 at different load ratios R

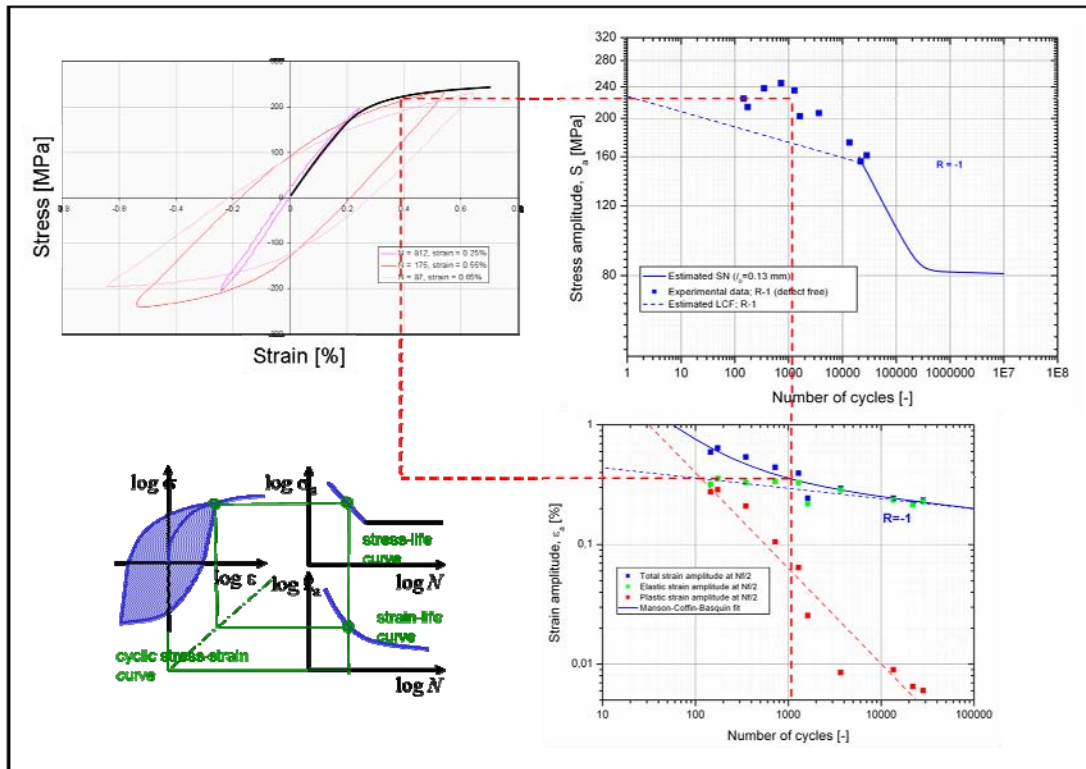


Fig. 5.5: Comparison of stress life and strain life approaches

5.1.3. Estimation of the S-N curve in the LCF regime

In order to obtain the lifetime estimate for a component under high loading (or a notched section) where stresses are in the plastic range, a strain life approach should be followed, as mentioned earlier. However, many design engineers are accustomed to using S-N curves; thus it appears promising to reformulate the strain life results within the latter framework. A possible approach is shown in Fig. 5.5, where the cyclic stress-strain curve forms the link between the two approaches.

Generally, for initially soft materials, the stress amplitude increases with increasing number of cycles at constant strain amplitude loading. However, after a few cycles stabilization will occur, leading to a nearly constant saturated stress amplitude until the point of final failure approaches. The stabilized region, where the maximum stress values are constant, is usually much larger than the regimes of initial shakedown and final failure. Thus, if the maximum stress values at half the number of cycles to failure ($N_f/2$) are taken, it will be possible to link LCF (constant-strain) ϵ -N and HCF (constant-stress) S-N curves.

¹¹ Obtained by using the interpolated value of σ_a from $R = 0.5$

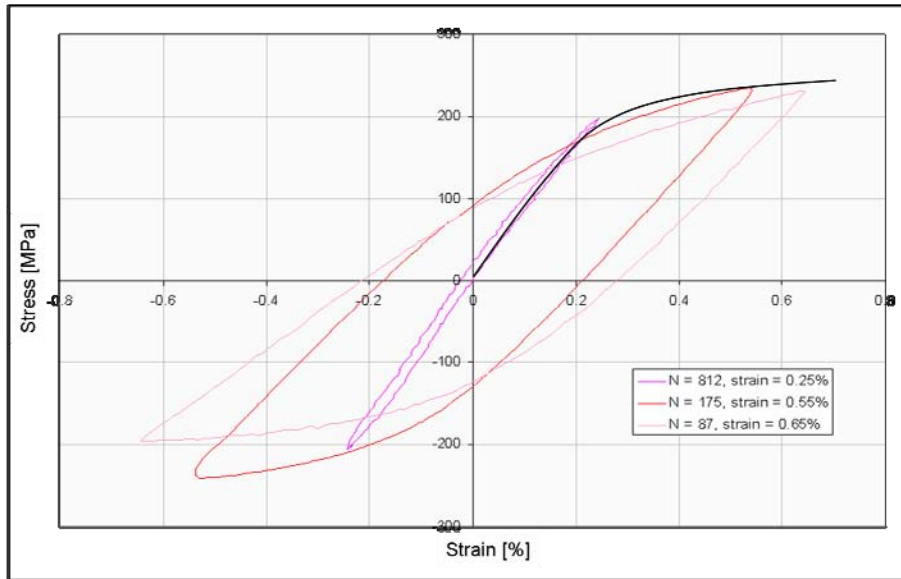


Fig. 5.6: Saturation stresses (at half-lifetime) versus strain amplitude

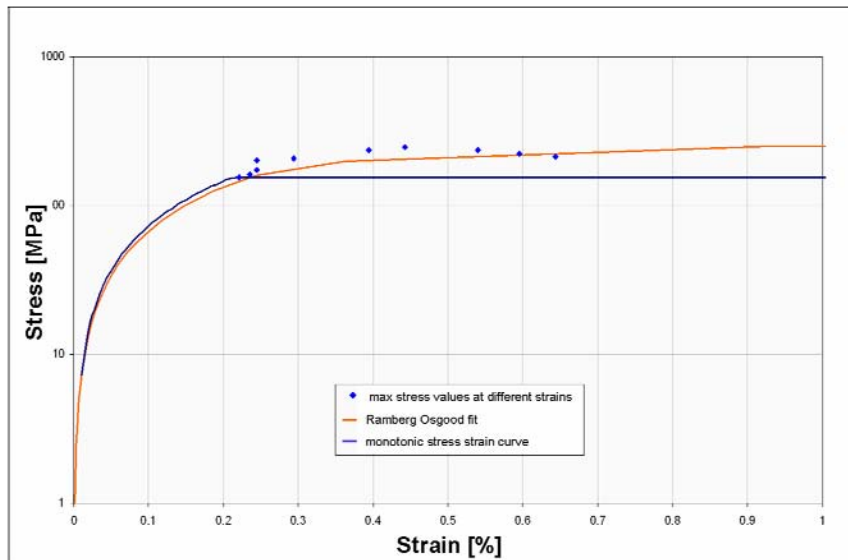


Fig. 5.7: Monotonic and cyclic stress-strain behaviour of the material

In Fig. 5.6, the maximum stress values at half the number of life cycles are shown for different strain amplitudes. The change of the elastic slope can be attributed to cyclic damage. The maximum stress values at different strain amplitudes will in turn give a cyclic stress-strain curve (CSSC), Fig. 5.7. These data points can be approximated using the Ramberg-Osgood relation, Equ. (3.20) (cf. chapter 3).

With reference to the LCF data in Fig. 4.11, the hardening behaviour of the material for some of the strain amplitudes is shown in Fig. 5.8. The material exhibits an initial strain hardening behaviour followed by a long period of saturation until failure occurs. Clearly, the behaviour is dominated by the stabilized regime (see also sections 4.2.2 and 4.3.2).

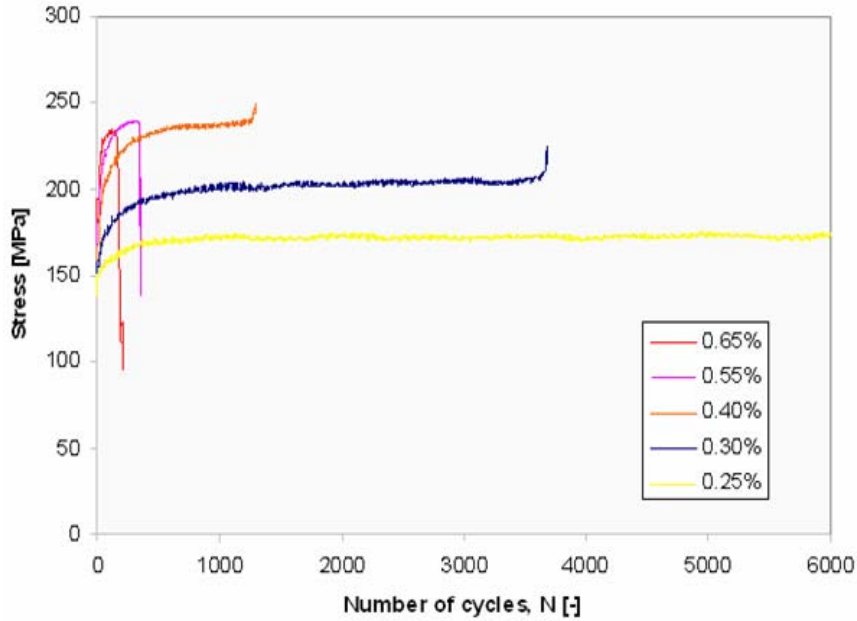


Fig. 5.8: Cyclic stress response curves at different strain amplitudes

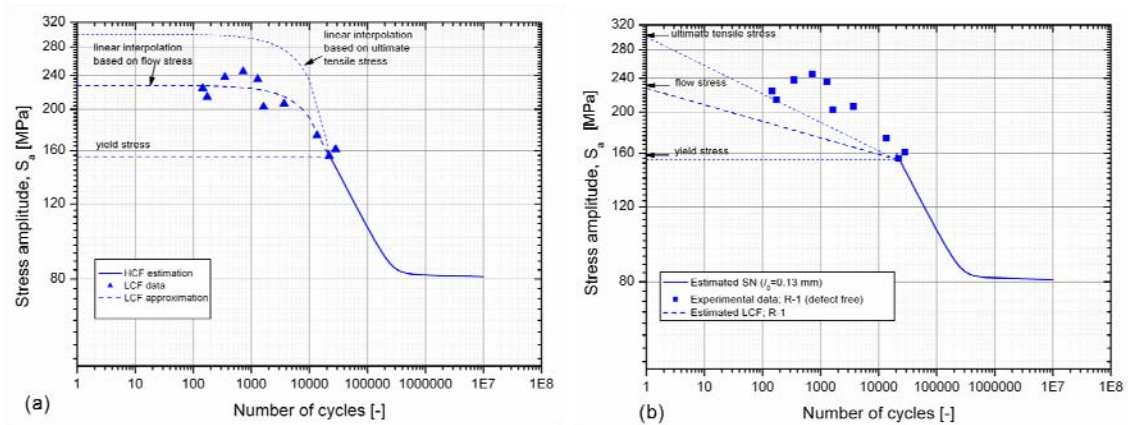


Fig. 5.9: LCF estimation using (a) linear, (b) log-linear interpolation ($R = -1$); comparison with experimental data

The stabilized stress values obtained as a result of the strain controlled tests at various constant strain amplitudes are shown in Fig. 5.9 (cf. section 3.5). The S-N curve for a load ratio $R = -1$ in the high cycle fatigue regime has been estimated from the fatigue crack growth values using the procedure detailed in previous section.

A prediction for the LCF regime within the stress based S-N diagram can be obtained using the HCF curve and the tensile properties of the material. Fig. 5.9 presents various possibilities for such an estimation of the LCF regime. The starting point of the LCF regime can be taken as the yield, ultimate tensile, or flow stress (the flow stress is the average of the yield stress and the ultimate tensile stress) at a cycle count of one (static failure). In Tab. 5.3, values of yield, ultimate tensile and flow stress are presented. According to [88], the stress amplitude at the yield limit must satisfy the relation

$$\sigma_{y,R} < \sigma_y \frac{(1-R)}{2}. \quad \text{Equ. (5.3)}$$

The same is applied to the flow and ultimate tensile stresses.

The connection between the LCF and HCF regimes is obtained where the yield limit of the material intersects the S-N curve estimated from the FCG properties.

The LCF curve in between these two points can be estimated by linear interpolation. Using Equ. (3.23), such an approximation is shown in Fig. 5.9 (a), again considering yield stress, ultimate tensile stress and flow stress as starting points. Clearly, the LCF estimate using the ultimate tensile stress as the starting point will give an upper bound. The LCF data points are clustered near the line which has been obtained using linear interpolation between the flow stress and the intersection of yield limit and FCG estimate of the S-N curve.

Stress amplitude	$R = -1$	$R = -0.2$	$R = 0$	$R = 0.2$
corresponding to the yield stress R_e [MPa]	155	93	77.5	62
corresponding to the ultimate tensile stress R_m [MPa]	300	180	150	120
corresponding to the flow stress σ_f [MPa]	227.5	136.5	113.75	91

Tab. 5.3: Stress amplitudes corresponding to the tensile and yield values of the material at different load ratios

Another way of predicting the LCF regime within the stress based framework is to use a straight line between the two limits – the intersection of yield limit to the S-N curve from FCG curve and the yield stress, flow stress or ultimate tensile stress – in the log-log diagram (log-linear interpolation). Such lines are shown in Fig. 5.9 (b). Again, it can be seen that using the flow stress a better approximation is obtained.

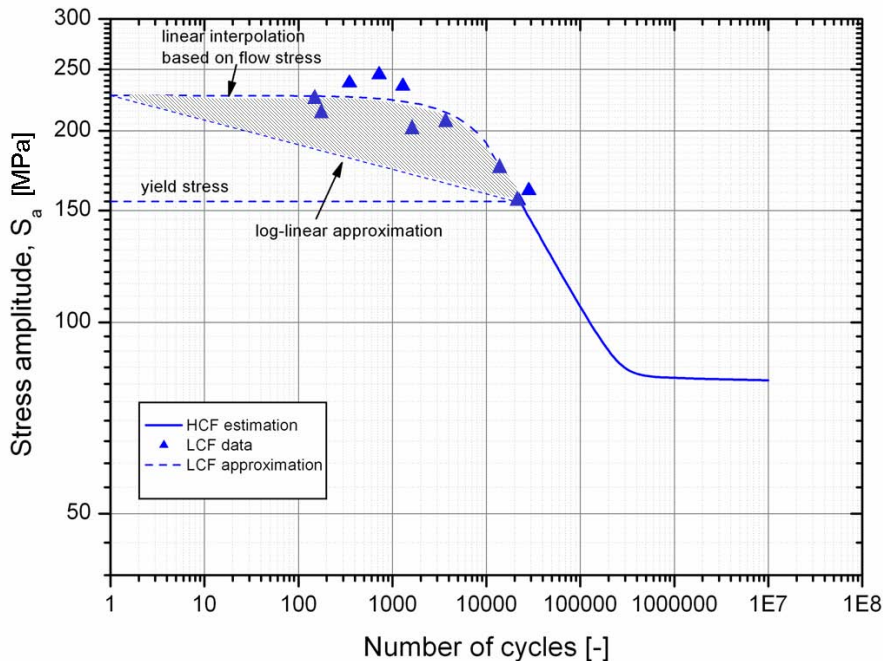


Fig. 5.10: Estimated HCF and LCF curves for a stress ratio $R = -1$

A comparison between the two methods above is shown in Fig. 5.10. Here, both approximations are shown using the flow stress as the starting point for the LCF regime. The stabilized stress values obtained for different strain amplitudes from the strain-controlled LCF experiments are also plotted. It can be seen that, by taking the flow stress as a starting point and using the log-linear interpolation, a lower bound for the LCF behaviour is obtained, whereas the linear interpolation fits the experimental values rather satisfactorily.

5.1.4. Mean stress effects in the LCF region

The mean stress influence has been shown for the HCF regime in section 5.1.2 (cf. Fig. 5.4). For the LCF regime, there are various models for the effect of the stress ratio. Two of them are more widely used – the Morrow model and the Smith-Watson-Topper (SWT) model. For comparing the results, LCF tests were conducted at stress ratios $R = -1$ and $R = -0.2$.

According to Morrow [20], the mean stress effect is modelled by modifying the elastic part of the total strain value as given in Equ. (1.14). This estimate is shown in Fig. 5.11.

On the other hand, the Smith-Watson-Topper (SWT) [21] relation modifies both the elastic and plastic parts of the Manson-Coffin-Basquin relation. This method uses the maximum stress (σ_{max}) of the hysteresis loop instead of the mean stress. Equ. (1.16)., A comparison of the strain life curves for $R = -1$ and $R = -0.2$ using this equation is shown in Fig. 5.12.

It can be seen that both models over-estimate the mean stress influence grossly. Looking into the experimental data for $R = -1$ and $R = -0.2$, the mean stress has even less influence in the LCF regime than in the HCF regime.

Another estimate for the effect of the mean stress on the LCF regime is obtained using the method described in section 5.1.3. In this case, the effect of the stress ratio on the yield limit, Equ. (5.3), can be used. The predicted stress life curves for a defect-free material at different load ratios are shown along with the experimental data in Fig. 5.13. The influence of the stress ratio in the HCF regime has been obtained by the method already described (cf. section 5.1.2). For the LCF case, the change at the yield limit was taken following Equ. (5.3). Keeping the slope of the stress life curve in the LCF regime constant, A conservative estimate of the quasi-static limit is obtained by applying

Equ. (5.3) to the flow stress, i.e., keeping a constant ratio of yield stress vs. flow stress for any stress ratio:

$$\sigma_{f,R} = \frac{\sigma_f}{\sigma_y} \cdot \sigma_{y,R} \quad \text{Equ. (5.4)}$$

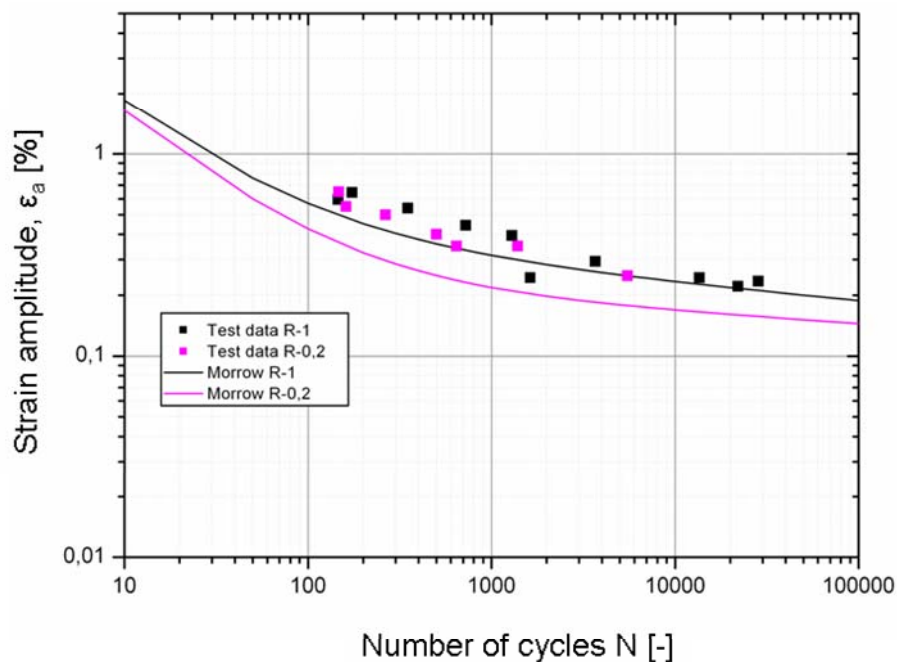


Fig. 5.11: LCF: mean stress effect using the Morrow approach

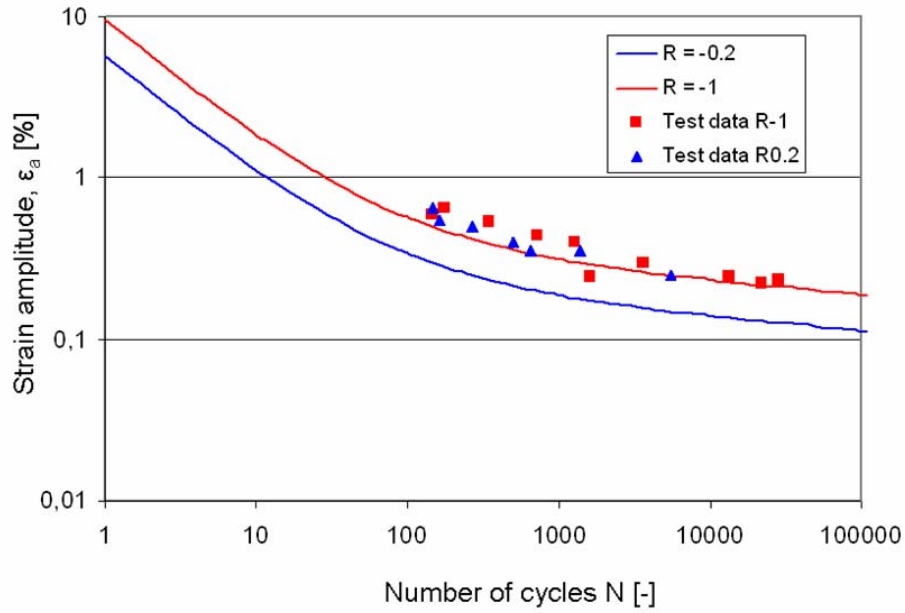


Fig. 5.12: LCF: mean stress effect using the SWT approach

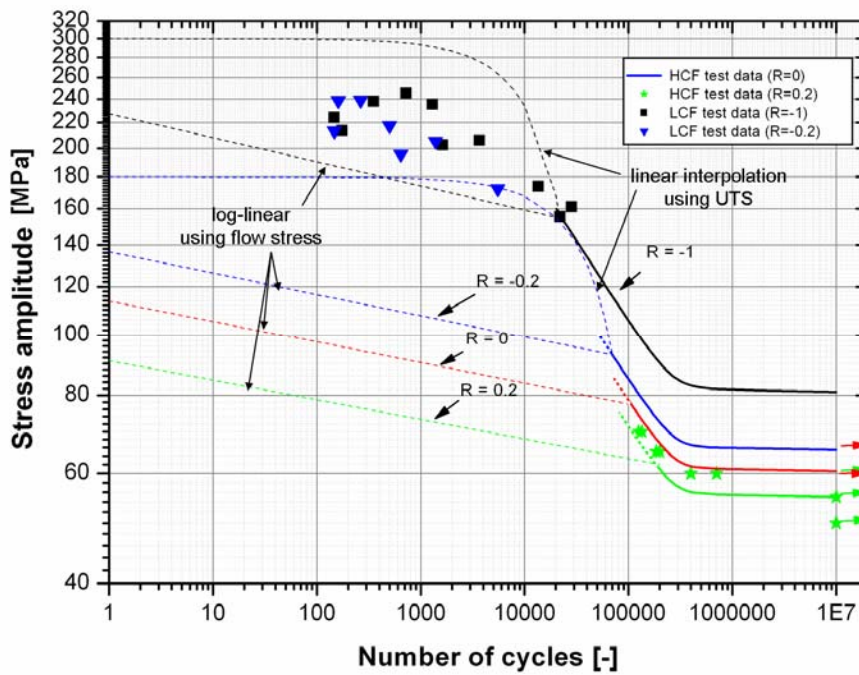


Fig. 5.13: Estimation of stress based S-N curve for a defect free material at different load ratios

5.2. Material with defects

5.2.1. Estimation of the HCF-endurance regime

A schematic representation of obtaining the stress life curve from the fatigue crack growth properties for a material containing defects has been shown in Fig. 5.14. Here, the actual flaw size a replaces the intrinsic flaw size l_0 of the defect-free material.

With reference to Fig. 5.14, it can be seen that the Kitagawa diagram can also be generalized to obtain the stress life curve for a material containing defects in the finite life regime. Considering a material which contains a certain initial defect, this will be represented by a point that it is already in the crack growth regime of the crack growth curve.

Equ. (3.8) is recalled here. The same equation can be written a

$$\Delta K = Y\Delta\sigma\sqrt{\pi(a+l_0)} \quad \text{Equ. (5.5)}$$

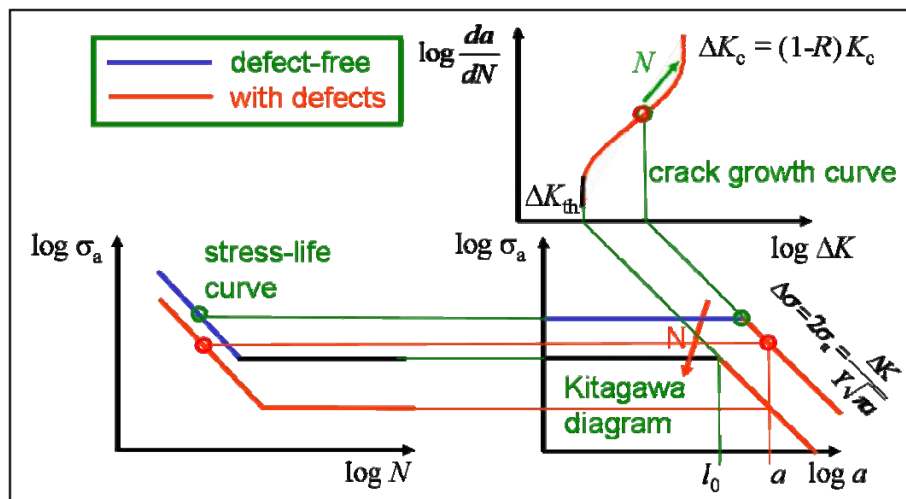


Fig. 5.14: Schematic representation of obtaining the stress life curve for a material containing defects

The above equation can provide the endurance limit for a material containing a crack of length a . Here it is to be noted that the length parameter l_0 given by El Haddad's Equ. (3.7) defines the endurance limit for a material with no defects, $a = 0$. Thus, setting $a = 0$ in the equation above will give the stress range at the endurance limit of the defect-free material.

For stresses higher than the endurance limit, the number of cycles to failure is obtained by numerical integration of the Kohout function, now using the actual defect size as the lower integration limit. Fig. 5.15 shows the estimation of the HCF-endurance part of the stress life curve for different defect sizes. It is obvious that the fatigue limit is decreasing with increasing initial defect size. Alternatively, an admissible maximum initial flaw size can also be determined for a given number of cycles provided the applied loading is known.

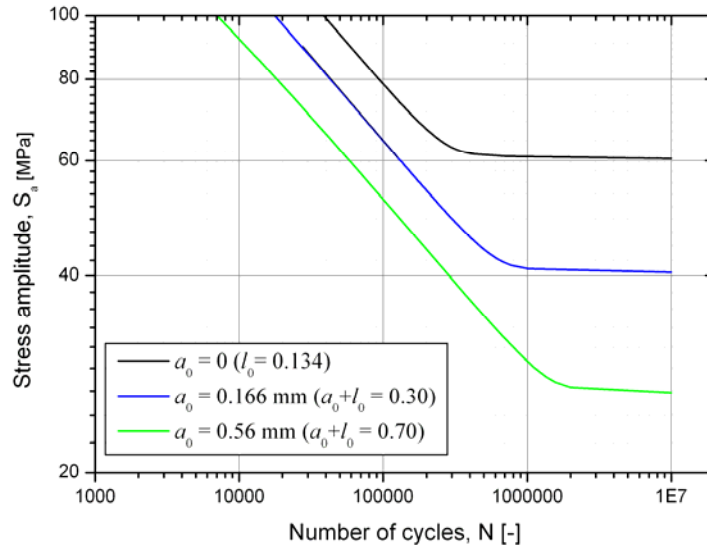


Fig. 5.15: Estimation of S-N curve (HCF-endurance regimes) for material containing defects ($R = 0$)

The stress life curve obtained from FCG data is compared with experimental S-N data for a specimen with defects in Fig. 5.16. The HCF tests were performed on two types of specimens (cf. section 4.3.1). For the type 1, for many of the specimens the crack did not grow from the initial defect, instead it started from one of the sides of the specimen. These data points have been shown as outliers in Fig. 5.16. One of the reasons for such behaviour could be the fact that the cracks were generated by means of a sharp knife, thereby introducing some plasticity-induced hardening at the rims. The apparent presence of plastic regions around the crack tips results in a higher applied stress needed for the crack to grow. This effect can be seen from the result of a similar specimen tested at a load amplitude higher than the elastic limit of the material, cf. Fig. 4.15 b, where crack growth started again at the initial defect.

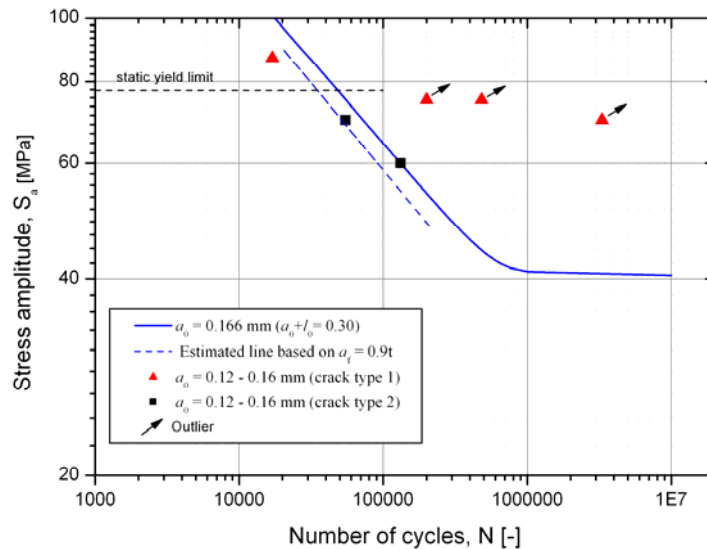


Fig. 5.16: Comparison of estimation with experimental results ($R = 0$)

On the other hand, in specimens with a crack of type 2, crack propagation occurred from the initial defect. Obviously the ends in the length direction were sharp enough for the crack to grow. Moreover, the lower constraint at the ends also facilitated crack growth (cf. Fig. 4.15c).

In Fig. 5.16, the estimated stress life curve is shown for a defect size $a_0 = 0.166$ mm. It is to mention here that by this way the total crack length becomes $a_0 + l_0 = 0.30$ mm, keeping the intrinsic size l_0 as calculated from Equ. (3.7). In the HCF regime the data points are confirming the estimated fatigue

curve. The specimen tested at load amplitudes higher than the yield limit indicates clearly that the estimated S-N curve loses its validity in the LCF regime.

On the other hand, one of the data points in the HCF regime is lying on the lower side of the estimate. This can be understood from the fact that the calculated curve (solid line) is based on the final crack size a_f , Equ. (3.13), obtained from the critical stress intensity range of the material. As this final crack size exceeds the actual thickness of the specimen, a different assumption is necessary here. If the final crack size is taken as a fraction of the actual thickness of the specimen, the crack growth life will be reduced for thin sheets as in the present case. As final forced rupture occurs before the fatigue crack has grown fully through the thickness t of the specimen, a_f is taken as $0.9t$ as an engineering assumption. A corresponding line is shown in Fig. 5.16, giving good agreement with the experimental data.

5.2.2. Estimation of the LCF regime

From Fig. 5.15, it can be seen that the S-N curve obtained from the FCG properties for different load ratio is not valid in the LCF regime. However, an approximate estimate of the LCF behaviour can be obtained similar to the one proposed for the defect-free case.

To this purpose, the concept of net section yielding (NSY) is exploited here. For a cracked specimen, the onset of yielding can be taken at the point where the applied force divided by the remaining section of the specimen (the net section) reaches the yield stress. For a specimen with a surface crack of depth a and thickness t , the yield limit σ_{yd} can be obtained as

$$\sigma_{yd} = \sigma_y \left(1 - \frac{a}{t} \right), \quad \text{Equ. (5.6)}$$

where σ_y is the yield stress of the un-cracked material and for simplicity any stress concentration effects have been neglected. Conversely, the crack size at the onset of net section yielding is determined by

$$a_f = t \left(1 - \frac{\sigma}{\sigma_y} \right). \quad \text{Equ. (5.7)}$$

For a defect-free material, the LCF prediction was based on the yield and flow stresses (cf. section 5.1.3). The same model can also be used for a material containing defects [84]. The yield limit, obtained from NSY, intersecting the HCF curve will give the point where the material behaviour becomes plastic. Thus, for a material with a defect of size a_0 the yield load can be used to estimate the beginning of the LCF regime, which can be taken equal to $\sim 2 \times 10^4$ cycles in this case.

For obtaining a point at $N = 1$, for the material with defect, the slope of LCF for a material without defect can be used to estimate the flow stress σ_f or ultimate stress σ_u

$$\sigma_{fd} = \frac{\sigma_f}{\sigma_y} \sigma_{yd}, \quad \text{Equ. (5.8)}$$

where σ_{yd} and σ_{fd} correspond to the yield and flow stress for a material with a defect, respectively. As stated before, in this case σ_{yd} is obtained from the NSY criterion, Equ. (5.6).

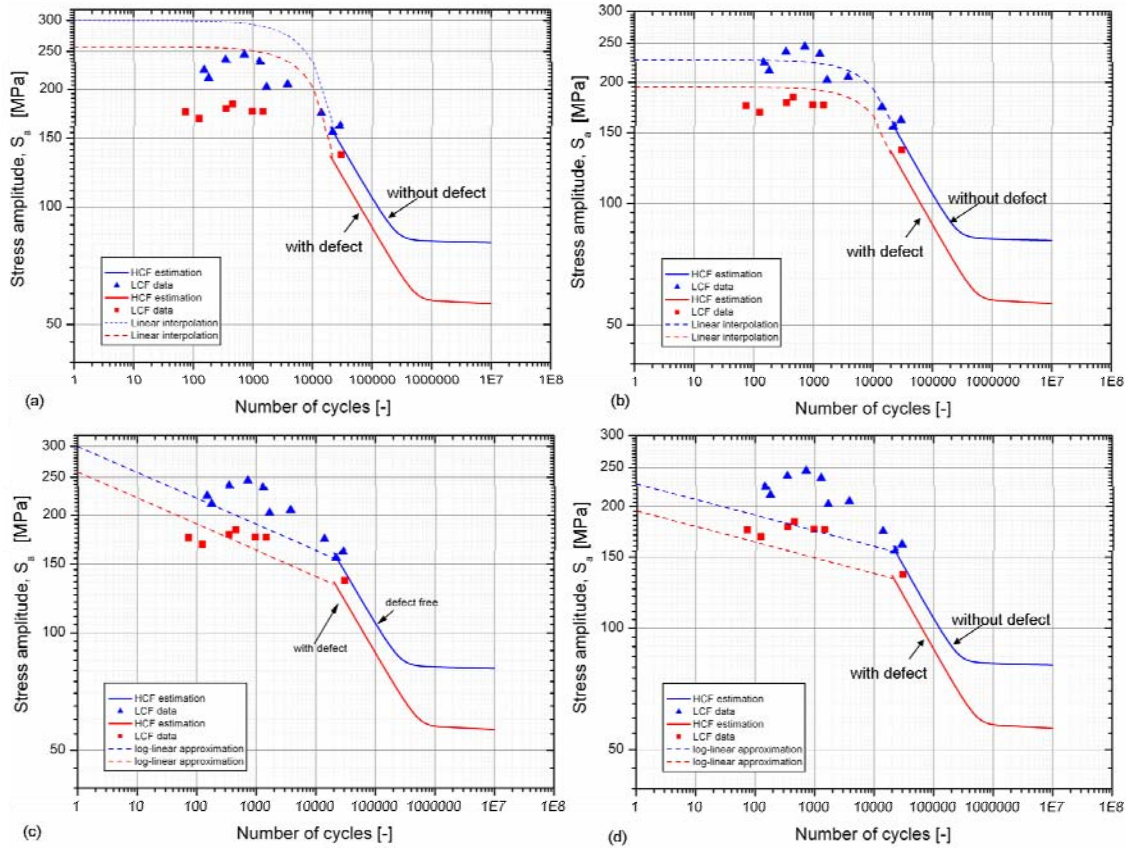


Fig. 5.17: Possible consideration for approximating the LCF regime within the stress based diagram for defect containing and defect free material using linear interpolation and (a) ultimate tensile strength, (b) flow stress and using log-linear and (c) ultimate st

Using Equ. (5.6) and Equ. (5.8), values of yield stress, tensile stress and flow stress for a material with and without defect are listed in Tab. 5.4.

Similar to the defect-free material, LCF predictions can also be obtained in this case using various possibilities, i.e., linear and log-linear interpolation. In Fig. 5.17 (a), a linear interpolation between the ultimate stress and the yield stress is shown. Using Equ. (3.23), predictions for both defect free and defect containing cases have been obtained. It can be seen that for both cases the use of the ultimate stress gives an upper bound to the experimental data. In Fig. 5.17 (b) the linear interpolation between the flow stress and yield stress has been used. Although for the defect-free case Equ. (3.23) gives a fit to the average of the experimental results, for the defect containing case it gives an upper bound to the test data.

Material parameter	Defect-free	With defect ($a = 0.14 \text{ mm}$)
Yield stress R_e [MPa]	155	133
Ultimate tensile stress R_m [MPa]	300	258
Flow stress σ_f [MPa]	227.5	195

Tab. 5.4: Tensile and yield values of the material with and without defect

On the other hand, the log-linear interpolation of the LCF behaviour is defined by Equ. (3.24) and Equ. (3.25). Fig. 5.17 (c) and (d) show these predictions using the ultimate tensile stress and flow stress, respectively. Clearly, the latter provides a lower bound to the experimental data in both the defect free and defect containing cases.

Thus it can be concluded that the use of ultimate tensile strength value in Equ. (3.23) will lead to an upper bound LCF prediction (Fig. 5.17 (a)), whereas the latter approximation using the flow stress provides a lower bound LCF prediction (Fig. 5.17 (d)).

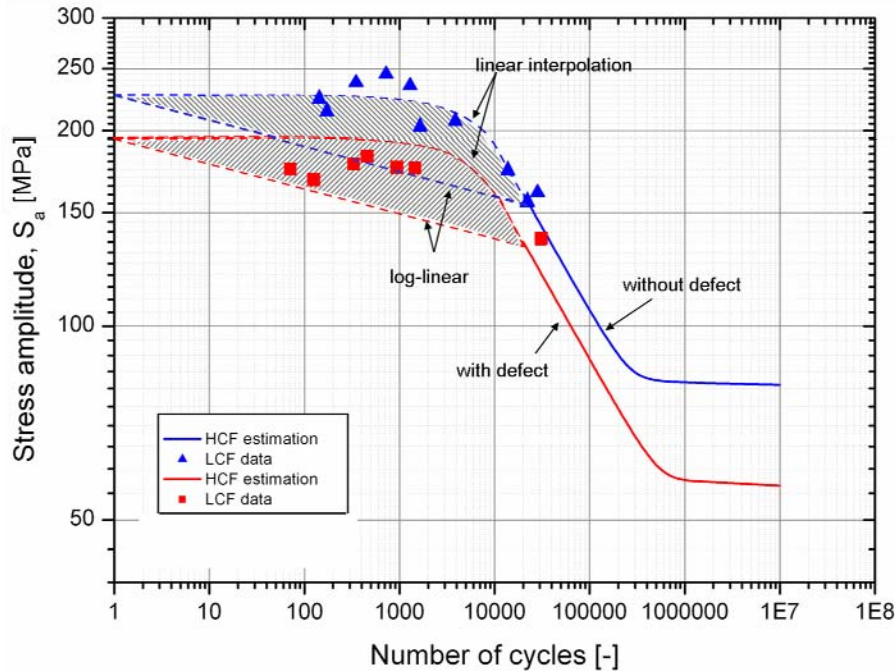


Fig. 5.18: Estimation of stress life curve for a material with a defect ($R = -1$)

In Fig. 5.18 the above two methods are shown using the flow stress. Here, both LCF and HCF predictions for a material with and without defect are presented. The comparison of HCF predictions with experimental data has already been discussed (section 5.2.1). The LCF test data for a material with a defect size a_0 are included. The log-linear interpolation method gives a lower bound to the test results for both damaged and undamaged materials. The linear interpolation method gives an upper bound for the damaged material, and a good average fit for the undamaged material

The limiting predicted value for the static loading (i.e., at $N = 1$) for a material with a defect size a_0 can also be verified following the net section yielding (NSY) concept using the area ratio of the specimen with and without defect. Keeping the width of the specimen constant, this ratio will be $(t - a_0)/t$, where t is the thickness of the specimen. Application to the flow stress gives

$$\frac{\sigma_{fd}}{\sigma_f} = \frac{t - a_0}{t} \quad \text{Equ. (5.9).}$$

5.2.3. Estimation of HCF-LCF based on net section stresses

In the methodologies detailed above, the NSY concept was used only to obtain an intersection point at LCF-HCF for a material with a defect. The same can also be used for estimating the HCF and LCF regimes for a material containing a defect. In this case, the Paris or Kohout equation for the fatigue crack growth is integrated between an initial defect size a_0 and a final crack size a_f obtained from

- net section yielding (NSY),
- net section flow stress, or
- net section ultimate stress,

respectively. Fig. 5.19 shows the various crack lengths at which the remaining ligament of the specimen with a surface crack will attain the yield stress, flow stress, and ultimate stress.

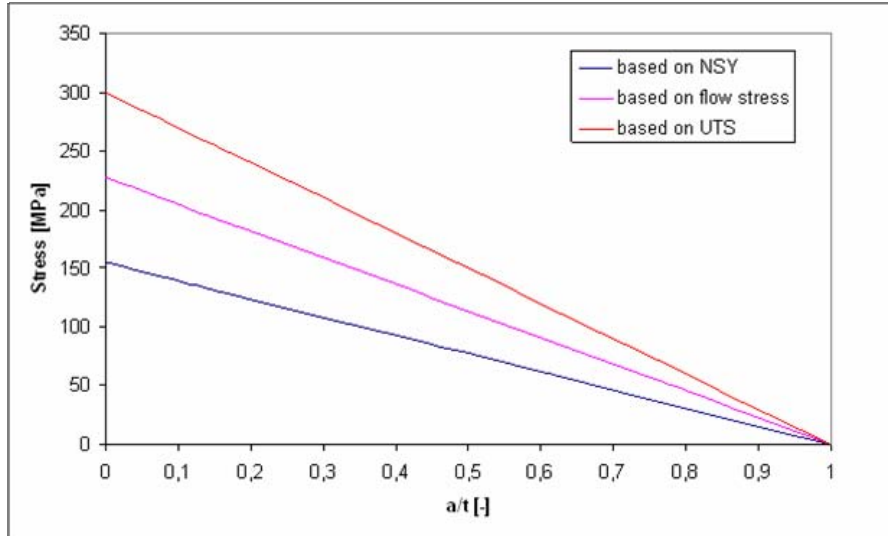


Fig. 5.19: Failure stress based on NSY and flow stress

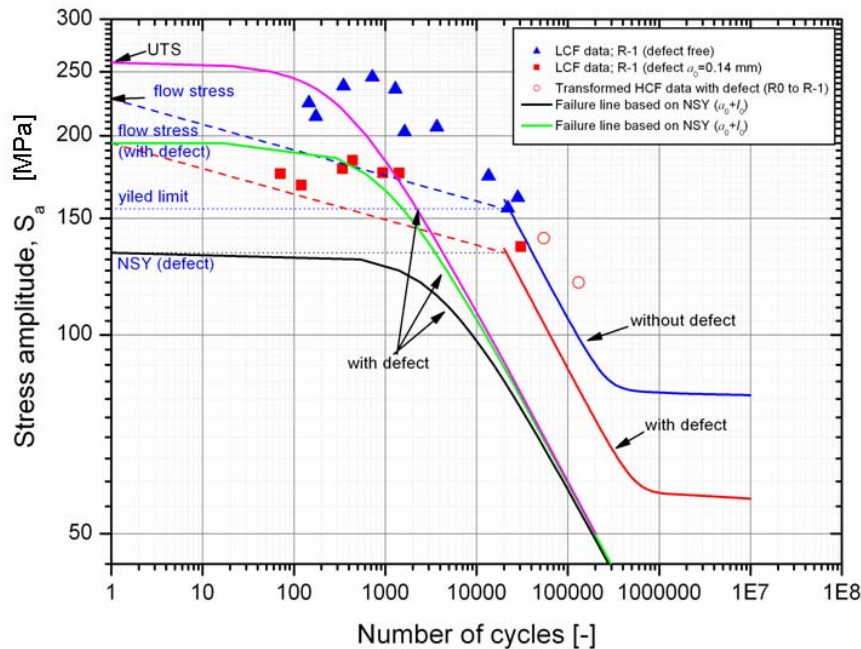


Fig. 5.20: S-N curves obtained from final crack sizes based on NSY and flow stress

In Fig. 5.20, the three curves obtained from the FCG curves with the final crack size from net section yielding, net section flow stress, and net section ultimate stress are compared with the curves based on a final crack size obtained from the fracture toughness of the material. Again, the stress intensity factor range is a function of initial crack length and intrinsic crack length, a_0+l_0 , as given in Equ. (5.5).

Obviously, the NSY based curve shows a more conservative behaviour with respect to the estimated S-N curve for a material with an initial defect size a_0+l_0 and final crack size a_f obtained from the fracture toughness K_{Ic} , cf. Equ. (3.13). The test data points (transformed from $R = 0$ to $R = -1$ using $\sigma_{a,R=-1} = 2\sigma_{a,R=0}$) for a defect size of $a_0 \approx 0.14$ mm show that both estimated curves in the HCF regime are on the conservative side.

5.3. Residual stress effects

Using the methodology above, the effect of residual stresses can also be obtained within the stress based S-N diagram. As these stresses are permanently present within the structure, they act like a mean stress. Thus, tensile residual stresses will tend to raise the mean stress and consequently reduce the fatigue life.

For the welded aluminium sheet, the residual stress measurements have been discussed in section 4.5. Referring to Fig. 4.26 the stresses were measured at different locations. Evidently, the tensile residual stresses raising the mean stress in the weld will have a major influence on fatigue life.

The effect of tensile residual stresses on the stress life curve for an undamaged material is shown in Fig. 5.21. The analysis has been carried out based on the following assumptions: the loading is considered to be in the weld direction and the residual stress obtained at point 2 (cf. Fig. 4.26), $\sigma_{res} = 22.8$ MPa, has been assumed to be uniform for the whole area. The methodology described previously for estimating the fatigue life curve has been used (see also [102]). It is emphasized that, as the mean stress is assumed to be constant, the specimen experiences different load ratios at various load amplitudes, cf. Equ. (1.4). The fatigue life for various load amplitudes and constant mean stress of 22.8 MPa (and hence different R ratios for each point) was calculated using the crack growth properties (see green triangles in Fig. 5.21). It can be seen that the slope of the curve tends to be the same as for a material without a weld in the HCF region. However, further experimental verification is still needed.

For the LCF prediction, the flow stress has been lowered by the amount of the residual stress:

$$\sigma_{f,Res} = \sigma_f - \sigma_{Res} \quad \text{Equ. (5.10)}$$

This provides the initial point for the LCF estimation. The slope of the S-N curve in the LCF regime corresponds to that of a specimen without residual stress (cf. section 3.5).

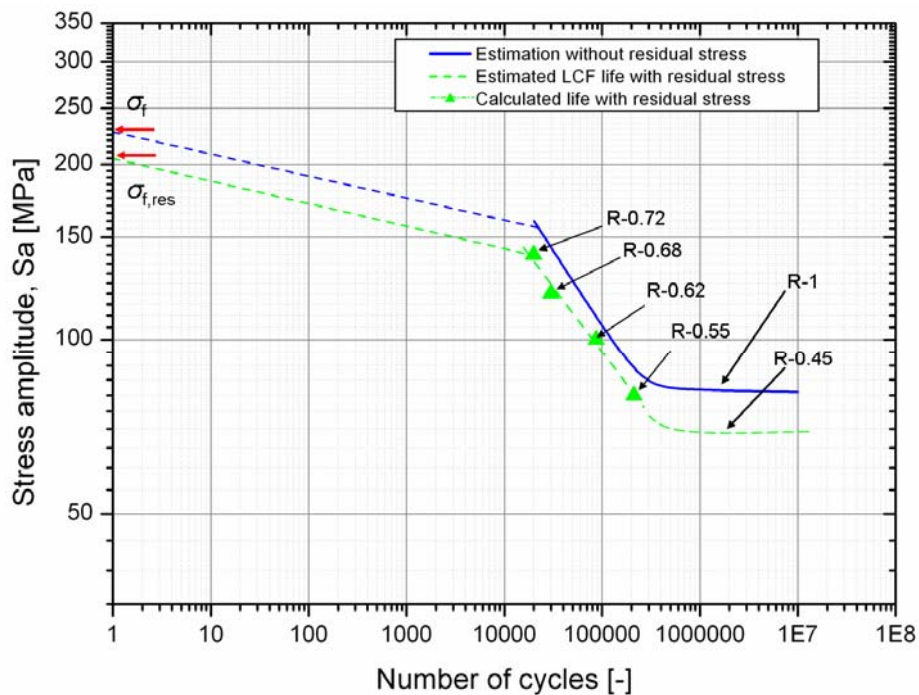


Fig. 5.21: Effect of a constant residual stress on the stress life curve (defect-free material)

For a first verification of these results in the LCF regime, results of tensile tests on specimens with weld are used. In Fig. 5.22, tensile test results for specimens with and without residual stress are compared. The welded tensile specimens are shown in Fig. 5.23. Tests were performed at a rate of 0.005 mm/sec and the strains were measured with a commercial extensometer.

It can be seen that the presence of the weld influences the stress-strain curve. The ultimate tensile strength is reduced by 16% to 250 MPa. Similarly, the 0.2% proof strength (Fig. 5.24) assumes a value of 140 MPa, also giving a 10 % reduction in yield strength.

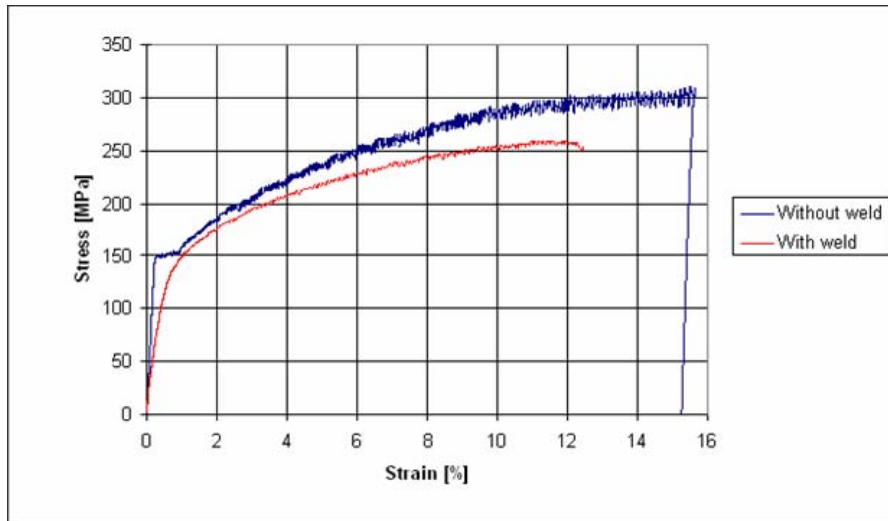


Fig. 5.22: Tensile tests for aluminium 5083 specimens with and without residual stress



Fig. 5.23: Welded tensile specimens (direction of the weld perpendicular to the specimen axis)

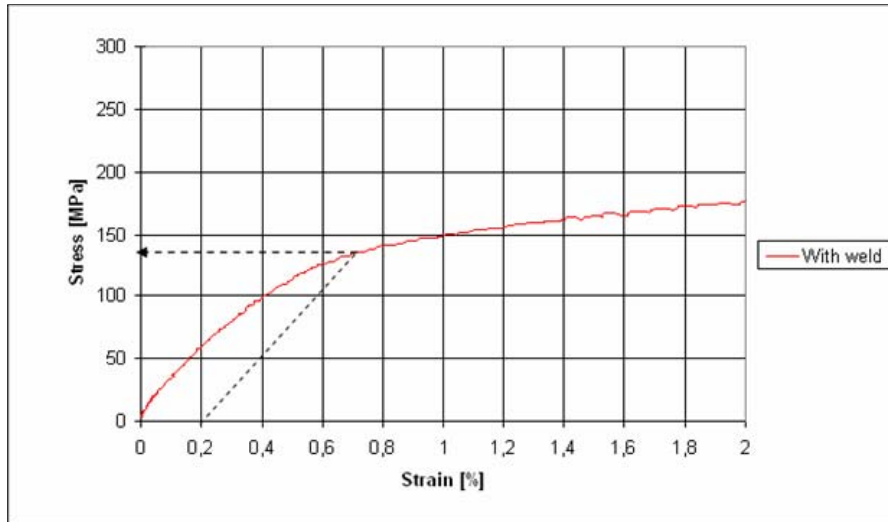


Fig. 5.24: Estimation of proof strength from tensile test of welded specimen

In Fig. 5.25, the estimated life for a constant residual stress has been obtained for an initial flaw size of 0.14 mm (filled circles). Again, different points at various load amplitudes were calculated with the corresponding stress ratios. The estimated points in the LCF regime were obtained as detailed in section 5.2.2. It can be seen that the estimated life-time for various stress levels lies in between the fatigue life curves for a defect-free material with a stress ratio $R = -1$ and for a material with a flaw size of 0.14 mm at a stress ratio $R = -0.42$ – the ratio obtained for an applied loading corresponding to the fatigue limit of a material with this particular flaw size. These points follow the line which joins the static flow stress for a material containing a defect as obtained from

$$\sigma_{fd,Res} = \sigma_{fd} - \sigma_{res} \tag{5.11}$$

where σ_{fd} is the flow stress for a material with a certain flaw given in Equ. (5.8). In this way, an estimate for the stress life curve of a material with a certain flaw size under an average residual stress can be obtained. However, this remains to be verified experimentally.

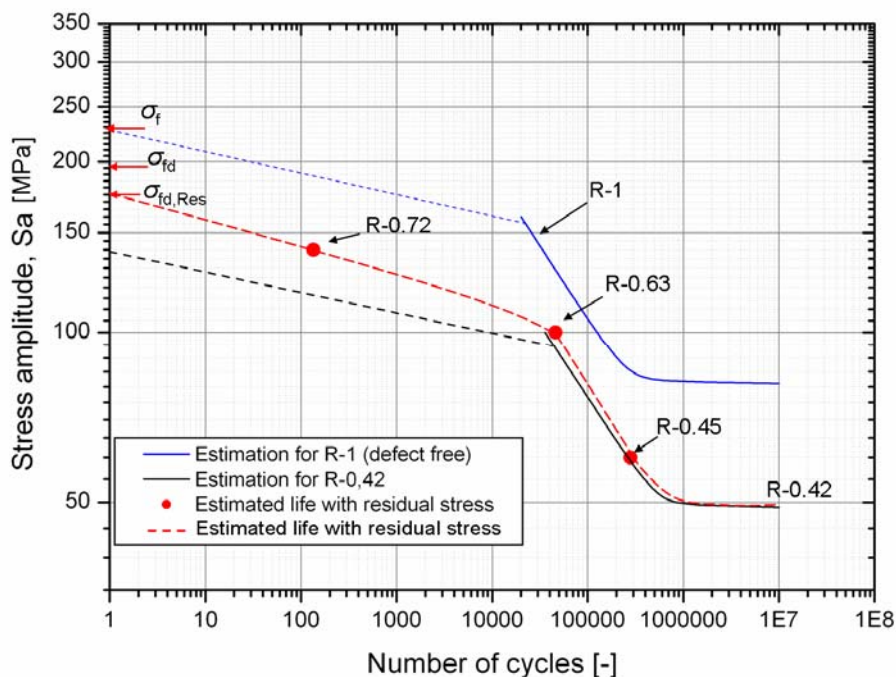


Fig. 5.25: Fatigue life estimation for material with defect under weld residual stress

6. Guidelines for Engineering Estimates

In what follows, the general method developed in Section 3 and the learnings from the model calibration in Section 5 are briefly summarized in the form of guidelines for engineering estimates. By means of an intrinsic crack length – either from El Haddad's estimate or from the NDT detection limit – a unified approach is possible by reducing a nominally defect-free case to a case with an intrinsic defect.

Flow charts representing the methodologies for both defect-free and defect-containing cases are shown in Fig. 6.1 and Fig. 6.2, respectively.

6.1. Material without defects

1. Estimate the static properties of the material – yield stress σ_y , ultimate tensile strength σ_u
2. Calculate the flow stress σ_f – Equ. (3.22)

$$\sigma_f = \frac{\sigma_y + \sigma_u}{2}$$

3. Estimate fatigue crack growth properties from available data or fatigue crack growth tests $m, C, \Delta K_{th}$,
4. Estimate the initial crack size from NDT limit. If not available, intrinsic crack size can be used with Equ. (3.7) using the endurance limit and crack growth threshold

$$l_0 = \frac{1}{\pi} \left(\frac{\Delta K_{th,lc}}{Y \Delta \sigma_{lim,0}} \right)^2$$

5. Find the fracture toughness of the material or estimate ΔK_c from fatigue crack growth data
6. Compute the final crack size using ΔK_c – Equ. (3.13)

$$a_f = \frac{1}{\pi} \left(\frac{K_{lc}}{\sigma_{max}} \right)^2$$

7. Calculate the HCF part of the S-N curve by integrating the fatigue crack growth law (Paris Equ. (1.29) or Kohout function Equ. (1.34)

$$\frac{da}{dN} = C(\Delta K)^m$$

$$\frac{da}{dN} = CK_c^n \left(\frac{\Delta K}{(1-R)^\gamma} \right)^{m-p} \left[\frac{\{(\Delta K(1-R)^{-\gamma})^p\} - \Delta K_{th0}}{\{K_c^n - (\Delta K(1-R)^{-1})^n\}} \right]$$

8. Find the number of cycles at which the HCF part of the S-N curve will cross the yield stress

9. LCF estimation: Join the number of cycles at yield stress with number of cycles at flow stress – Equ. (3.24)

$$\sigma_a = \sigma_f (N)^m$$

10. Mean stress influence for the HCF part: change the R value in the crack growth function

11. Mean stress influence for the LCF part: obtain the yield stress for a particular R ratio using Equ. (5.3); obtain stress ratio dependent $\sigma_{f,R}$ from Equ. (5.4)

$$\sigma_{y,R} < \sigma_y \frac{(1-R)}{2}$$

$$\sigma_{f,R} = \frac{\sigma_f}{\sigma_y} \cdot \sigma_{y,R}$$

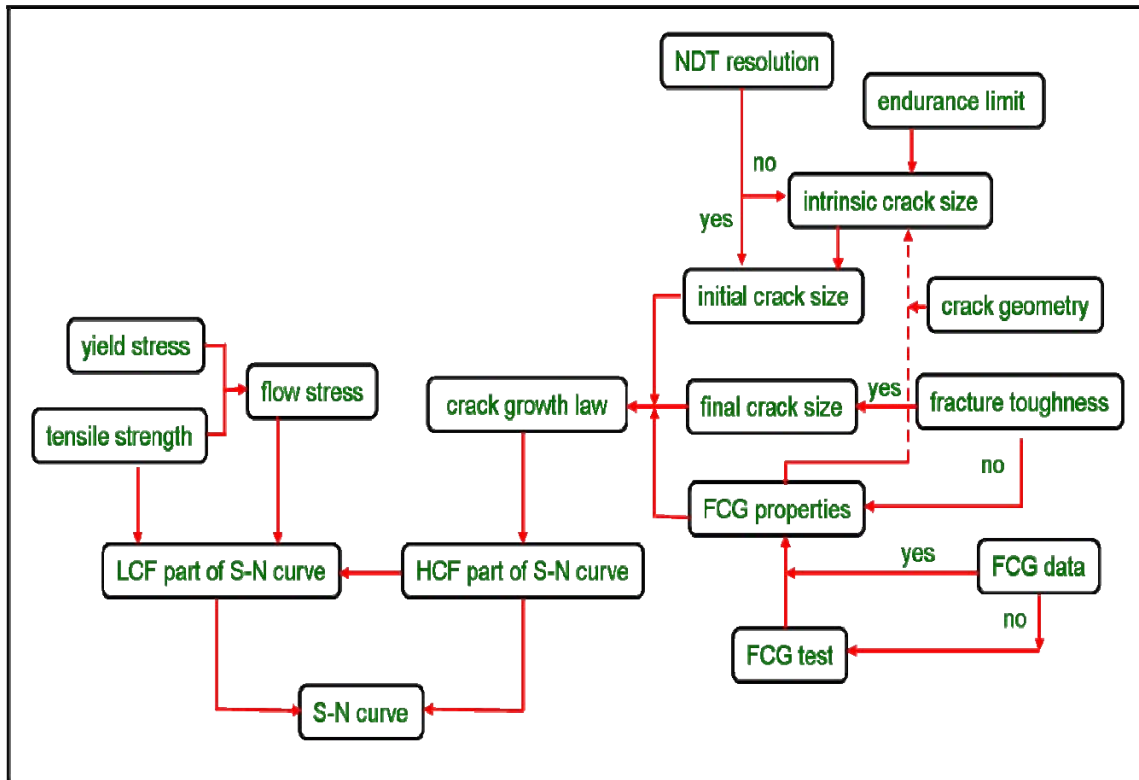


Fig. 6.1: Flowchart for obtaining the S-N curve for a defect-free material

6.2. Material with defects

1. Estimate the static properties of the material – yield stress σ_y , ultimate tensile strength σ_u
2. Calculate the flow stress σ_f – Equ. (3.22)

$$\sigma_f = \frac{\sigma_y + \sigma_u}{2}$$

3. Estimate fatigue crack growth properties from available data or fatigue crack growth tests: m , C , ΔK_{th} ,
4. Estimate the intrinsic crack size from Equ. (3.7) using the endurance limit and crack growth threshold

$$l_0 = \frac{1}{\pi} \left(\frac{\Delta K_{th,lc}}{Y \Delta \sigma_{lim,0}} \right)^2$$

5. Add the size of the defect a_0 to l_0 from step 4 above
6. Find the fracture toughness of the material or estimate ΔK_c from fatigue crack growth data
7. Compute the final crack size using ΔK_c – Equ. (3.13)

$$a_f = \frac{1}{\pi} \left(\frac{K_{Ic}}{\sigma_{max}} \right)^2$$

8. Calculate the HCF part of the S-N curve by integrating the fatigue crack growth law (Paris Equ. (1.29) or Kohout function Equ. (1.34)

$$\frac{da}{dN} = C(\Delta K)^m$$

$$\frac{da}{dN} = CK_c^n \left(\frac{\Delta K}{(1-R)^\gamma} \right)^{m-p} \left[\frac{\{(\Delta K(1-R)^{-\gamma})^p\} - \Delta K_{th0}}{\{K_c^n - (\Delta K(1-R)^{-1})^n\}} \right]$$

9. Calculate the yield strength σ_{yd} of the defect-containing material using net section yielding – for surface defect use Equ. (5.6)

$$\sigma_{yd} = \sigma_y \left(1 - \frac{a}{t} \right)$$

10. Calculate flow stress for material with defect – Equ. (5.8)

$$\sigma_{fd} = \frac{\sigma_f}{\sigma_y} \cdot \sigma_{yd}$$

7. Fatigue Testing on Thin Tubes

7.1. Introduction

Modern engineering applications such as automobile, aerospace etc. contain thin walled piping mainly under cyclic loading. In some cases these are obtained by bending and welding thin sheets.

Many pressure vessel codes such as ASME [93] are based on uni-axial fatigue testing. However; due to the fact that certain pressurized equipments such as piping experience a multi-axial fatigue loading, the study of such components under these loadings is of high value.

In what follows, the static and fatigue behaviour of thin-walled pipes with and without defects under multi-axial conditions is considered. A special-purpose test rig is developed for characterizing the response of thin-walled pipes under internal pressure and axial cyclic loading.

7.2. Background

Considering the typical case of a pressure vessel under internal pressure p and axial tension F , the stresses within the vessel are: axial stress σ_a , radial stress σ_r and tangential stress σ_t . Under static loading, the failure can be avoided if the von Mises equivalent σ_v stress is below the yield strength σ_y . Accordingly,

$$\sigma_v \leq \sigma_y \quad \text{Equ. (7.1)}$$

$$\sigma_v = \sqrt{\frac{1}{2}[(\sigma_t - \sigma_a)^2 + (\sigma_a - \sigma_r)^2 + (\sigma_r - \sigma_t)^2] + 3\tau^2} \quad \text{Equ. (7.2)}$$

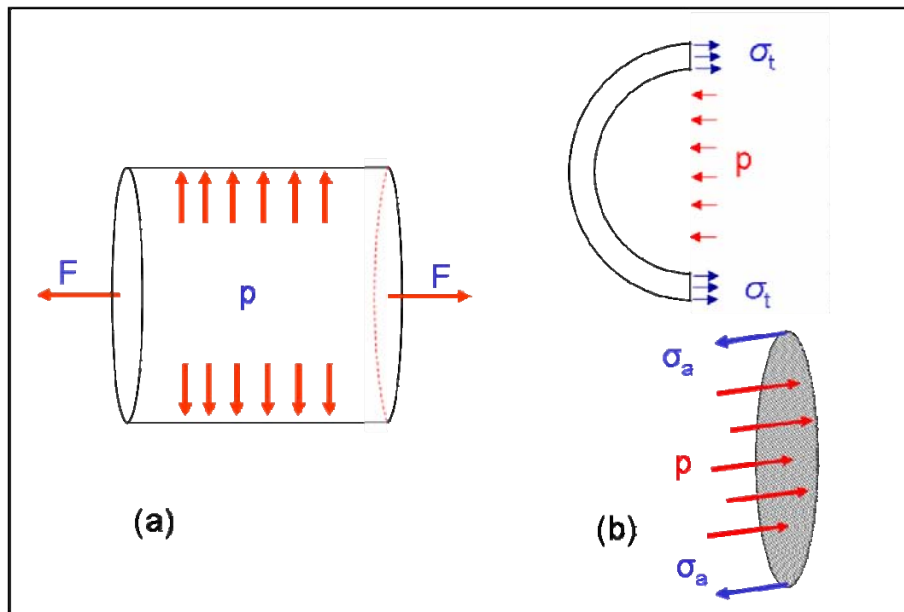


Fig. 7.1: Thin pipe under pressure and axial force (a), tangential and axial stress definition (b)

Using the equilibrium force diagram (Fig. 7.1b), the various stresses can be obtained

$$\sigma_r = -p \quad \text{Equ. (7.3)}$$

$$\sigma_t = \frac{pR}{t} \quad \text{Equ. (7.4)}$$

$$\sigma_{a,p} = \frac{pR}{2t} \quad \text{Equ. (7.5)}$$

where $\sigma_{a,p}$ is the axial stress due to the internal pressure p . The axial stress is superimposed by the stresses due to the axial tensile force F

$$\sigma_{a,F} = \frac{F}{A} \quad \text{Equ. (7.6)}$$

However for thin-walled tubes with $R/t \geq 10$ [90], the radial stress can be neglected and the stress state may be assumed to be biaxial. Consequently, in the absence of any torque, where the shear stress drops out, Equ. (7.1) becomes

$$\sigma_v = \sqrt{\sigma_t^2 - \sigma_t \sigma_a + \sigma_a^2} \quad \text{Equ. (7.7)}$$

7.3. Design approximations

The objective of the general design is to keep the stresses within the allowable limit so that the vessel does not fail within the design limits. In design codes, generally the stresses are categorized into primary, secondary and peak stresses. For pressure vessels the allowable stresses (or design stress intensity S_m) are not expressed in terms of yield or tensile stress, instead a multiple of design stress is considered, which is typically two-thirds of yield strength or one-third of ultimate tensile strength. For the general primary membrane stress intensity, P_m , the local primary membrane stress intensity, P_L and the combined membrane and bending stress intensity $P_L + P_b$, the limits for design conditions are typically expressed as [91]:

$$\begin{aligned} P_m &\leq S_m \\ P_L &\leq S_m \\ P_L + P_b &\leq 1.5S_m \end{aligned} \quad \text{Equ. (7.8)}$$

For a moderately thick shell employing thin shell theory, the design equations for computing the minimum thickness t are obtained by equating the allowable stress S_m and the hoop stress [91].

$$t = \frac{pR_i}{S_m - 0.5p} \quad \text{Equ. (7.9)}$$

$$t = \frac{pR_o}{S_m + 0.5p} \quad \text{Equ. (7.10)}$$

where R_i and R_o are the inner and outer radii of the tube. The approximate design equations in the ASME code are based on equating the maximum membrane stress to the allowable stress S corrected for joint efficiency E . Accordingly, in ASME Section VIII Div1¹² [92]

$$t = \frac{pR_i}{SE - 0.5p} \quad \text{Equ. (7.11)}$$

$$t = \frac{pR_o}{SE + 0.5p} \quad \text{Equ. (7.12)}$$

and in ASME Section III Div 1¹³ [92]

$$t = \frac{pR_i}{SE - 0.6p} \quad \text{Equ. (7.13)}$$

¹² Rules for construction of pressure vessels

¹³ Rules for construction of nuclear facility components

$$t = \frac{pR_o}{SE + 0.4p} \quad \text{Equ. (7.14)}$$

7.4. Design for cyclic loading

Although fatigue is not a common failure phenomenon in pressure vessels, some pressure vessels such as those used in aerospace applications experience fatigue loading. Various methodologies are available for pressure vessel design against fatigue, such as ASME Section VIII Div2 and BS 5500. These methodologies have mainly been developed for defect free assessment. The ASME fatigue design curves are mainly derived from uni-axial strain controlled fatigue tests on machined samples, and are used in combination with stress concentration factors in order to account for structural discontinuities.

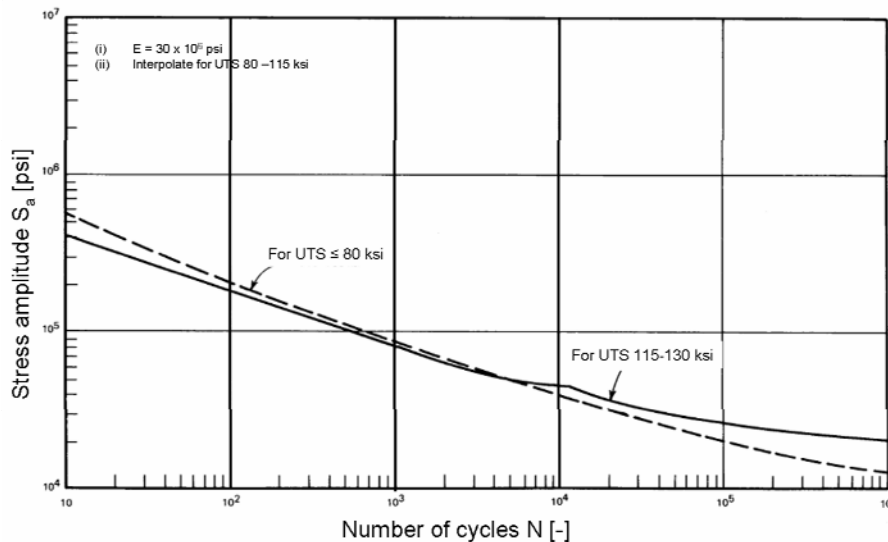


Fig. 7.2: ASME design fatigue curve for various steels [93]

For obtaining the fatigue life curves within the stress based diagram, the strains are multiplied by the elastic modulus. A design margin has been provided such as to make the calculated stress intensity and the amplitude and the allowable stress amplitude directly comparable. Fig. 7.2 shows the ASME design fatigue curves for carbon, low alloy, high alloy, high tensile steels. These curves are based on strain controlled tests and the best fit curves are downscaled by a factor of 2 on stress or a factor of 20 on number of cycles to account for environment, size and scatter of data [91].

7.5. Experimental details

7.5.1. Design of experimental rig

Multi-axial fatigue is an important consideration for the design of components under cyclic loading. For the current case the basic load parameters are

- Axial force
- Internal pressure

For thin-walled pipes a biaxial stress state is assumed incorporating the hoop and axial stresses. The principal stress ratio λ is defined as

$$\lambda = \frac{\sigma_t}{\sigma_a} \quad \text{Equ. (7.15)}$$

where σ_t and σ_a are the hoop and axial stresses. Substituting Equ. (7.15) into Equ. (7.7) gives

$$\sigma_a = \frac{\sigma_y}{\sqrt{(\lambda^2 - \lambda + 1)}} \quad \text{Equ. (7.16)}$$

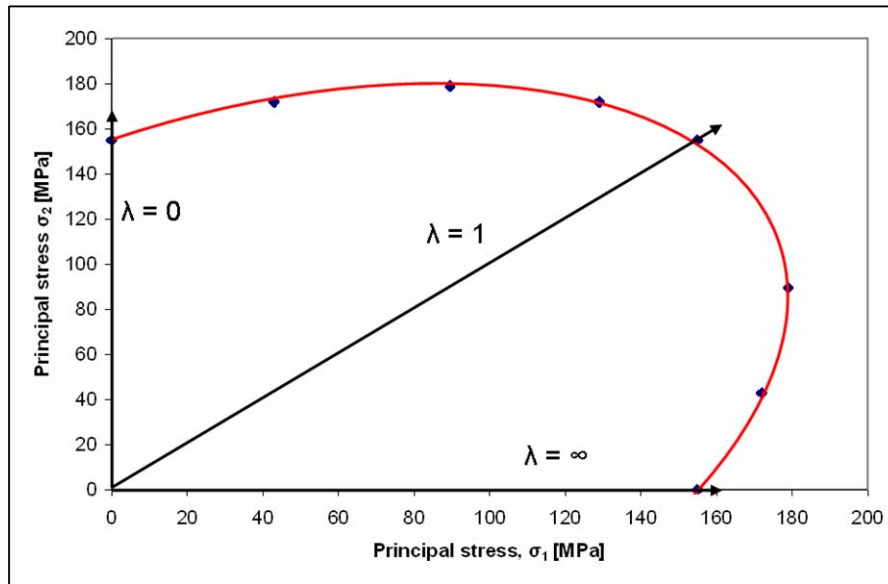


Fig. 7.3: Principal stress diagram for aluminium 5083 H111 using Mises criterion

The axial stress σ_a is a combination of the axial component due to internal pressure and the axial force itself

$$\sigma_a = \sigma_{ap} + \sigma_{aF} \quad \text{Equ. (7.17)}$$

where σ_{ap} and σ_{aF} are given in Equ. (7.5) and Equ. (7.6). Using these equations, a principal stress diagram of the yield locus can be drawn. For the current material with a yield strength of 155 MPa, such a diagram is shown in Fig. 7.3.

Based on these considerations, for a tube of diameter D and thickness t , a force versus pressure diagram can be obtained. Fig. 7.4 shows such a diagram for various principal stress ratios. It can be seen that a principal stress ratio of $\lambda = 0$ means pure axial force and no internal pressure. Similarly, a principal stress ratio of $\lambda = 2$ will mean pure internal pressure and no external axial force.

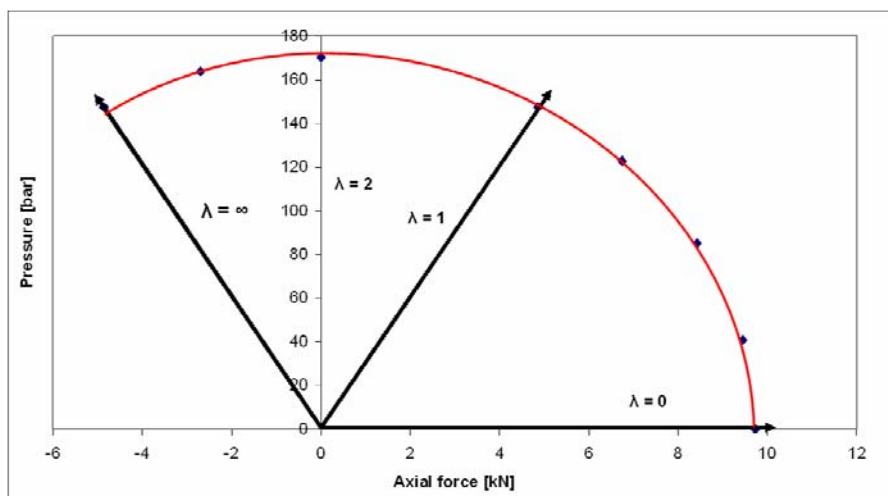


Fig. 7.4: Pressure–force diagram at different principal stress ratios for aluminium 5083 H111 using the von Mises criterion

In order to obtain the fatigue behaviour for various materials, a dedicated test setup has been designed so that arbitrary combinations of pulsating internal pressure with axial tension can be obtained. For this reason the use of two hydraulic cylinders is considered. For the internal pressure, the axial force of one of the hydraulic cylinders is used such that it generates the cyclic loading within the hollow specimen through hydraulic oil with the help of a piston. The basic working principle is highlighted in Fig. 7.6. This setup has the advantage of being applicable to a wide range of materials for fatigue loading. Further it has the capacity of loading a thin walled specimen with various principal stress ratios. The test rig is directly mounted on a hydraulic cylinder with a load cell.

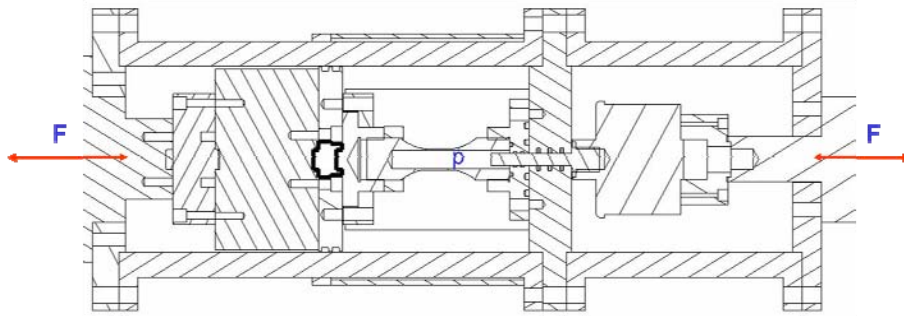


Fig. 7.5: Testing of tube specimens under cyclic internal pressure and cyclic axial tension

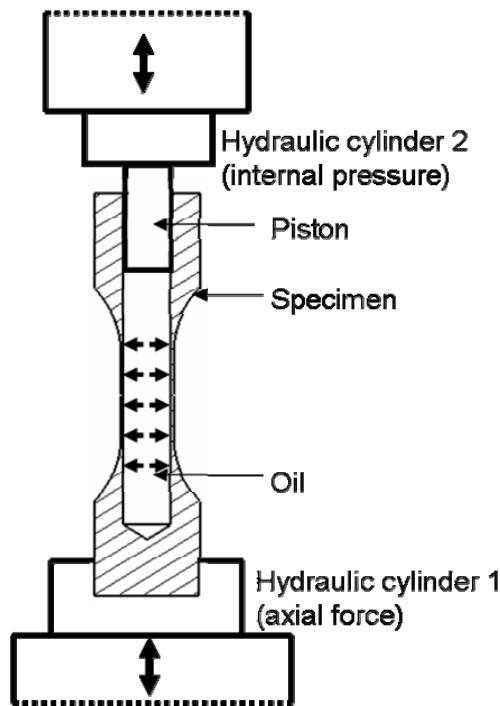


Fig. 7.6: Working principle of the test setup

7.5.2. Material and specimen

Although the test setup has been designed for obtaining the material behaviour of various materials, the current study focuses on investigating aluminium 5083 H111. The material was received in a solid rod shape and was machined in house to obtain the desired thin-walled hollow specimens.

Fig. 7.7 shows the geometry and dimensions of the test specimen. The inner diameter was kept at 19 mm, giving a wall thickness of 1 mm. The gauge length was kept sufficient for measurement of strains. The hollow section of the tube can also be seen in Fig. 7.7 where an R/t ratio of approximately

10 was maintained in order to keep the condition of thin walled cylinders. The specimen was fine threaded at both ends for mounting in the test rig.

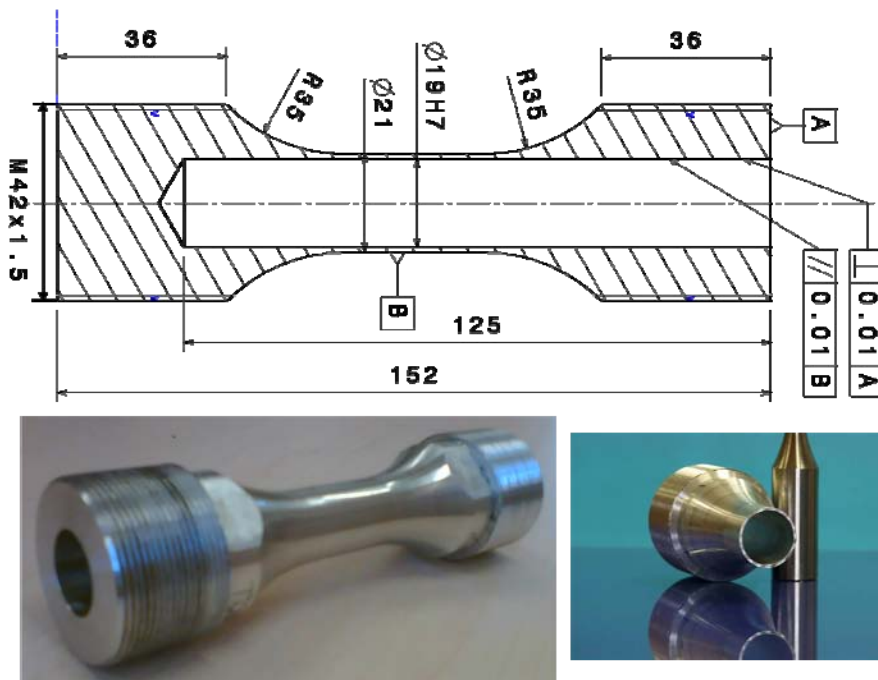


Fig. 7.7: Geometry and dimensions of the test specimen

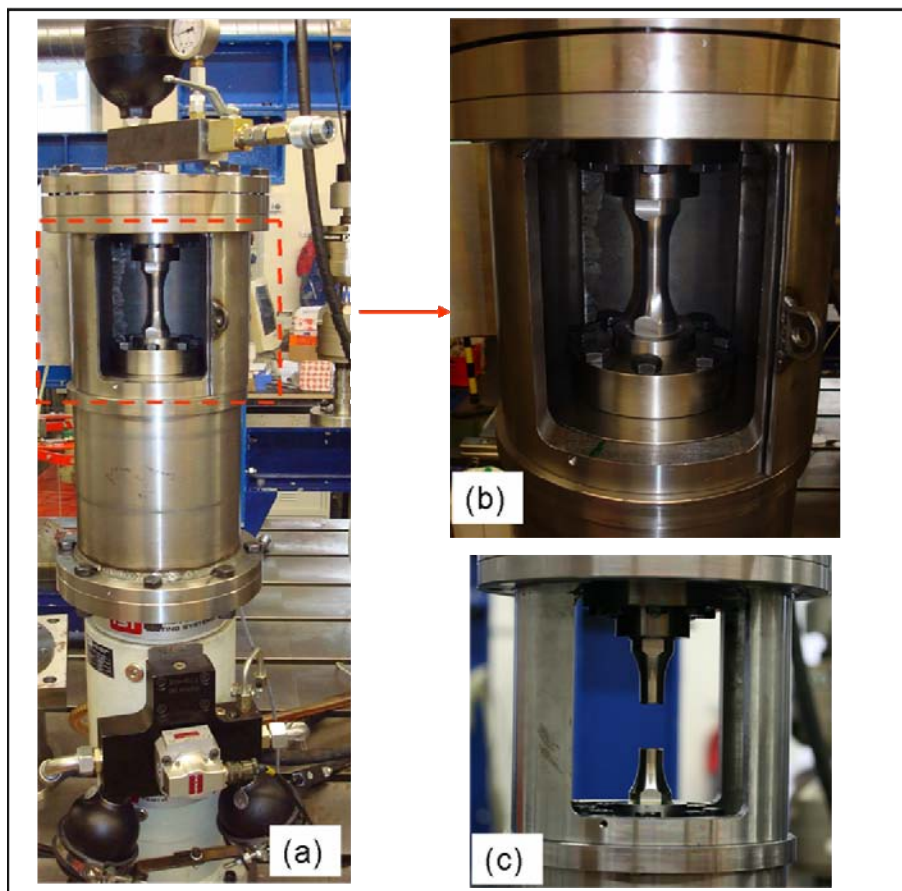


Fig. 7.8: Testing of thin walled specimens

7.5.3. Fatigue tests

For biaxial loading, fatigue tests can be performed at different frequency, phase angle and principal stress ratios. Preliminary testing was performed at a phase angle $\phi = 0$ and a frequency of 30 Hz.

The following sets of high cycle fatigue tests were performed

- HCF tests at a principal stress ratio $\lambda = 0$
- HCF tests at non-constant principal stress ratio

In the former case, the tests were performed with pure axial force, i.e. the internal pressure was kept zero, and in the latter case an internal pressure of 100 bar (10 MPa) was maintained.

For obtaining the fatigue behaviour of a specimen with defects, some specimens containing machining flaws were also tested. These tests were also performed

- with internal pressure
- without internal pressure

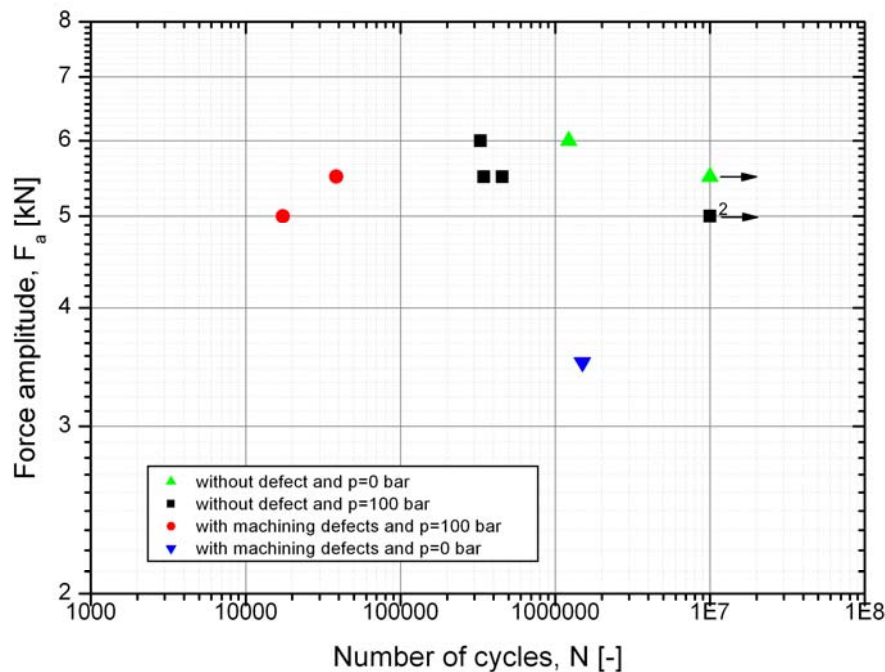


Fig. 7.9: Fatigue test results of thin walled specimens at (external axial) load amplitude ratio $R = 0$

7.6. Results and discussion

The high cycle fatigue results are shown in Fig. 7.9. The tests were conducted at a load ratio $R = 0$ under load control at room temperature. Although a precise statistical analysis could not be made due to the reason that the tests were performed on a limited number of specimens, however; a variety of parameters as mentioned in previous section were assessed.

The fatigue tests for smooth specimens without any apparent flaw and with no internal pressure show the highest lifetime. The tests were carried out until failure or 10^7 number of cycles. Apparently, in the absence of internal pressure, only the cyclic axial tension was responsible for inducing the damage.

On the other hand, the fatigue tests performed with internal pressure show a relatively lower lifetime. At the endurance limit, the stress amplitude has dropped by approximately 10%. Similarly, at same stress amplitude (of 95.5 MPa) the number of cycles to failure is decreased by more than 50%. This shows the major influence of the internal pressure.

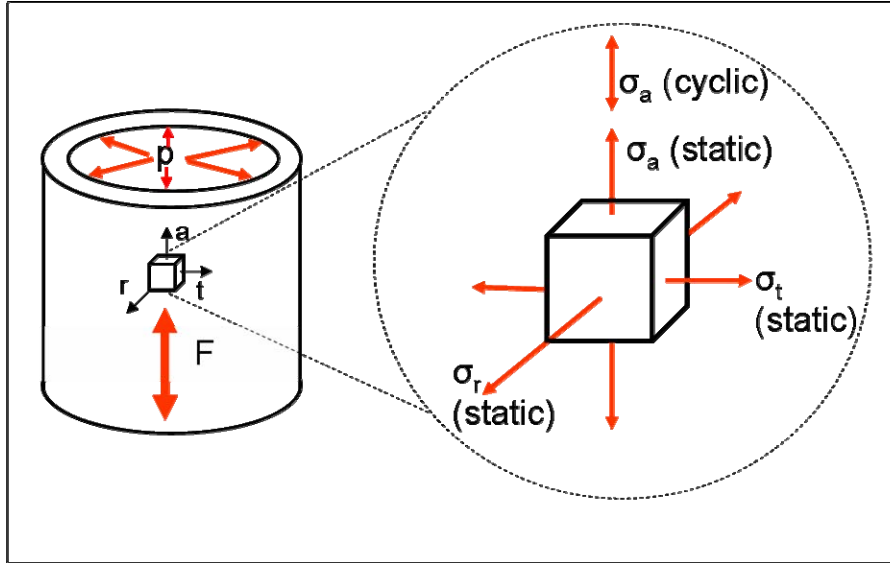


Fig. 7.10: Various stresses on the specimen

As described earlier, the internal pressure is employed as a static parameter. There are three static stress components as result of this applied pressure – axial, tangential and radial stress (cf. Fig. 7.10). Thus, the superimposition of the axial part of the stress component due to internal pressure will act as a mean stress over the applied axial cyclic tension. By this way a rise in mean stress takes place. For the current specimen geometry, an applied pressure of 100 bar will result in an axial stress of 52 MPa (cf. Equ. (7.5)), meaning that mean stress will be raised from 95 MPa to 147 MPa (a load ratio change from $R = 0$ to $R = 0.35$), thereby reducing the fatigue properties.

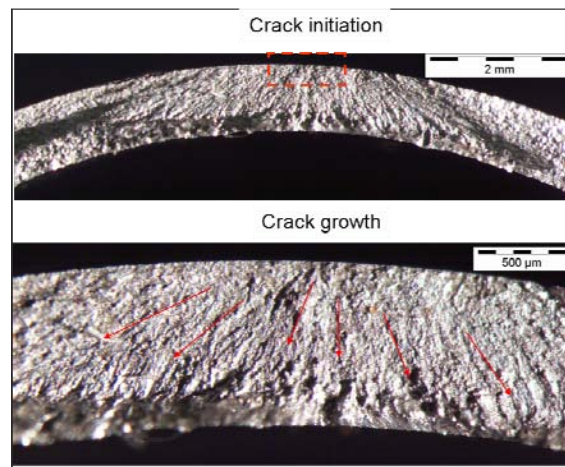


Fig. 7.11: Crack initiation and growth in a specimen tested under cyclic axial tension and static internal pressure

Fig. 7.11 shows the fractured surface of a specimen tested under both cyclic axial tension and static internal pressure. The microscopic analysis of the surface shows the initiation of the crack from the outer surface. As the radial stress is equivalent to the internal pressure (i.e., negative) at the internal surface, and zero at the outer surface, the preferred site of crack initiation is the outer surface.

The fatigue lifetime for a specimen tested with a machining defect was observed to be considerably lower. For damage tolerant design of components, the geometry and orientation of the flaws is of major importance. In the current case, the flaw considered was a real machining flaw.

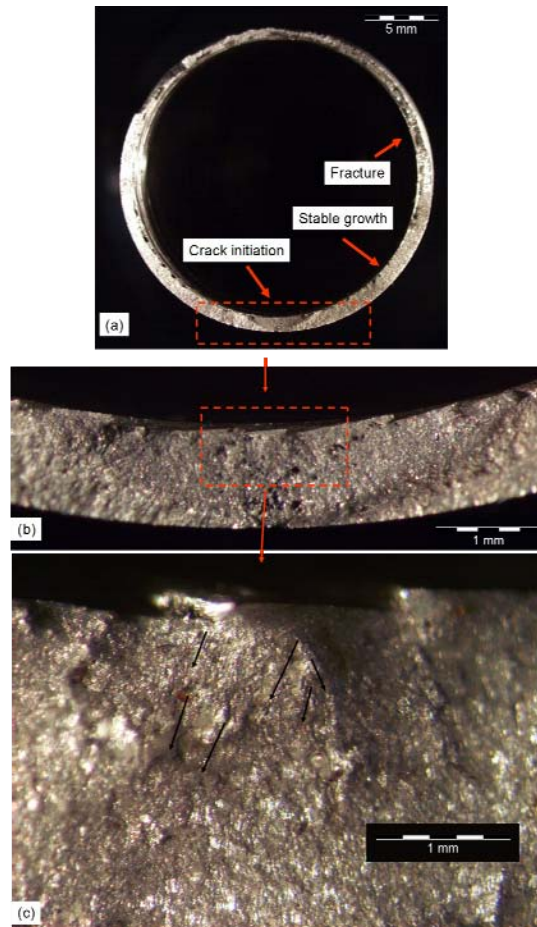


Fig. 7.12: Fractured section of thin walled specimen under axial tension with machining defect (a), crack growth from initial flaw (b) and (c) (flaw size $\sim 0.1\text{-}0.14$ mm)

Fig. 7.12 shows the fractured surface of such a specimen containing machining defects and tested under cyclic tension only. A post-mortem inspection under the light microscope shows the depth of the flaw to lie between 0.10 mm and 0.14 mm. Contrary to the previous case of a defect-free specimen, the crack initiation was facilitated from the crack-like machining flaw at the inner surface of the specimen. Typical fatigue crack striations can be seen in Fig. 7.12, where the crack is moving initially towards the outer radius followed by growth along the circumferential direction. Referring to the cross-sectional view under the microscope, Fig. 7.12 (a), a symmetrical growth of the crack can be seen prior to the final fracture. However, due to the small thickness of the specimen, plastification has started just after more than half of the area has been covered by the fatigue crack.

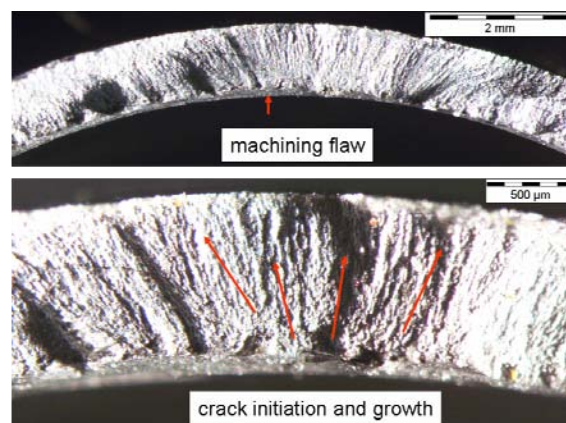


Fig. 7.13: Crack initiation and growth in a specimen with machining flaw tested under cyclic axial tension and static internal pressure (flaw size ~ 0.1 mm)

A crude comparison with the specimen tested only under axial tension can be made. The fatigue lifetime of a specimen with machining defect under such loadings tested at a 35% lower load was about 1.5 million cycles compared to 10 million cycles life without defect, which shows a considerable effect of the machining defect on the fatigue lifetime.

Results of fatigue testing of specimens with defects tested under both cyclic tension and static internal pressure are also shown in Fig. 7.9. As described earlier for the defect-free case, the mean stress effect is also influential here. The presence of a machining flaw further accelerates the damage process.

Fig. 7.13 shows the fractured surface of the specimen with a machining flaw of depth ~ 0.12 mm. As expected, the crack initiation starts from the machining flaw at the inner surface. However, it can be seen that the crack starts from more than one point.

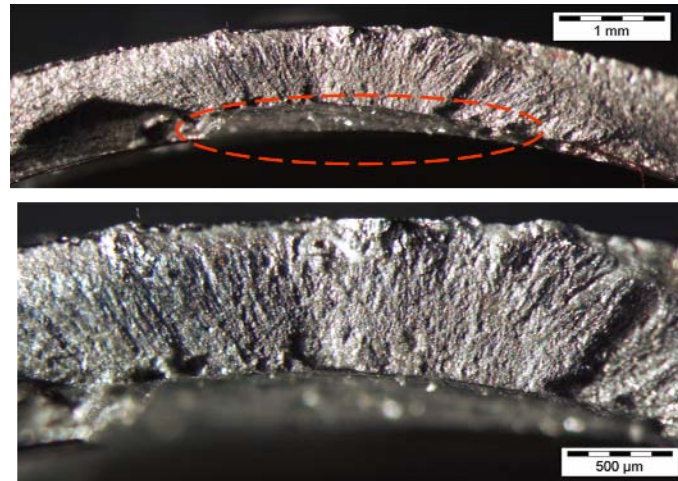


Fig. 7.14: Crack initiation and growth of specimen with machining flaw tested under cyclic axial tension and static internal pressure (flaw size ~ 0.2 mm)

Similar to the previous case, micrographs for a flaw size of ~ 0.2 mm are shown in Fig. 7.14. Again, the flaw growth occurs from the inner surface with a similar path as in the previous case. However, the lifetime is reduced by about 50%, although the load amplitude is approximately 10% lower. Clearly, an increase in the flaw depth decreases fatigue life time.

defect \ pressure	without pressure	without pressure
without defect	crack initiation from outer surface	crack initiation from outer surface
with defect	crack propagation from defect (inner surface)	crack propagation from defect (inner surface)

Tab. 7.1: Comparison of crack initiation and growth cases

7.6.1. Application of the DTD engineering estimates to thin tubes

Using the method for estimating the fatigue life curve for a material with certain defects based on the sheet specimen data, a comparison of the tube specimen data with the prediction is presented in Fig. 7.17. The predicted curves have been obtained for a stress ratio $R = 0$ for a material with and without defect. In case of internal pressure of 100 bar, this ratio becomes $R = 0.35$. The procedure discussed in chapter 5 has been followed. Accordingly, the HCF and LCF predictions were obtained¹⁴.

¹⁴ It is to be noted that due to the non-availability of FCG data for the tube material, the slope m and coefficient C of the sheet material has been used. Moreover, the intrinsic crack size has been assumed to be the same which in turns gives $\Delta K_{th} = 3.2 \text{ MPa}\sqrt{\text{m}}$ using $\sigma_{0(R=0)} = 70 \text{ MPa}$ from FKM (cf. Tab. 7.2).

Fig. 7.15 shows the comparison of the tensile curve of tube material with the sheet material. Clearly, both materials have different tensile properties. The yield stress and tensile strength of the tube material has been obtained as as 250 MPa and 360 MPa, respectively.

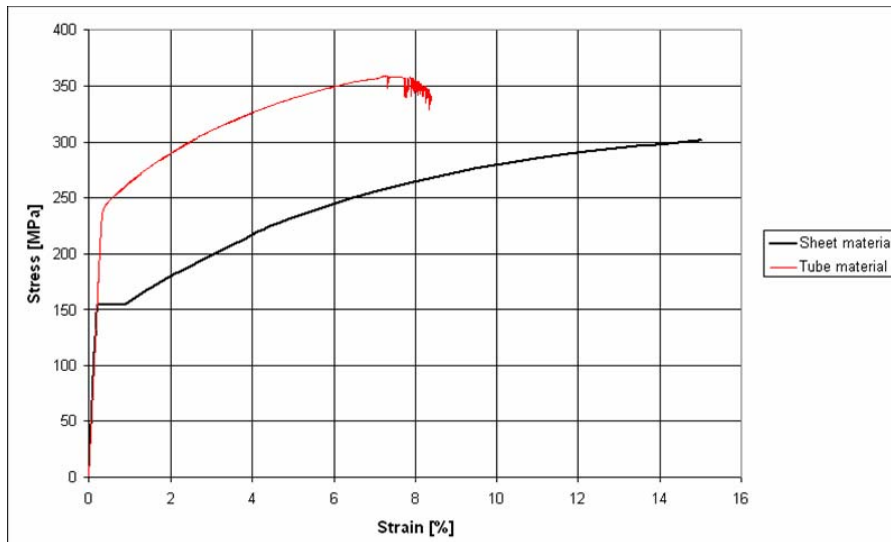


Fig. 7.15: Comparison of partly tensile curve of tube material with the tensile curve of sheet material

Material	Yield stress R_e [MPa]	Tensile strength R_m [MPa]	Endurance limit ($R = 0$) [MPa]	Source
Sheet (5083 H111)	155	300	61	test results
Tube (5083H14/H24/H34*)	250	360	70*	test results/ *FKM [107]

Tab. 7.2: Tensile data for sheet and tube material

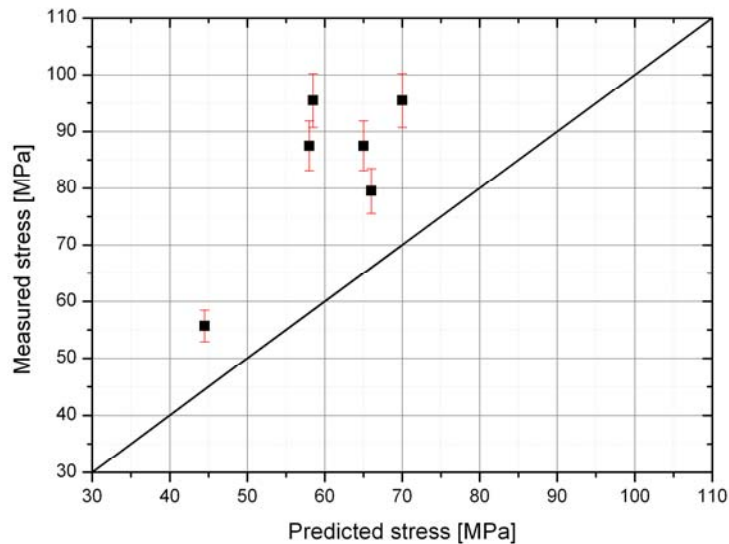


Fig. 7.16: Comparison of predicted stress values with measured data for same number of cycles to failure for tube material (see also Fig. 7.17)

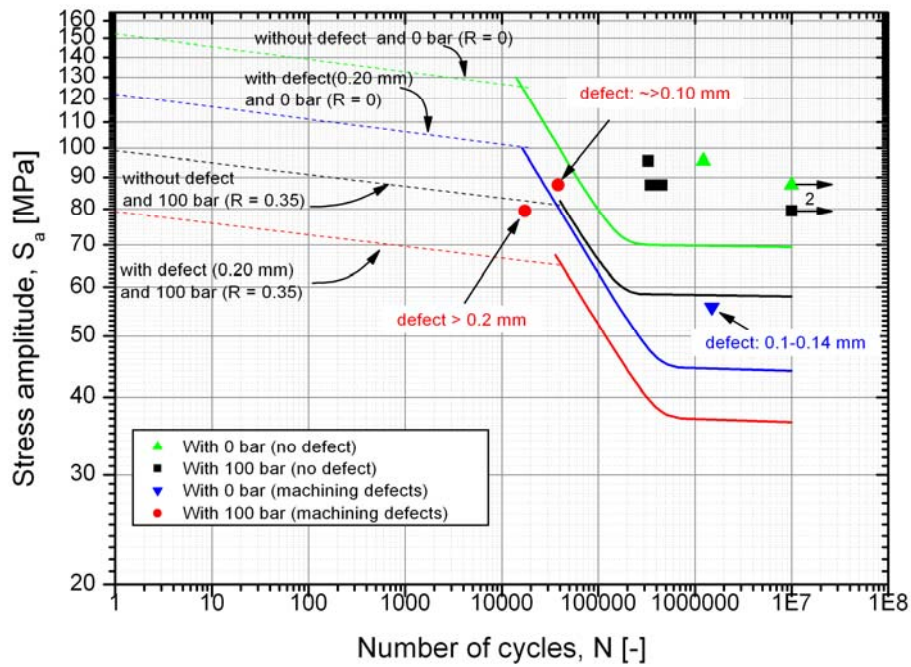


Fig. 7.17: Comparison of estimated stress life curve for tube material with and without defect with thin tube test data

For the HCF estimate, fatigue crack growth parameters C and m have been taken from the sheet material. The endurance limit at pulsating loading from the FKM guideline has been used. For the estimation of the LCF part, tensile data and HCF part of the curve have been used in a similar way as described previously.

The comparison shows that the prediction is on the conservative side in all cases (cf. also Fig. 7.16). However, it must be noted that the value of the endurance limit taken from FKM (70 MPa for $R = 0$) is rather conservative.

8. Comparison and Validation

Fatigue assessment against flaws is one of the considerations in codes like BS 7910, ASME Section XI, FKM fracture mechanics guidelines and FITNET. The latter two use the guidelines of BS 7910 for the assessment of components containing flaws. BS 7910 contains assessment procedures for both welded and un-welded parts. It uses two approaches for assessing flaws under fatigue loading:

- For planar flaws, fracture mechanics based fatigue crack growth methodologies are considered.
- Assessment of non-planar flaws is based on experimental S-N curves.

However, for planar flaws a simplified procedure related to S-N curves can also be adopted.

The general methodology for the assessment of flaws is outlined for steels. Once the crack growth law has been obtained, the assessment of a particular flaw is obtained using the following steps:

- Select the values of C , m , ΔK_{th}
- Determine ΔK for cyclic stress range and flaw height and shape
- Calculate crack growth rate until the final crack growth or specified design life. The flaw is acceptable if the limit to crack growth is not exceeded throughout design life.

8.1. Comparison with crack growth data

Recommended fatigue crack growth laws for steels are provided as mean values and mean+2SD (standard deviations) for two cases:

- (i) $R < 0.5$
- (ii) $R \geq 0.5$

For welded components with residual stresses, conservative estimates can be obtained using the mean+2SD (standard deviations) laws for $R \geq 0.5$.

However, in case of non-ferrous materials such as aluminium alloys, BS 7910 recommends to modify the crack growth constants for steels according to the ratio of Young's modulus E . Accordingly, for aluminium alloys the following value of the crack growth constant C is given:

$$C = C_{\text{steel}} \left(\frac{E_{\text{steel}}}{E} \right)^3 \quad \text{Equ. (8.1)}$$

Similarly, the threshold stress intensity factor can be obtained as follows:

$$\Delta K_{th} = \Delta K_{th, \text{steel}} \left(\frac{E}{E_{\text{steel}}} \right) \quad \text{Equ. (8.2)}$$

The recommended values for preliminary screening assessments are as follows:

$$m = 3,$$

$$C = 5.21 \times 10^{-13} \text{ and}$$

$$\Delta K_{th} = 63 \text{ MPa}\sqrt{\text{mm}} \text{ (} 2 \text{ MPa}\sqrt{\text{m}} \text{)}$$

A comparison of BS 7910 recommended crack growth law with experimental fatigue crack growth is presented in Fig. 8.1. The influence of the Paris slope m is seen clearly. Using the value for m suggested in BS 7910, the crack growth curve is on the lower side of the experimental data in region II. On the other hand, the threshold stress intensity range ΔK_{th} computed for aluminium as $0.5 \text{ MPa}\sqrt{\text{m}}$ is lower than the experimental value.

Generally, for aluminium alloys the value of the Paris slope can vary from 2.5 to 4.5 (cf. figure 17 in [11]). Thus, for the current material the prediction of the BS 7910 will not be conservative in the crack growth region; however, in the threshold regime the approximation is on the safe side.

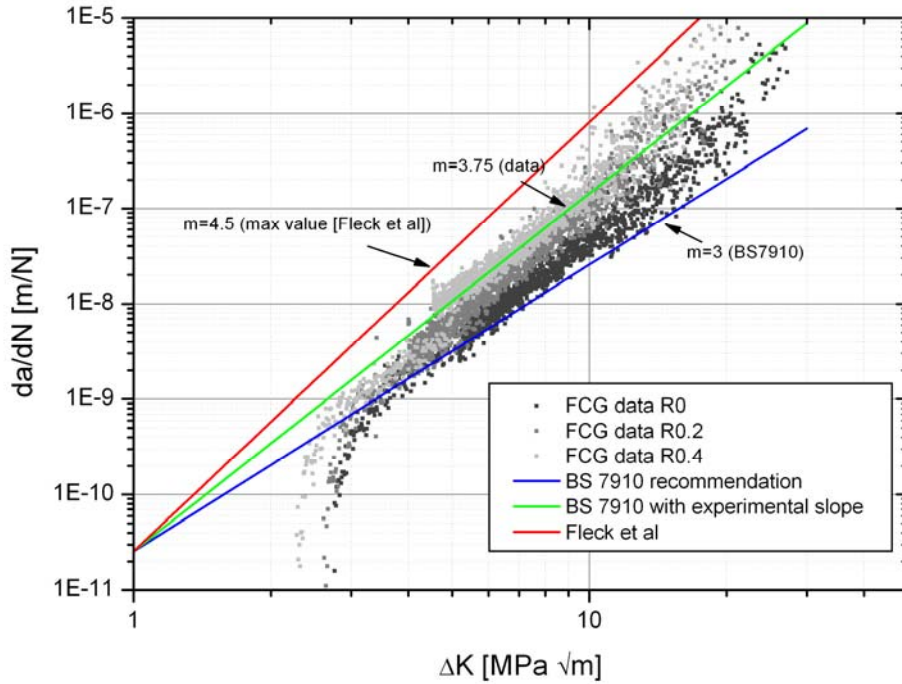


Fig. 8.1: Comparison of fatigue crack growth curves recommended in BS 7910 with experimental data

8.2. Comparison with quality S-N curves

Another method for obtaining the assessment of flaws in the BS 7910 is to use the S-N curves that represent the actual and required fatigue strengths of the flawed part. In this case; a grid of S-N curves is given in which each curve represents a particular quality category. The flaw is acceptable if its actual quality category is the same or higher than the required quality category.

The required quality category is determined for the service conditions experienced by the flawed weld. This can be fixed on the basis of the stress ranges and the total number of cycles of fatigue loading. Alternatively, the quality category can be selected by reference to adjacent design details.

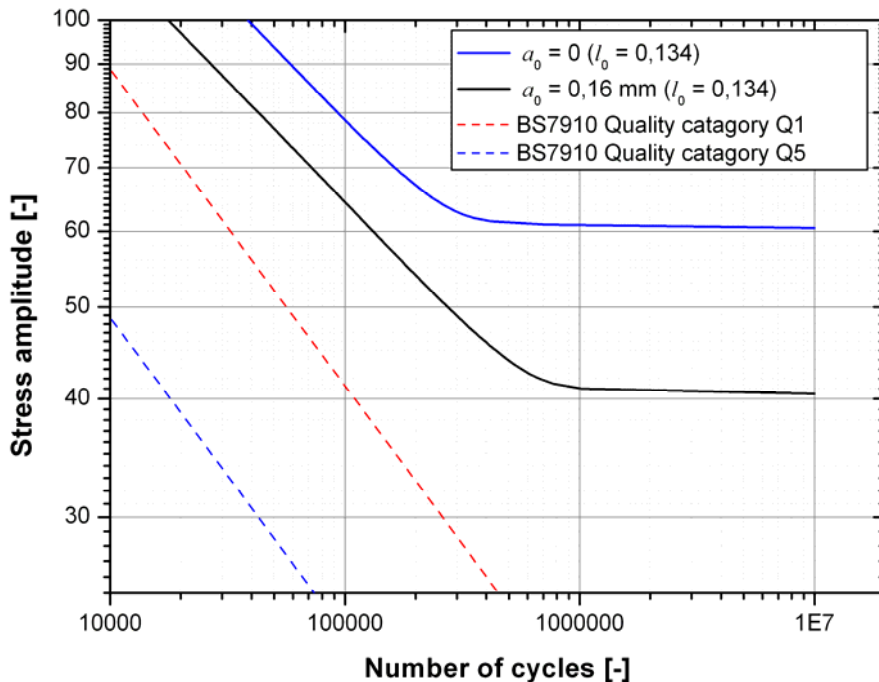


Fig. 8.2: Comparison of estimated S-N curves with BS 7910 quality S-N curves

Following the guidelines of BS 7910, the estimated S-N curves obtained by the method described in chapter 3 have been compared with the quality S-N curves from BS 7910. The following flaw geometry has been considered for both cases:

Type of flaw: surface flaw; Depth of the flaw $a = 0.14$ mm; Thickness of the specimen $t = 1$ mm

The procedure for obtaining the quality S-N curve is as follows:

- using a/t and $a/2c$ ($a = 0.14$ mm, $2c \approx 3-4$ mm, $t = 1$ mm), find the effective flaw parameter a'_i/t and hence $a'_i/t = 0.10$ (Fig. 17a in BS 7910)
- effective flaw $a'_i = 0.1$ mm
- similarly: obtain a'_{max} (taking 90% of the thickness)
- using Fig. 17b in BS 7910, obtain S_i and S_{max}
- calculate S using $S = (S_i^3 - S_{max}^3)^{1/3}$
- the actual quality category for the flaw in question is the next below S in Table 7 of BS 7910. If this is the same as or higher than the required quality category, the flaw is acceptable.

The quality category S-N curves are described by the following equation:

$$\Delta\sigma^3 N = Const \quad \text{Equ. (8.3)}$$

where the values of the constant are provided in Table 7 of BS 7910. Accordingly, a quality category Q2 was obtained for the flaw size above at an applied stress $S = 30$ MPa at $1 \cdot 10^6$ cycles.

The various values for the flaw geometry above were obtained using an extrapolation of Fig. 17a,b in BS 7910, as the figures do not provide values below 5 mm thickness.

Fig. 8.2 compares the quality S-N curves of BS 7910 with the estimated S-N curves according to the method described in chapter 3. The estimated S-N curves are shown for material with and without flaw. Q1 and Q5 of the quality S-N curves have been obtained for aluminium alloys. The comparison shows that the BS 7910 quality S-N curves are very much on the conservative side of the estimated S-N curves for both flawed and unflawed material.

8.3. Application to cryogenic conditions

Environmental effects greatly influence the fatigue life of a material. Aluminium alloys such as 5083 H111 are being used increasingly for cryogenic systems such as liquid hydrogen vessels or space applications due to their good resistance in such environments. Under these circumstances, the material experiences extremely low temperatures and the material properties may change. In literature many investigations under cryogenic temperature for different materials can be found.

A recent research about the fatigue behaviour of aluminium 5083 under cryogenic temperatures has been reported by Yuri et al [106]. In this study, specimens were obtained from aluminium plates.

Temperature (K)	Yield strength (MPa)	UTS (MPa)	Elongation at fracture, ϵ (%)	Reduction in area (%)	Young's modulus, E (MPa)
293	153	310	18.1	30.7	72000
77	168	433	36.3	32.5	74000
4	192	577	30.3	35.4	83000

Tab. 8.1: Tensile properties of A5083 at 293, 77, and 4 K [106]

Tab. 8.1 presents the tensile properties of the material at different temperatures. Comparing the tensile data with Al 5083 H111 thin sheet material (Tab. 4.2) at room temperature, it can be seen that in both cases the yield stress and ultimate tensile strength have nearly identical values. Thus from Tab. 8.1, it can be seen that the tensile values increase with decreasing temperatures. The fracture strain at 4 K seems to be remarkably high.

For HCF, cylindrical (dia. 6 mm) hourglass-type specimens and for LCF cylindrical (dia. 6 mm) specimens with gauge length of 12 mm were used. Tests were performed at 4 Hz in the range of 10^6 cycles and at 10 Hz above that. Moreover, the frequency at 77K and 4K was also kept at 10 Hz in order to avoid heating of the samples as a result of cyclic loading. HCF tests were performed at a load ratio $R = 0.01$. The comparison in Fig. 8.3 indicates an increase in the endurance limit with decreasing temperature. The endurance limit at 77 K is raised by 70 %. However, it must be noted that the endurance limit for aluminium 5083 plate at room temperature in [106] is 20 % higher than for the sheet material in the current study. Moreover, with respect to the yield strength at 4 K, two of the four data points shown in Fig. 8.3 for HCF seem to belong already to the LCF regime.

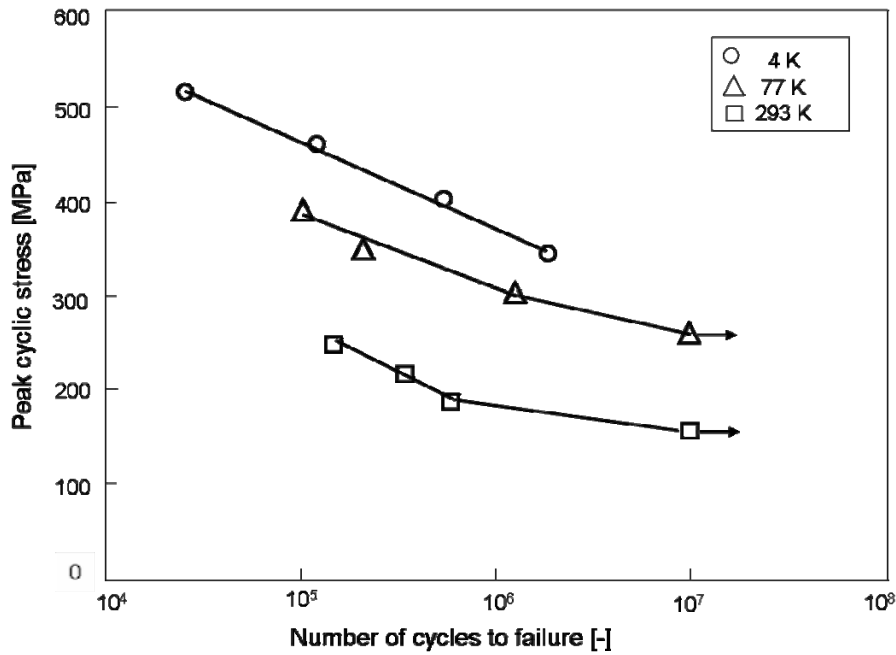


Fig. 8.3: High cycle fatigue data for aluminium 5083 at 293, 77, and 4 K (retrieved from [106])

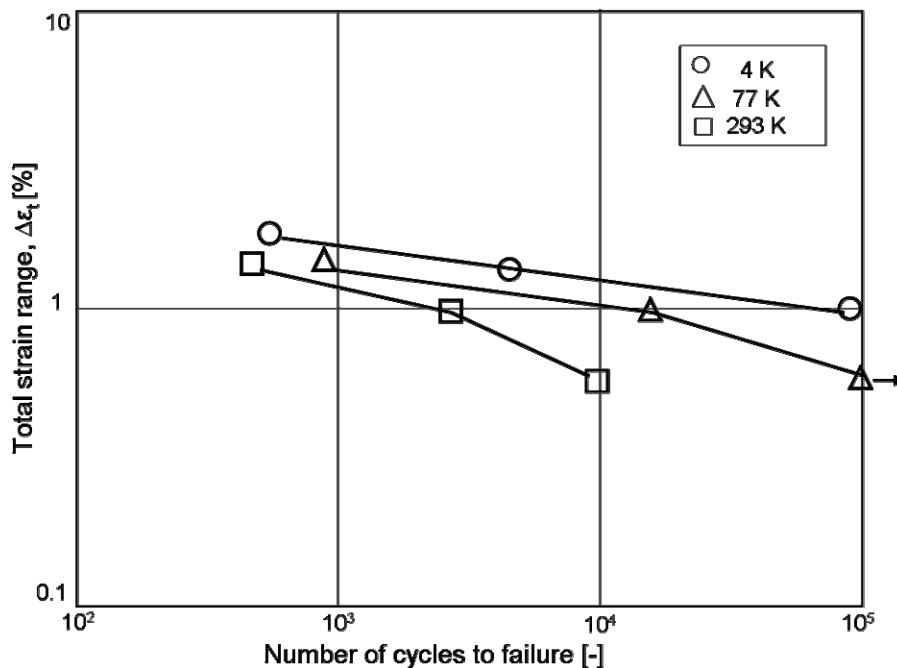


Fig. 8.4: Low cycle fatigue data for aluminium 5083 at 293, 77, and 4 K (retrieved from [106])

The low cycle fatigue data for various temperatures are plotted in Fig. 8.4. Clearly, the fatigue lives also increase with decreasing temperatures in the LCF regime, similarly to the HCF case.

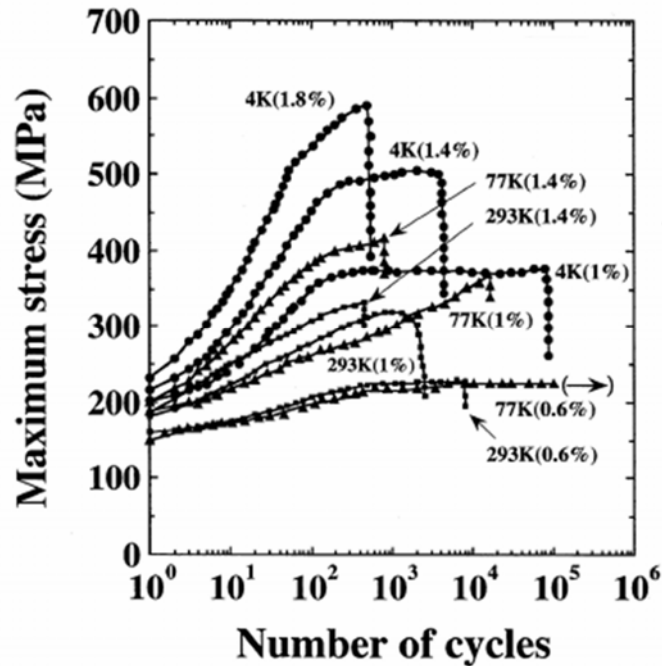


Fig. 8.5: Change of maximum stress values at different temperatures [106]

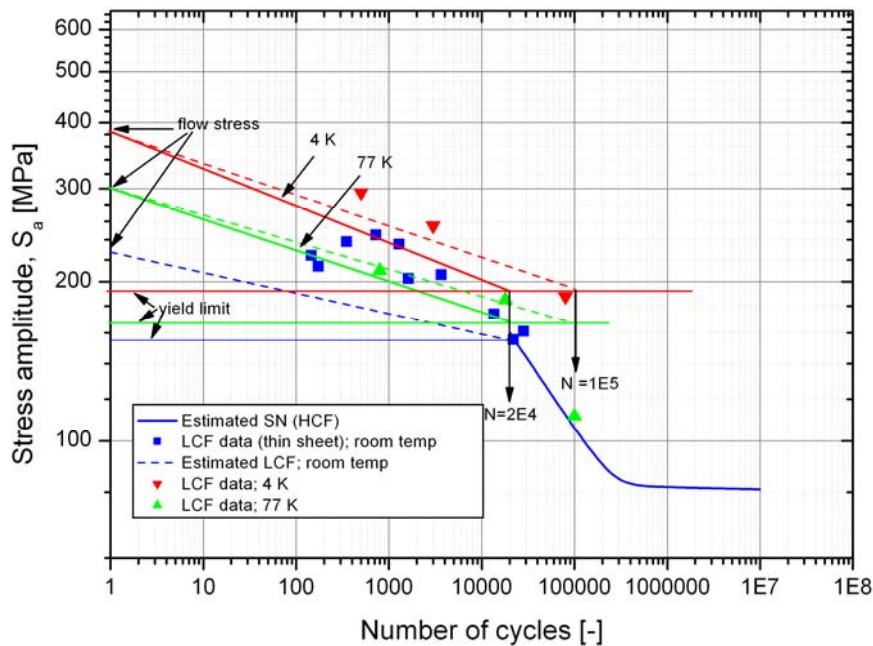


Fig. 8.6: Comparison of approximated LCF curves for thin sheet at room temperature with LCF curves at cryogenic temperatures obtained from data in [106]

Fig. 8.6 compares the LCF approximation for aluminium 5083 thin sheet with the approximated curves obtained from data in [106]. The maximum stress values at cryogenic temperatures were obtained using Fig. 8.5. For the prediction of LCF regime, the log-linear method with flow stress has been used. Due to the unavailability of data for estimating HCF curve at alternating load ratio, the start of the LCF curve (i.e., the intersection between LCF and HCF) has been assumed at $N = 2 \cdot 10^4$. Alternatively, a line to $N = 1 \cdot 10^5$ has also been shown. Clearly, the LCF predictions for both cryogenic temperatures (77 K and 4 K) give conservative results with the exception of one data point for 77 K which lies in the LCF-HCF transition regime.



8.4. Comparison with FKM Guideline

The FKM Guideline ‘Analytical Strength Assessment’ [107] provides static and fatigue data of various materials. In Tab. 8.2, the experimental results of the thin aluminium sheet (5083 H111) are compared with the FKM data. It shows that for this particular material the tensile value given by the FKM is smaller compared to the experimentally obtained value for a thin sheet material. However, for the fatigue properties the results are nearly identical.

	Yield stress, R_e [MPa]	Tensile strength, R_m [MPa]	Endurance limit at $R = 0$, [MPa]	Endurance limit at $R = -1$ [MPa]
Test results	155	300	61	81
FKM [107]	110	270	65	80

Tab. 8.2: Comparison of experimental results for sheet material with data from FKM guideline

9. Summary and Conclusion

9.1. Summary

The objective of the present work was to establish a design methodology for estimating the fatigue life of a material considering defects. Special focus was laid on providing a method for design engineers to obtain an easy estimate. Detailed experimental investigations have been performed on a thin sheet of Al5083 H111 of 1 mm thickness. The possibility of combining various design approaches, namely fatigue crack growth, high cycle fatigue (HCF) and low cycle fatigue (LCF), has been shown (see Fig. 9.1).

The results may be summarised as follows:

- The Kitagawa-Takahashi diagram serves as a tool for linking the stress-based and the fracture mechanics approaches. Using its approximation by means of the El Haddad equation, an intrinsic crack size can be determined even for a defect-free material.
- For the HCF part of the S/N curve, the relation of crack growth vs. applied stress intensity factor is integrated to obtain the crack growth lifetime. A complete estimation for this region has been obtained using Kohout's proposal for a crack growth function incorporating all the regions of the crack growth behaviour and including the effect of the stress ratio. For a defect-free material, the integration starts at the intrinsic crack size as defined by the El Haddad equation; for a material with initial defects the size of the biggest pre-existing flaw is taken as a starting value.
- For the LCF region, experimental data of strain controlled low cycle fatigue tests have been mapped to the stress-life diagram. A method has been proposed for obtaining a lifetime estimate in this region using the ultimate tensile stress, yield stress and the number of cycles at the transition between LCF and HCF regimes. – For a material with initial defects, the net section yielding concept based on the flow stress (average of yield and ultimate tensile stress) is a viable approach in the LCF region.
- Residual stresses for welded specimens are accounted for within the stress based fatigue life prediction in the form of mean stress.
- A comparison of the method proposed with the existing standard BS 7910 is favourable in that
 - the new method offers a straightforward link between the fatigue crack growth properties and the HCF part of the S-N curve
 - as well as a simple and reliable approximation of the LCF behaviour in the S-N curve
 - in a unified framework applicable to components with and without defects (the latter via the intrinsic crack length determined via the Kitagawa-Takahashi diagram or El Haddad's equation, respectively),
 - whereas the crack growth curves and the quality S-N curves from BS 7910 show some lack of consistency (cf. chpt. 8.1 and 8.2).
- The final part of the thesis has been devoted to the fatigue behaviour of thin-walled tubular specimens. A special-purpose test rig has been developed for conducting uni-axial and biaxial tests on tubular specimens. The main observations after preliminary testing are as follows:
 - For specimens with machining defects, the crack propagation occurs from the inner surface where the defects are present. For defect-free specimens, the crack initiation occurs from the outer surface.
 - Fatigue life for specimens containing defects is lower than those without defect in both load cases. For the tube specimens tested under both cyclic axial tension and static internal pressure, the fatigue life is lower than for the tube specimens tested under cyclic axial tension only.

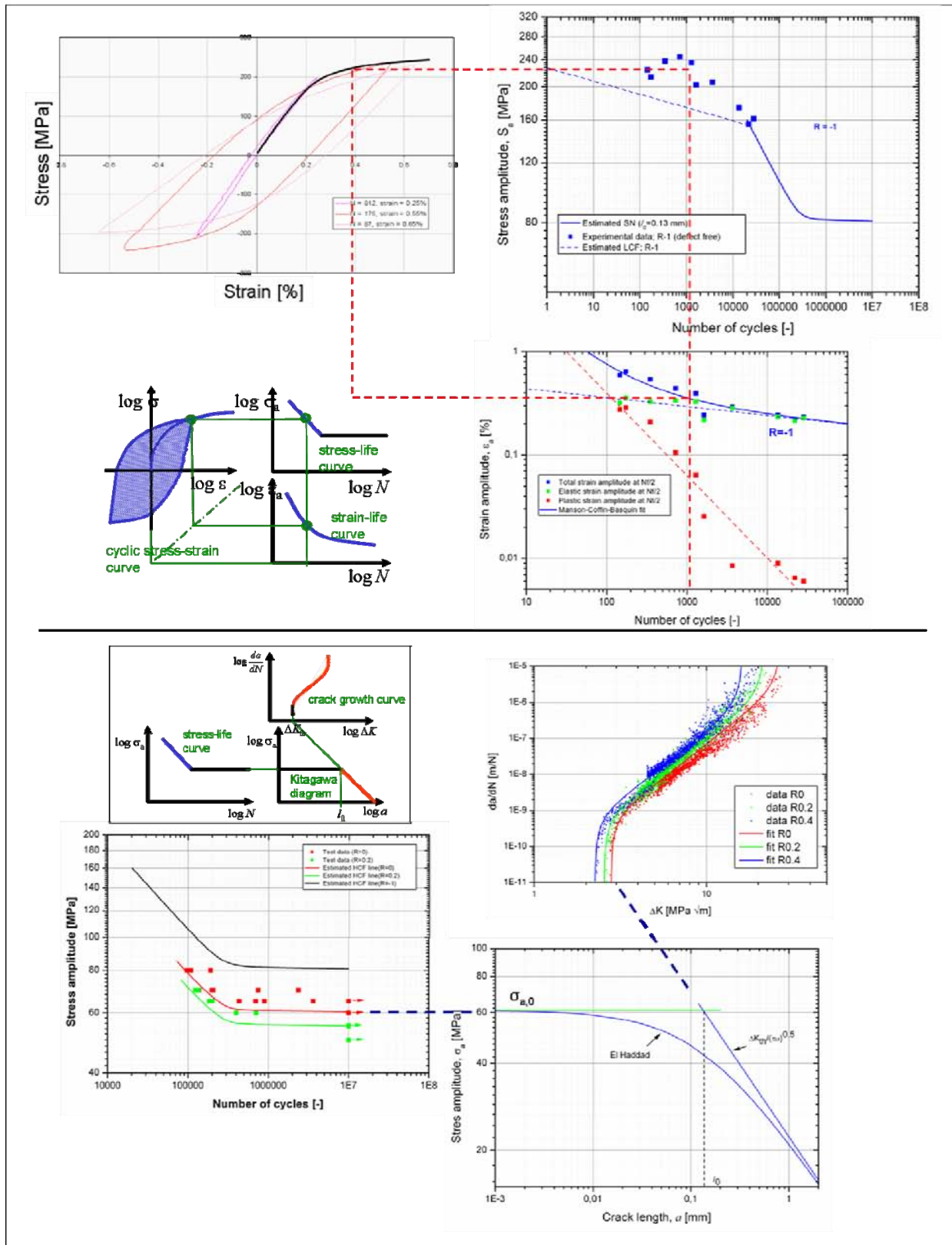


Fig. 9.1: Estimation of stress life curves for material without and with defects



9.2. Conclusion and outlook

The method developed in this thesis offers a unified framework for fatigue life assessment in the LCF, HCF and infinite lifetime domains applicable to components with and without defects, including the effects of mean stress and residual stresses.

The only basic data needed are static tensile and fatigue crack growth (FCG) properties. These data are comparatively easily determined, which makes the method suitable for application even in the early stages of design.

The method offers a balanced tradeoff between rapid applicability (due to the limited amount of test data necessary), easy use (as its final form is based on the classical concept of S-N curves), and satisfactory detailedness (accounting specifically for the mean stress influence).

Moreover, the method offers the design engineer a simple possibility for damage tolerant design by means of S-N curves for cracked components. Such S-N curves are easily generated automatically from FCG data without any need of expert knowledge from the part of the design engineer. It is hoped that, in this way, the gap between the classical methods of mechanical engineering and expert methods from fracture mechanics (including damage tolerant design considerations) may be closed.

An extension of the concept to thin-walled tubular specimens was implemented by designing a test rig offering the possibility to test specimens under arbitrary combinations of cyclic internal pressure and cyclic axial force. The first results obtained are promising; further investigations into flaws of various shapes and orientations and into multiaxial fatigue damage are underway.

10. References

- [1] Stephens, R.I., Fatemi, A., Fuchs, H. Stephens, R.R.: Metal fatigue in engineering, New York: Wiley, 2001.
- [2] Bishop, N.W.M. and Sherratt, F.: Finite element based fatigue calculations, UK, July 2000
- [3] Zerbst, U., Mädler, K., Hintze, H.: Fracture mechanics in railway applications - an overview, Engineering Fracture Mechanics 72 (2005) 163–194
- [4] Xiaoping, H., Moan, T., Weicheng, C.: An engineering model of fatigue crack growth under variable amplitude loading; International Journal of Fatigue 30 (2008) 2–10
- [5] Schijve, J.: Fatigue of Structures and Materials, ISBN 0-7923-7013-9, Kluwer Academic Publishers 2001.
- [6] Radaj, D., Vormwald, M.: Ermüdungsfestigkeit, Springer-Verlag, Berlin Heidelberg, 1995
- [7] Schijve, J.: Four lectures on fatigue crack growth. Engng Fract Mech 1979; 11:167-221.
- [8] Murakami, Y.: Metal Fatigue: Effects of small defects and non metallic inclusions, ELSEVIER, 2002.
- [9] Pippan, R.: Ausgewählte Kapitel der Festkörpermechanik (Bruchmechanik), Skriptum 2007; Montanuniversität Leoben
- [10] Anderson, T. L.: Fracture mechanics – Fundamentals and applications; CRC press London
- [11] Fleck, N. A., Kang, K. J., Ashby, M. F.: The cyclic properties of engineering materials. Acta metall. Mater 42 (1994) 365-381
- [12] Basquin, O.H.: The exponential law of endurance tests. Proc. ASTM 10, 625–630.
- [13] Leitner, H.: Simulation des Ermüdungsverhaltens von Aluminiumgusslegierungen, University of Leoben, Nov. 2001.
- [14] Bannantine, J.A.: Fundamentals of metal fatigue analysis. Prentice Hall Englewood Cliffs, New Jersey 07632; 1989
- [15] Haibach, H.: Modifizierte lineare Schadeakkumulations-Hypothese, (technical document), Technische Mitteilung des LBF, No TM 50/79, 1970
- [16] Coffin, L. F.: Transactions of American Society of Mechanical Engineering 76 (1954) 931.
- [17] Manson, S. S.: Experimental Mechanics, 5 (7) (1965) 193.
- [18] Morrow, J. D.: ASTM STP, vol. 378, American Society for Testing and Materials, Philadelphia, PA, 1964, p. 45.
- [19] Golos, K., Ellyin, F.: A total strain-energy density theory for cumulative fatigue damage. Trans ASME J Press Vess Tech 1988; 110(1):36–41.
- [20] Morrow, J., Fatigue Design Handbook, Advances in Engineering, Vol. 4, Society of Automotive Engineers, Warrendale, Pa., 1968, Sec. 3.2, pp. 21-29.
- [21] Smith, K. N., Watson, P. and Topper, T. H.: A Stress-Strain Function for the Fatigue of Metals, J. Mater., Vol. 5, No.4, 1970, pp. 767-778.
- [22] Hurley, P.J., Whittaker, M.T., Williams, S.J., Evans, W.J.: Prediction of fatigue initiation lives in notched Ti 6246 specimens
- [23] Manson, S. S. and Halford, G. R.: "Practical Implementation of the Double Linear Damage Rule and Damage Curve Approach for Treating Cumulative Fatigue Damage," Int. J. Fract., Vol. 17, No.2, 1981, pp. 169-172, R35-R42.
- [24] Griffith, A. A.: The phenomenon of rupture and flow in solids, Philos. Trans. R. Soc. London, vol. A221, 1920, p. 163.
- [25] Irwin, G. R.: Fracturing of Metals, American Society for Metals, Cleveland, Ohio, 1949, p. 147.
- [26] Irwin, G. R.: Analysis of Stresses and Strains near the End of a Crack Traversing a Plate, Trans. ASME, J. Appl. Mech., Vol. E24, 1957, p. 361.

- [27] Tada, H., Paris, P. C. and Irwin, G. R.: The Stress Analysis of Cracks Handbook, Del Research Corporation, Hellertown, Pa., 2000.
- [28] Dugdale, D. S.: Yielding of Steel Containing Slits, Journal of Mechanics and Physics of Solids Wiley Interscience, New York, 1963, p. 103.
- [29] Wells, A. A.: Unstable Crack Propagation in Metals--Cleavage and Fast Fracture: Cranfield Crack Propagation Symposium, Vol. 1, September 1961, p. 210.
- [30] Rice, J. R.: A Path Independent Integral and the Approximate Analysis of Strain Concentration by Notches and Cracks, Journal of Applied Mechanics, Transactions ASME, Vol. 35, June 1968.
- [31] Döker, H.: Fatigue crack growth threshold: implications, determination and data evaluation, Int. J. Fatigue Vol. 19, Supp. No. 1, pp. S145–S149, 1997
- [32] Barsom, J. M. and Rolfe, S. T.: Fracture and fatigue control in structures: Application of fracture mechanics ASTM *MNL41*; page 194.
- [33] Standard Test Method for Measurement of Fatigue Crack Growth Rates, ASTM E647, Vol. 03.01, ASTM, West Conshohocken, PA, 2000, p. 591.
- [34] Paris, P., Erdogan, F.: A critical analysis of crack propagation laws, J. Basic Eng. Trans. ASME, 528–534.
- [35] Wei, R. P.: Fracture Mechanics Approach to Fatigue Analysis in Design, ASME Paper No. 73-DE-22, New York, April 1973
- [36] Barsom, J. M.: Fatigue-Crack Growth Under Variable-Amplitude Loading in ASTM A514 Grade B Steel, ASTM STP 536, American Society for Testing and Materials, Philadelphia, 1973.
- [37] Crooker, T. W.: Effect of Tension-Compression Cycling on Fatigue Crack Growth in High Strength Alloys, Naval Research Laboratory Report 7220, Naval Research Laboratory, Washington, DC, January 1971.
- [38] Crooker, T. W.: Factors Determining the Performances of High Strength Structural Metals (Slope Transition Behaviour of Fatigue Crack Growth Rate Curves), NRL Report o/Progress Naval Research Laboratory, Washington, DC, December 1970.
- [39] Forman, R. G., Kearney, V. E., and Engle, R. M.: "Numerical Analysis of Crack Propagation in Cyclic-Loaded Structures," Trans. ASME, J. Basic Eng., Vol. 89, No.3, 1967, p. 459.
- [40] Priddle, E.K.: High cycle fatigue crack propagation under random and constant amplitude loadings. Int. J. Pressure Vessels & Piping, Vol.4 (1976) p.89.
- [41] Klesnil, M. and Lukáš, P.: The influence of strength and stress history on growth and stabilization of fatigue cracks. Eng. Fracture Mechanics, Vol.4 (1972) pp.77-92.
- [42] Elber, W.: Fatigue crack closure under cyclic tension. Eng Fract Mech 1970;2: 37–44.
- [43] Walker, K.: The effect of stress ratio during crack propagation and fatigue for 2024-T3 and 7075-T6 aluminum, ASTM STP 1970; 462:1–14.
- [44] Kujawski, D.: A new $(\Delta K^+ K_{max})^{0.5}$ driving force parameter for crack growth in aluminium alloys. Int J Fatigue 2001; 23:733–40.
- [45] Xiaoping, H., Moan, T.: Improved modeling of the effect of R-ratio on crack growth rate. International Journal of Fatigue 29 (2007) 591–602
- [46] Kohout, J.: A new function describing fatigue crack growth curves, Int. J Fatigue, pp.813-821
- [47] Zerbst, U., Ainsworth, R.A., Schwalbe, K.-H.: Basic principles of analytical flaw assessment methods. International Journal of Pressure Vessels and Piping 77 (2000) 855-867
- [48] Zahoor A. Ductile fracture handbook. Novotech Cop and EPRI, Res Proj 1757-69, vol. 1: 1989; vol. 2: 1990; vol. 3: 1991.
- [49] Gorrochategui, I., Gonzalez-Posada, M.A., Gutierrez-Solana, F.: On the structural integrity assessment of elastic-plastic redundant cracked structures. Engineering Fracture Mechanics 73 (2006) 2710–2722
- [50] British Standard BS7910 "Guide on Methods for Assessing the Acceptability of flaws in Fusion Welded Structures", 1999.



- [51] Webster, S., Tkach, Y.: The fracture module of the FITNET FFS procedure. Proceedings of FITNET 2006, Amsterdam, The Netherlands.
- [52] The fatigue module of the FITNET FFS procedure. Proc of FITNET 2006, Amsterdam, The Netherlands.
- [53] ASME Boiler and Pressure Vessel Code, Section XI, Rules for In service Inspection of Nuclear Power Plant Components, The American Society of Mechanical Engineers, New York, USA, 2000
- [54] ASME BPV Code Section XI Appendix A, The American Society of Mechanical Engineers, New York, USA, 2000
- [55] Singh, P.K, Vaze, K.K.: Crack initiation and growth behaviour of circumferentially cracked pipes. International Journal of Pressure Vessels and Piping 80 (2003) 629–640
- [56] Seifert, H.P., Ritter, S.: Corrosion fatigue crack growth behaviour of low-alloy reactor pressure vessel. Corros. Sci. (2008), doi:10.1016/j.corsci.2008.03.010
- [57] Pippin. R.: Fatigue threshold for engineering applications. Encyclopaedia of Materials: Science and Technology ISBN: 0-08-0431526
- [58] Ritchie, R. O., and Peters, J. O.: Small fatigue cracks: Mechanics, mechanisms and engineering applications. Materials Transactions, JIM
- [59] Venkateswaran, P., Raman S.G.S., Pathak S.D.: Generation of stress vs. crack length plots for a ferritic steel weld metal based on Kitagawa-Takahashi approach. Mat Lett 2005;59(4):495-8
- [60] Chapetti, M. D.: Application of a threshold curve model to high-cycle fatigue behaviour of small cracks induced by foreign-object damage in Ti–6Al–4V
- [61] Miller, K. J.: The two thresholds of fatigue behaviour, Fatigue Fract Eng Mater Struct 1993;16(9):931–939.
- [62] Murakami, Y. and Endo, M.: Effects of defects, inclusions and inhomogeneities on fatigue strength, Fatigue, 1994, Vol 16, April.
- [63] Pearson, S.: Initiation of fatigue cracks in commercial aluminium alloys and the subsequent propagation of very short cracks. Engng Fract Mech 1975; 7(2):235-47.
- [64] Kitagawa, H., Takahashi, S.: Applicability of fracture mechanics to very small cracks or the cracks in the early stage, Proceedings of 2nd International Conference on Mechanical Behaviour of Materials. Boston, MA, 1976:627-31.
- [65] El Haddad, M.H., Topper, T.H., Smith, K. N.: Prediction of non propagating cracks. Eng. Fract. Mech. 11 (1979) 573-584
- [66] Newman Jr., J.C.: The merging of fatigue and fracture mechanics concepts: a historical perspective. Progress in Aerospace Sciences 34 (1998) 347-390
- [67] Spagnoli, A.: Fractality in the threshold condition of fatigue crack growth: an interpretation of the Kitagawa diagram. Chaos, Solitons and Fractals 22 (2004) 589-598
- [68] Gaenser, H-P., Leitgeb, A., Glinsner, K., and Eichlseder, W.: Computation of a modified Haigh-Goodman diagram for damage tolerant design for infinite fatigue life. Proceedings of the Institution of Mechanical Engineers Part C: Journal of Mechanical Engineering Science, in press
- [69] Gänser, H-P., Glinsner, K., Eichlseder, W.: Dimensioning against fatigue - stress-based approach or fracture mechanics? Proceedings of the Institution of Mechanical Engineers, Part C: Journal of Mechanical Engineering Science, Volume 220, Number 8 / 2006
- [70] Ciavarella, M., Monno, F.: On the possible generalizations of the Kitagawa–Takahashi diagram and of the El Haddad equation to finite life. International Journal of Fatigue 28 (2006) 1826–1837
- [71] Ellyin, F.: Cyclic strain energy density as a criterion for multiaxial fatigue failure, in biaxial and multiaxial fatigue, EGF 3, Mech Eng Publ; London, 1989. p. 571–83.
- [72] Donahue RJ, Clark HM, Atanmo P, et al. Crack opening displacement and the rate of fatigue crack growth. Int J Fract Mech 1972;8: 209–19
- [73] Leitgeb, A., Jan, M.M., Gänser, H.-P., Eichlseder, W.: Engineering estimates for the fatigue and crack growth behaviour of aluminium alloys. Proc. International Conference of Fatigue 2007 (ICF-2007), July 2007, Moscow



- [74] Lemaitre, J., Desmorat, R.: Engineering damage mechanics. ISBN 3-540-21503-4 Springer, 2005
- [75] Eichlseder, W.: Betriebsfestigkeit I Skriptum, Montanuniversität Leoben
- [76] Supplier's inspection certificate, M/S Hydro Aluminium Deutschland GmbH.
- [77] Jan, M. M., Leitgeb, A., Gaenser, H-P, Eichlseder, W.: A comparative study of classical and damage tolerant design concepts, Proc. ISAM 2007, Islamabad.
- [78] Bork, C.-P., et. al.: Standardization of low cycle fatigue tests on thin sheet, LCF 6, Berlin 2008
- [79] MIL-HDBK-5J. Metallic materials and elements for aerospace vehicle structures.
- [80] <http://www.aluland.com> (Dutch aluminium sheet manufacturer)
- [81] Meggiolaro, M.A., Castro, J.T.P.: Statistical evaluation of strain-life fatigue crack initiation predictions, International Journal of Fatigue 26 (2004) 463–476
- [82] Muralidharan, U., and Manson, S. S.: Modified universal slopes equation for estimation of fatigue characteristics, Trans. ASME, J. Eng. Mater., Tech., Vol. 110, 1988, p55.
- [83] Stacey, A., Barthelemy, J.-Y, Leggatt, R.H., Ainsworth, R.A.: Incorporation of residual stresses into the SINTAP defect assessment procedure. Engineering Fracture Mechanics 67 (2000) 573-611
- [84] Jan M. M., Gaenser, H-P., Leitgeb, A., Eichlseder, W.: Synthesis of conventional and damage tolerant design concepts, 2nd Fatigue Symposium Leoben, April 2008
- [85] Tabemig, B., Powell, P. and Pippin, R.: Resistance curves for the threshold of fatigue crack propagation in particle reinforced aluminium alloys. Fatigue crack growth thresholds, endurance limits, and design, ASTM STP 1372, J. C. Newman, Jr. and R. S. Piascik, Eds., American Society for Testing and Materials, West Conshohocken, PA, 2000.
- [86] Chapetti, M.D.: Fatigue propagation threshold of short cracks under constant amplitude loading. International Journal of Fatigue 25 (2003) 1319–1326
- [87] Lassen, T.: Fatigue life analyses of welded structures. ISTE Ltd. 2006
- [88] Haibach, E.: Betriebsfestigkeit : Verfahren und Daten zur Bauteilberechnung. 2. Aufl. – Berlin, Springer, 2002
- [89] EPERC Bulletin 6: Current practices for design against fatigue in pressure equipment, June 2002
- [90] Moss, D. R.: Pressure vessel design manual. ISBN: 0-7506-7740-6, Elsevier 2004.
- [91] Chattopadhyay, S.: Pressure Vessels; design and practice, CRC press 2005
- [92] ASME boiler and pressure vessel code, The American society of mechanical engineers, New York, July 1998.
- [93] ASME Section VIII Div2 appendix 5, The American society of mechanical engineers, New York, July 1998.
- [94] SINTAP, Structural integrity assessment procedures for European industry, final procedure, British Steel Report, Sheffield. 1999.
- [95] R/ H/ R6, “Assessment of the Integrity of Structures Containing Defects”, British Energy Generation Ltd, 1999.
- [96] R5 - Issue 2, “An Assessment Procedure for the High Temperature Response of Structures”, British Energy Generation Ltd, 1998.
- [97] www.r-desk.co.uk
- [98] American Petroleum Institute, API579, “Recommended Practice for Fitness for Service”.
- [99] Kocak, M.: FITNET fitness for service procedure: an overview. Proc. of FITNET 2006, Amsterdam, The Netherlands.
- [100] <http://www.eurofitnet.org/FITNETFinalTechnRepwithProjManagement30Jan07.pdf>
- [101] AECMA Standard (prEN 3988:1998): Constant amplitude strain controlled LCF testing, published by the European association of aerospace industries.



- [102] Jan, M. M., Gaenser, H-P., Eichlseder, W.: Fatigue and fracture behaviour of a thin aluminium alloy sheet, Proc. ECF 17 Brno, September 2008.
- [103] Schwalbe, K-H., Zerbst, U., Kim, Y-J., Brocks, W., Cornec, A., Heerens, J., Amstutz, H.: EFAM ETM 97: The ETM method for assessing crack-like defects in engineering structures, GKSS Report GKSS 98/E/6, 1998
- [104] FKM Guidelines: Bruchmechanischer Festigkeitsnachweis für Maschinenbauteile, Vorhaben Nr. 229
- [105] Maddox, S. J.: Review of fatigue assessment procedures for welded aluminium structures. International Journal of Fatigue 25 (2003) 1359–1378.
- [106] Yuri, T. et al: Effect of welding structure on high-cycle and low-cycle fatigue properties for MIG welded A5083 aluminium alloys at cryogenic temperatures. Cryogenics 41 (2001) 475-483
- [107] FKM Guideline, Analytical strength assessment, 2003 VDMA Frankfurt
- [108] Paris, P.C.: Fracture mechanics in the elastic-plastic regime, ASTM STP 631, pp. 3-327, (1977)
- [109] Ruiz Ocejo, J., González-Posada, M.A., Gutiérrez-Solana, F., y Gorrochategui, I., “Development and Validation of Procedures: Review of Existing Procedures”, SINTAP Task 5, Report SINTAP/UC/04 (1997).
- [110] Kumar, V., German, M.D., Shih, C.F.: An engineering approach for elastic–plastic fracture analysis, General Electric Company, NP-1931, Research Project 1237-1 Topical Report, 1981.
- [111] Staat, M.: Local and global collapse pressure of longitudinally flawed pipes and cylindrical vessel, International Journal of Pressure Vessels and Piping 82 (2005), 217–225
- [112] Kim, Y-J., Shim, D-J., Huh, N-S., Kim, Y-J.: Plastic limit pressures for cracked pipes using finite element analyses, International Journal of Pressure Vessels and Piping 79 (2002), 321–330